Diese Dissertation haben begutachtet:

…………………. ………………….

DISSERTATION

Lorentz Force Actuated Resonant MEMS Magnetometer with Capacitive Read-out

ausgeführt zum Zwecke der Erlangung des akademischen Grades eines
Doktors der technischen Wissenschaften unter der Leitung von

Ao.Univ.Prof. Dipl.-Ing. Dr.techn. Roland Grössinger

E138
Institut für Festkörperphysik

eingereicht an der Technischen Universität Wien
Fakultät für Physik

von

MMag. Michael Stifter

Matrikelnummer: 9425863
Hammerbachgasse 16, 2620 Neunkirchen

Wien, am 25. Oktober 2012

Kurzfassung

In der vorliegenden Arbeit wird ein Lorentzkraft erregter Kragbalken beschrieben. Dieser wird als Magnetometer zur Detektion sowohl von statischen Magnetfeldern als auch magnetischer Wechselfelder verwendet. Das Bauelement ist in SOI-Technologie gefertigt, wobei die Form des Kragbalkens einem U entspricht. Der einkristalline Signalwandler befindet sich in einer Vakuumkammer, das durch ein Spulenpaar, welches als Helmholtz-Spule das Magnetfeld erzeugt, umgeben ist. Auf den Teststrukturen befindet sich eine Goldleiterbahn, welche durch einen sinusförmigen Wechselstrom durchflossen ist. Der Kragbalken wird durch die Lorentz-Kraft erregt, wobei die Auslenkung des Balkens ein Maß für die magnetische Flussdichte darstellt. Im Falle eines sinusförmigen magnetischen Flussdichte, enthält die daraus resultierende Lorentzkraft zwei alternierende Terme, welche sowohl Summen- als auch Differenzfrequenzen des Wechselstrom und des magnetischen Wechselfeldes enthalten. Der in Resonanz betriebene Kragbalken wird dabei als Mischer in einer Heterodynen-Konfiguration zur Detektion für magnetische Wechselfelder mit variabler Frequenz verwendet. Dabei tritt Resonanz nur auf, wenn eine dieser Mischfrequenzen in der Nähe der mechanischen Resonanzfrequenz liegt, welche auch die Auswahlregel der Feldkonfiguration erfüllt. Der Schwerpunkt wird im resonanten Betrieb auf der Untersuchung der ersten symmetrischen, der ersten antisymmetrischen und der zweiten symmetrischen Schwingungsmode gelegt. Hierbei ist die Schwingungsamplitude proportional der zur messenden Vektorkomponente des Magnetfeldes. Die Empfindlichkeit eines Resonators wird dabei sehr stark vom Gütefaktor Q bestimmt. Die Ursachen des Gütefaktor Q sind jedoch derart vielseitig, daß der mechanischen Gütefaktor Q bei kontrolliertem Umgebungsdruck im Bereich von 0,01 Pa bis 100 Pa analysiert wurde. Die experimentellen Ergebnisse wurden mit bestehenden Theorien verglichen, wobei der Vergleich eine Unterbewertung der Dämpfungsparameter für den Knudsen-Bereich von $Kn = 0,1$ bis 10 zur Folge hatte. Das hier präsentierte Dämpfungsmodell berücksichtigt sowohl Quetschfilm-Dämpfung durch freie molekulare Strömung als auch gaskinetische Dämpfung für den quasi-molekularen Bereich. Die Berechnung des Dämpfungskoeffizienten wurde unter Annahme einer freien molekularen Strömung durchgeführt. Der darauf aufbauende Algorithmus basiert auf einem Random-Walk-Modell, welches in Modellen der Direkten Monte Carlo Simulation Verwendung findet. Mit diesem Ansatz wurde die Güte eines Quetschfilm-gedämpften Kragbalkens im quasi-molekularen Bereich hergeleitet. Die daraus resultierenden Ergebnisse wurden mit aktuellen stochastischen Modellen verglichen. Die theoretischen Vorhersagen und die experimentellen Untersuchungen zeigen dabei markante Unterschiede der Knudsen-Zahlen bis 10. Eine Überlagerung beider Dämpfungsmechanismen, der gaskinetischen und Quetschfilm-Dämpfung, zeigt jedoch eine zufriedenstellende Charakterisierung des Dämpfungsverhaltens eines schwingenden Kragbalkens im quasi-molekularen Bereich mit Knudsen-Zahlen von 0,02 bis 10. In dieser Arbeit wurden die Oszillationen des Kragbalkens sowohl mit einem dafür eigens entwickelten, kapazitiven Detektionsverfahren als auch mit einem kommerziellen Laser-Doppler Vibrometer gemessen. Durch die Änderung des Leiterbahnstromes kann der Messbereich des Magnetometers von ein paar hundert nT bis ca. 10mT variiert werden. Dabei bleibt die Empfindlichkeit mit einer Unsicherheit von weniger als einem Prozent für alle drei Schwingungsmoden konstant. Höhere magnetische Flußdichten, wurden mit Permanentmagneten erzielt (max. ca. 300 mT). Das Funktionsprinzip dieses Prototyps ermöglicht eine weitere Miniaturisierung. Die räumliche Auflösung der Magnetfelder ist dabei nur durch die Größe des Kragbalkens bestimmt. Außerdem eignet sich das Heterodyne-Detektionsverfahren mit MEMS, hohe AC-Ströme berührungslos durch Messung der damit verbundenen AC-Magnetflussdichten zu bestimmen.

Abstract

A Lorentz-force actuated cantilever used as a magnetometer detecting both static and alternating magnetic fields is described. The device consists of a U-shaped single-crystal silicon cantilever manufactured in silicon-on-insulator (SOI) technology. The cantilever is placed in a vacuum chamber surrounded by a pair of coils configured as Helmholtz coil which generates the magnetic field. The test structures are harmonically excited by the Lorentz force acting on the gold lead at the top surface of the cantilever carrying an alternating current, where the deflections of the cantilever are a measure of the magnetic flux density. In the case of a sinusoidal magnetic flux density, the resulting Lorentz force contains two alternating terms including the sum and difference of current and field frequencies. Therefore, the resonating cantilever is used as mixer in a heterodyne detector for alternating magnetic fields with variable frequency. Resonant excitation only occurs if one of these frequencies is close to a mechanical resonance that satisfies the selection rule imposed by the field configuration. In the experiments, emphasis is laid on the investigation of the first symmetric, the first antisymmetric mode and the second symmetric vibration mode, where the amplitude of the vibration is proportional to the exciting vector component of the magnetic field. The sensitivity of a resonator is most affected by the quality factor Q. Since the reasons of the quality factor Q are versatile, especially in rarefied gas regimes, mechanical quality factors Q were analyzed at controlled ambient pressures in the range of 0.01 Pa to 100 Pa. The experimental results were compared with existing theories revealing an underestimate of the damping parameter for the Knudsen range $Kn = 0.1$ to 10. So far, squeeze-film damping by free molecular flow and kinetic damping were taken into account in damping models for the quasi-molecular regime. However, the measurements indicate that also the ongoing molecular flow around the test structures has to be considered. Hence the damping coefficient has to be calculated with methods of the free molecular aerodynamics. Thus, we used an algorithm based on the random walk model that allows the usage of already available knowledge in the field of Direct Simulation Monte Carlo. With this approach the quality factor of a squeezed-film damped cantilever in the quasi-molecular regime was derived. The results were compared with the most recent stochastic model, where the theoretical predictions and the experimental investigations indicate significant squeezing up to a Knudsen number of 10. In a superposition of both damping mechanisms, kinetic and squeeze-film damping, a satisfactory characterization of the damping behavior of an oscillating cantilever in the quasi-molecular regime with Knudsen numbers in the range of 10 down to 0.02 was achieved. For this work the harmonic deflection of the cantilever was measured with a capacitive readout system and additionally, with a laser-Doppler vibrometer. By changing the drive current, the operating range of the magnetometer can be varied from a few hundred nT up to approx. 10 mT, whereas the sensitivity remains constant with an uncertainty of less than one percent, valid for all three vibration modes. For higher magnetic flux densities, a sample of appropriate permanent magnets was used, so that the achieved maximum flux density was around 300 mT. The operation principle of this prototype allows a further miniaturization leading to a spatial resolution of the magnetic field detection determined by the size of the cantilever. It is worth mentioning that the heterodyne detection method with the MEMS device is also suited to measure AC high current flows contactlessly measuring the related AC magnetic flux density.

Contents

Part I

Start

CHAPTER **1**

Introduction

Overview

The recent work deals with the design, fabrication and implementation of a resonant magnetic field sensor. Due to the large number of magnetic measuring principles and techniques, it is necessary to give an overview, to summarize the state of the art and to explain the pros and cons of used commercial sensors.

1.1 Progression of Magnetism and their Detection Techniques

The dynamic effect of magnetite[1] was already described by Thales of Miletus in the ancient Greece in the 6$^{\text{th}}$ century B.C. [1]. The name magnet is due to the location of Magnesia, an anient Greek city. In the 3$^{\text{rd}}$ century before Christ the first compass was developed in China [2]. This technical achievement represents the first magnetic field sensor interacting with the earth's magnetic field. Obviously a compass is a navigational instrument, representing one of several possible applications of magnetic field sensors. A spoon carved from magnetite provides the magnetic compass. This rotatable spoon was placed on a smooth plate made of bronze whose handle always adjust to the south, which denotes Si'Nan in Chinese (Fig. 1.1).

Between the 4$^{\text{th}}$ and 10$^{\text{th}}$ centuries A.D. the Si'Nan was replaced by iron objects, e.g. by a needle. With the improvement on the functionality of the device, e.g. with a buoyant compass needle, the knowledge of the remanence of iron-made components was discovered. Remanence means that the device made of iron becomes a magnet if it is rubbed at a magnetide or heated up to red heat and then quickly cooled down. In Europe the buoyant compass needle was first mentioned by the English scholar Alexander Neckam in 1187 [4]. In 1492 Columbus discovered the magnetic declination, which means the deviation between the geographical and the mag-

---

[1]Magnetite is an iron oxide mineral ordered in the cubic crystallization system with the chemical formula $Fe^{2+}(Fe^{3+})_2O_3$.

Figure 1.1: The device described in this figure is considered to be the earliest form of a magnetic compass [3].

netic north direction. The magnetic inclination[2] was first described by Georg Hartmann from Nürnberg in 1543 [5].

Systematic studies of William Gilbert, such as with a spherical magnet, which he called "terrella" resulted in his magnum opus with the title "De Magnete, Magnetisque Corporibus, et de Magno Magnete Tellure" (1600 A.D.). For two centuries it was the most important systematic study regarding magnetism and it tooks a long time to recognize that magnetism and electricity are related phenomena, but of different origin since magnetism represents another manifestation of electricity. The magnetic effect of an electric current to a magnetic needle was shown experimentally by Hans Christian Oersted in 1820. He demonstrated the movement of the compass needle nearby a current carrying conducter loop. The primary law, which describes the connection between electric current and magnetism, is the Biot-Savart law discovered in 1820. André-Marie Ampère describes the reason of solid state magnetism using microscopic ring currents. In 1831 Michael Faraday discovered the law of induction (Faraday's law). The definite formulation of the electromagnetic interaction was established by James Clerk Maxwell in the year 1862.

The microscopic explanation of the magnetism kept the best known physicist of the early 20th century busy, such as Albert Einstein (special relativity and magnetism), Paul Langevin, Pierre Curie und Pierre Weiss (theory of Para-, Dia- und Ferromagnetism). With the help of quantum mechanics, George Uhlenbeck and Samuel Goudsmit (hypothesis of the angular momentum of an electron, the so-called "'Spin"'), Werner Heisenberg (theory of spin-spin interaction, a quantum mechanical explanation of the magnetic order in magnetic materials) and the systematic studies of antiferromagnetism by L. Néel completed the theory of magnetism.

Parallel to the fundamental research of the phenomenon magnetism, many physical effects which are of great importance for the operating mode of magnetic sensors were discovered. The working principle of magnetic field sensors is based on the effect of the magnetic field on hard or soft magnetic materials or other solids, like semiconductor or resistance films (Fig. 1.2). Technically relevant sensors for medium-sensitivity applications are magneto-resistive sensors

---

[2]This is the incline of the geomagnetic field to the horizon sphere.

(XMR-thin-film sensors), Hall sensors and induction driven magnetic field sensors. **Magnetoresistive sensors** (AMR-sensors) change their electrical resistance due to the influence of the magnetic flux density. Magnetoresistance was first described by William Thomson[3] in 1856.

$$R = R_0 \cdot \left[1 + \cos^2\theta(H)\right],$$ (1.1)

where R_0 is the electric resistance without an ambient magnetic field, H is the magnetic field and θ is the angle between the electric field and the electrical current density through the specimen.

```
                    ┌──────────────────┐
                    │ Magnetic Field   │
                    │     Sensors      │
                    └──────────────────┘
           ┌──────────────┐          ┌──────────────┐
           │ Magnetometers│          │  Gaussmeters │
           └──────────────┘          └──────────────┘

                                      • Hall Effect
                                      • Magnetoresistive
           ┌─────────┐  ┌─────────┐   • Magnetodiode
           │ Vector  │  │ Scalar  │   • Magnetotransistor
           └─────────┘  └─────────┘   • NMR
                                      • Rotating Coil
  • Fluxgate          • Nuclear Precession
  • SQUID             • Optically Pumped
  • Magnetoresistive
  • Fiber-Optic
  • Search Coil
```
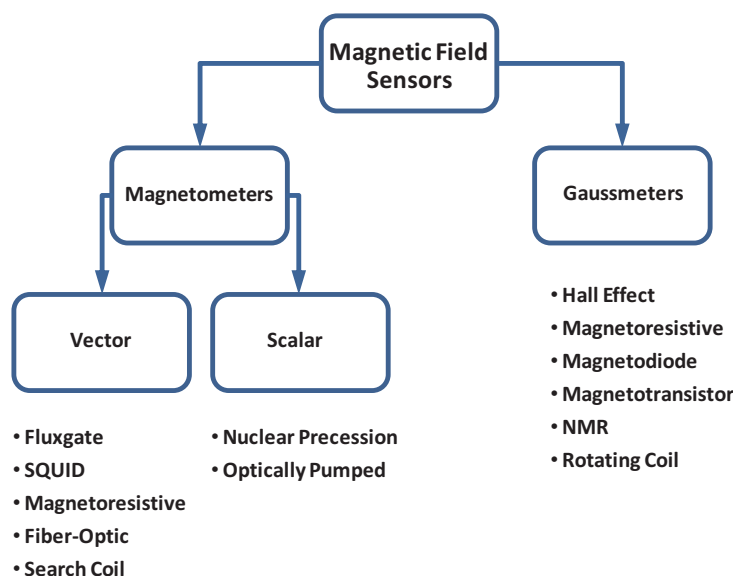
Figure 1.2: Magnetic field sensors can be separated depending on their field strength and their measurement range: magnetometers measure low fields whereas gaussmeters are able to measure high fields [6, 7].

The **Hall sensor**, often addressed as Hall probe is a totally different type of sensor regarding its working principle. If a current flows through a Hall probe while a magnetic field vertically to the current flow passes the sensor, the device delivers an output voltage across the probe, perpendicular to the electrical current density which is proportional to the product of the magnetic field strength and the electrical current. If the value of the current is known, the magnetic field strength is directly proportional to the measured Hall voltage. This is the so-called Hall effect, where Hendrik A. Lorentz gave an explanation for the voltage due to the movement of the charge carriers in the magnetic field (Lorentz-force). The macroscopic effect of the Lorentz force on a current carrying conductor with the length l in a magnetic field leads to

$$\vec{F}_\mathrm{L} = l \cdot \vec{i} \times \vec{B},$$ (1.2)

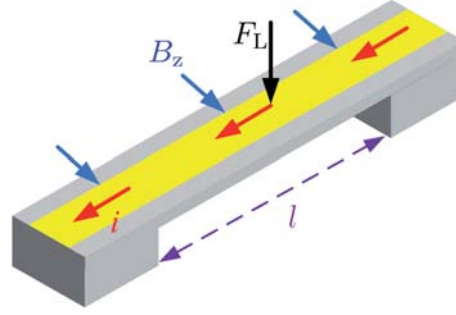[3]Better known as Lord Kelvin.

Figure 1.3: Schematic of the load acting on a current carrying clamped-clamped beam, due to the Lorentz force acting on the lead on the top of the structure.

where i is the electrical current in the lead on the top of the structure and B the magnetic flux density (Fig. 1.3). This linear relationship makes the Hall probe an ideal candiate for a magnetic sensor. However, there exist two severe drawbacks. Firstly, the temperature dependence of the Hall voltage due to the charge carrier density of doped semiconductors and secondly the offset voltage. The latter varies with temperature and time, which is vulnerable to different drift mechanisms that can completely mash the measurement effect. Many applications are not accessible to AMR and and Hall sensors because they are not as sensitive as Fluxgate sensors and SQUID's[4] due to their inherent noise level. SQUID's consist of two superconductors (e.g., niobium) that are separated by a thin insulating layer of approximately 1 nm, like aluminum oxide (Josepheson junction). If the temperature of the junction is decreased below the critical temperature, a superconductor current will flow through the junction. The magnitude of the current through the tunnel effect is a periodic function of the magnetic flux. One disadvantage of SQUID's is that up to now they depend to low temperatures due to the used tunnel effect through superconductivity. Although SQUID magnetoemeters are most sensitive instruments in measuring magnetic fields, they only detect the change of the magnetic field and not its absolute value [6].

Induction driven magnetic field sensors like search coils, rotating coils or Fluxgate sensors are based on the Faraday induction law

$$U_{\mathrm{i}} = N \frac{d\Phi}{dt} \,, \tag{1.3}$$

where U_{i} is the induced voltage in a coil with N windings, due to the temporal change of the enclosed magnetic flux Φ. Equation (1.3) can be rewritten as

$$U_{\mathrm{i}} = N \frac{d(B \cdot A)}{dt} = N \frac{d(\mu_0 \mu_{\mathrm{r}} H \cdot A)}{dt} \,, \tag{1.4}$$

and

---

[4] Abbr. for Superconducting QUantum Interference Device.
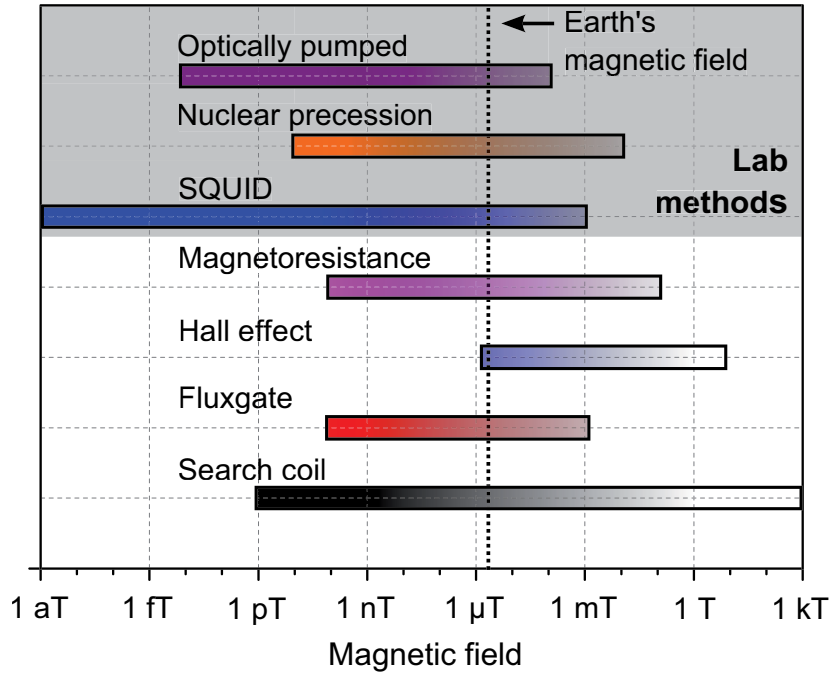
Figure 1.4: Typical measurement range of different magnetic field measurement methods [6, 8].

$$U_{\mathrm{i}} = N A \mu_0 \mu_{\mathrm{r}} \cdot \underbrace{\frac{\partial H}{\partial t}}_{\text{Search coil}} + N \mu_0 \mu_{\mathrm{r}} H \cdot \underbrace{\frac{\partial A}{\partial t}}_{\text{Rotating coil}} + N A \mu_0 H \cdot \underbrace{\frac{\partial \mu_{\mathrm{r}}}{\partial t}}_{\text{Fluxgate}} , \qquad (1.5)$$

where H represents the magnetic field to be measured, A is the cross section of the coil and μ_{r} describes the relative permeability. Search coils would provide a wide measurement range, but are limited to magnetic AC fields (see Eq. (1.5)). Fluxgate sensors consist of magnetically soft cores[5] (e.g., nickel-iron alloy), which are surrounded of two detecting coils (primary and pick-up coil). There are several fluxgate magnetometer architectures, e.g. residence times difference fluxgates-RTD and second harmonic fluxgates [9, 10].

Second harmonic fluxgate detect the second harmonic of the output voltage in the pick-up coil. A periodic driving current (e.g., sine, pulse, triangular waves) is applied in the primary coil, wound around the core and generates a periodic magnetic excitation field. The pick-up coil senses the flux change according to Faraday's law. In the case of an external magnetic field the core permeability alternates from a low value to a high value and produces voltage pulses at the pick-up coil, where the frequency of the signal is twice of the primary drive frequency since the transitions due to saturation occurs twice in each excitation period [6]. The amplitude of the

---

[5]Abbr. cores with a abrupt hysteresis curve with a very high permeability, so that the probe reacts to smallest changes particularly sensitively.

output signal is proportional to the magnitude of external magnetic field, whereas the phase is a measurand for the direction of the field.

Residence times difference fluxgates detect the time difference of two successive peaks in the pick-up coil. The time difference represents the time spent by the core magnetization in the two stable steady states. In the absence of an external magnetic field the time difference is zero. In the presence of an external magnetic field the hysteresis loop skew, and the time positions of the stable states vary.

1.2   Micro Electro-Mechanical Systems

Microelectromechanical systems (MEMS) are compact integrated systems that combine electrical and mechanical components. Their size can vary over a wide range from the sub micron up to the millimeter level. Furthermore, there can be any number, from a few to several millions, in a particular system. MEMS technology uses not only the fabrication techniques that were developed for the semiconductor industry but also adds mechanical elements such as beams, gears, and diaphragms to the devices. There are various examples of MEMS device applications including inertial sensors, micromirrors, microactuators, optical scanners, fluid pumps, pressure and flow sensors, and many more. The development of new applications is closely linked to the miniaturization and integration of conventional devices. These systems are able to sense, control, and activate mechanical processes on the micro scale, but also to generate effects on the macro scale. Micromachined devices often perform individually simple tasks, but in combination with each other they can achieve sophisticated functions. MEMS are neither defined by a single fabrication process, nor they are limited to a few materials. They are a result of a fabrication approach using the advantages of miniaturization and integration of multiple components and microelectronics. Hence, MEMS can have a significant impact on commercial markets, e.g. for mobile communications. Since the mid 1970's, the complexity of integrated circuits (ICs) has doubled every one and a half year. The dimension of manufactured devices and assembled in an IC has decreased from 20 microns down to currently 22 nm, where the leading-edge technology enables the fabrication of more than 1.4 billion transistors on a chip (Intel, Ivy Bridge processor-2012). Especially IC fabrications for mobile communications are the driving force for the development upon sensors and are responsible for their mass production. Similarly, control systems need actuators to accomplish their desired functions. In summary, there are three characteristics featured by MEMS's fabrication technologies: miniaturization, multiplicity, and microelectronics.

Micromachined Resonant Sensors

Independent of the working principle of the sensor, one has to distinguish between passive (e.g., magnetoelastic sensors) and active sensors, depending wether the sensor needs an external energy supply or not. If an external energy source is necessary for the conversion of the measurand, it is a so-called modulating sensor because the output signal depends both on the power supply and on measurand itself (e.g., Hall probe).

Assuming the property of the sensor is to provide an electrical output signal, containing the information of the measurand or rather his change, it is obvious that this direct conversion is only one aspect of the measurement problem. But usually the sensor principle consists of a multi-stage conversion from the input quantity to the output signal. As a result, more than only one quantity is involved during the conversion process. A typical quantity is the mechanical eigenfrequency of a vibrating structure. Sensors that detect the natural frequency or its change are called resonant sensors [11]. Thereby, the measurand is represented as a change or shift of the resonance frequency. Compared to other analog quantities, the frequency as output signal provides many advantages. A usual way to measure the quantity frequency is to count the number of cycles per unit time, which can be easily digitized, providing easy access to modern techniques of digital signal processing. Additionally, the frequency is directly attributed to the base item time and thus accessible with an excellent accuracy. The degradation of the resolution during the conversion, e.g. from a mechanical to an electrical signal are minimal, wherein the transmission reliability of an analog frequency signal from the sensor to the electronics is high. Simultaneously, these output signal is nonsensitive due to fluctuations of the signal amplitude and the drift of the reference potential. Beside the frequency, resonant sensors additionally offer many possible measuring quantities, such as amplitude, phasing, damping and individual signal shape. In general, these quantities include a different, but very important information about the measurement system, which contributes to a deeper understanding of the complex systems. One big disadvantage of resonant sensors is their limited time resolution because of their dependence due to the time constant τ of the oscillation and the quality factor Q.

Micromachined resonant sensors may work like tuning forks. Natural frequencies of the resonators are well-reproducible. Depending on the design of the sensor the structure can vibrate in different modes. This often results in a specific detection method. The kind of clamping and the shape of the resonator must be selected carefully, so that undesirable modes of vibration and its harmonics are either suppressed or have a frequency, which is far enough away from the desired resonant frequency. Beside the selected sensitivity, several different influences have to be considered in the design process. Regarding to the resonance frequency and according to the measurand, influences of the ambient like temperature changes or the change of the ambient pressure have to be considered for the design. Therefore all couplings of the sensing element to the environment that can influence the vibration that must be of interest for the applications of micromachined resonators. Due to the miniaturization of the sensor, a low mechanical energy is stored in the vibration mode, where various types of energies (e.g., thermal, acoustic, etc.) can be of the same order of magnitude. Hence, a insufficient signal-to-noise ratio of oscillations can result if the design of the sensor is not done carefully [12].

Both the excitation and the detection of oscillations can be realized electrostatically, magnetically, piezoresistively, piezoelectrically, thermally or optically, wherein the micromachined resonators can exhibit functional thin-film layers. Micromachined resonant sensors are used as force, inertial and pressure sensors, whereas the resonator oscillates and the measurand changes the resonance frequency, the amplitude or phase. The great advantage of resonators is the resonance amplification if the exciting frequency and natural frequency are close together. Such sensors respond much more sensitive to harmonic excitations than an equivalent broadband sensors (see Chapter 2.1).

Another possible description of a mechanical resonator is that a propagating mechanical wave through a geometrically limited structure creates a stationary wave, whose resonant frequency is simultaneously determined by the propagation speed of the wave and the geometric dimension of the structure itself. Accordingly, the resonance frequency can be influenced only in two ways: Firstly, the change of the propagation velocity of the wave (e.g., possible modes) or secondly, by a change of the material or by the structure itself.

Technically, micromachined resonant sensors, acoustic microsensors and ultrasonic sensors are of most importance. Micromechanical sensors are often fabricated with single-crystalline silicon, which has superior mechanical properties with regard to elastic parameters. These properties permit reproducibility and long-term stability better than other materials [13]. Furthermore, silicon-based production enables an integration of microelectronic and micromechanical components. Beside the mechanical characteristics of single-crystalline silicon, the high thermal conductivity (see Table 4.1) and the ability to manipulate electrical conductivity through doping enables a wide field of application [14].

1.3   Resonant Magnetic Field Sensors

The use of micromachined, resonant magnetic field sensors is adequately described in literature [15–25]. Nevertheless, these studies differ both in the sensor concept and in the detection method, which is summarized in Table 1.1. The most important part of a MEMS resonant sensor is the oscillating mechanical structure, which directly affects the characteristics of the sensor itself, such as accuracy and fabrication complexity.

Mechanical Design

In recent years, various resonator designs have been proposed, tested, and manufactured. They can be classified by their basic mechanical design: cantilevers, bridges and comb structures.

- **Cantilevers** represent the simplest structure in terms of manufacturing and function (see Fig. 1.5). The beam is fixed at one end to the substrate while the other end is free to move. If the cantilever is actuated, the free end oscillates in a mode depending on the eigenfrequencies of the structure. Therefore out-of-plane, in-plane and torsional mode shapes are possible. Because of the simplicity of such a design, it has several advantages for the engineer: Firstly, a simple mechanical design normally results in a simple fabrication process, which in turn leads to low production costs. Secondly, since one end of the beam is not anchored to the substrate, the possibility to introduce residual stresses into the structure during manufacturing is negligible. At last, due to the simple geometry the mode shapes can be characterized analytically using elementary beam bending theory, where the vibrations of cantilevers have been extensively studied.

- The **U-shaped structure** is a kind of folged bridge, but without tensile stresses. This shape provides a larger width to stiffness-ratio than standard cantilevers, making such devices more compliant to forces applied to its base.

(a) Cantilever

(b) U-shaped Cantilever

(c) Torsional plate
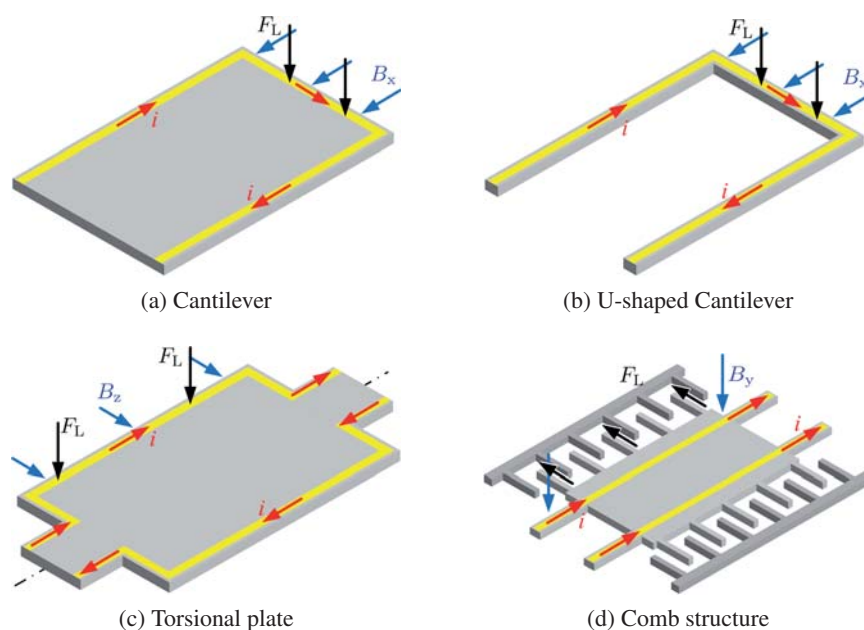
(d) Comb structure

Figure 1.5: Schematics of principle mechanical resonator designs regarding magnetic field sensor with electromagnetic actuation used in literature.

- A **clamped-clamped beam** resonator is a structure, where the vibrating mass fixed at two points. This architecture is very flexible due to the mechanical layout and functionality, and results in many variations of this basic structure, e.g. U-shaped cantilevers. Usually the oscillation is laterally and in an antisymmetric (AS) mode.

- The fourth fundamental MEMS resonators design is the **comb structure** architecture. This concept is most complex, but offers a very flexible design. It offers the same stability regarding the resonance mode as the clamped-clamped design.

Depending on the excitation of the mechanical structure three bending shapes are possible: If the structure bends such that the plane of the loading is parallel to the axis of the beam passing through its center of gravity, then the bending is known as in-plane bending. Otherwise it is called out-of-plane bending, due to the effects of twisting and lateral forces perpendicular to the plane of loading.

Actuation and Signal Transduction

The heart of a MEMS resonant sensor is a vibrating mechanical structure, but the structure do not resonate spontaneously. An actuation mechanism is necessary, which sets the structure to resonance, where a phase change occur. Several methods are possible, but in the MEMS field most popular and widely used are capacitive, piezoelectric, thermal, photothermal and magnetic techniques [28–34].

Table 1.1: Overview of Lorentz-forced, resonant magnetic field sensors. Following abbrevations are used: $c - f$ ... clamped-free, $c - c$ ... clamped-clamped.

Authors et al.	Deflection	Read-out	Clamping	Shape
Donzier (1991)[15]	out of plane	piezoresistive	$c - f$	cantilever
Eyre (1997)[16]	out of plane	piezoresistive	$c - c$	torsion/bridge
Kadar (1998)[26]	out of plane	capacitive	$c - c$	torsion/bridge
Emmerich (2000)[18]	$in - plane$	capacitive	$c - c$	comb
Leichle (2001)[27]	out of plane	capacitive	$c - f$	cantilever
Beroulle (2003)[19]	out of plane	piezoresistive	$c - f$	$U - shape$
Keplinger (2004)[20]	out of plane	optical	$c - f$	$U - shape$
Sunier (2006)[21]	out of plane	piezoresistive	$c - f$	$U - shape$
Bahreyni (2007)[22]	$in - plane$	capacitive	$c - c$	comb
Herrera (2009)[23]	out of plane	optical	$c - f$	cantilever
Choi (2011)[24]	$in - plane$	inductive	$c - c$	$comb - disk$
Herrera (2011)[25]	out of plane	piezoresistive	$c - f$	cantilever

Capacitive Actuation: Any electric charge is surrounded by an electric field and this electric field applies a force to any other charged particle. The drawback of the electrostatic force is that it decreases with the square of the distance between the two electric charges. In the MEMS world however, at microscopic scale, the distances between structures are very small. As a result, the electrostatic force can most efficiently affect the dynamic behavior of the resonator. Thus, electrostatic actuation is often used in microresonators, switches, micromirrors, accelerometers, and microactuators. An electrostatic force can be generated on a capacitor arrangement by applying an electrical voltage. Neglecting stray fields, the force between two parallel plates is

$$F = \frac{1}{2} \frac{\varepsilon A}{d^2} U^2 \tag{1.6}$$

where d is the equilibrium distance between the two plates, A is the area of the plates and U is the applied DC-voltage. As a result of Eq. (1.6) the only design parameters of the electrodes are the area A of the plates and the distance d between the electrodes.

Piezoelectric Actuation: Piezoelectric materials can be deformed in specific directions by applying an appropriately oriented electric field. Through these inverse piezoelectric effect, a conversion of electrical power into mechanical motion is achieved.
Piezoelectric materials are characterized by their piezoelectric coefficient, which quantifies the volume change, when the material is exposed to an electric field or mechanical stress. If the clamped piezoelectric material is stressed, the deformation of the lattice structure will cause a separation of charges, which thus generate an electric field across the material. At the other side a potential difference will generate a mechanical deformation through the material. This working principle can be used to excite mechanical oscillations by applying a sinusoidal driving

voltage to a piezoelectric material coupled to the resonator. If the piezoelectric layer on the resonator expands and contracts harmonically the steady-state response of the resonator will also be periodically. Like the capacitive method, piezoelectric devices can be used both as transducer for the mechanical oscillations and driving actuator.

Magnetic Actuation: Typical implementations are flexible structures with a load on its surface, which are placed in an external magnetic field. The current in the lead generates a Lorentz force, which in turn provides a tunable form of actuation. The motion of a conductor through the magnetic field, induces a response-dependent electromotive force (emf). This force can directly be used to recover the response of the system, for e.g., feedback purposes, or as a basis for electromagnetically coupled oscillators. The magnetic actuation is not only limited to the Lorentz force, it can also be realized by magnetostrictive materials. These materials change their shape when they are exposed to magnetic fields (e.g., Nickel, Terfenol-D, etc.).

Read-out

An important aspect of any sensor design represents the applied read-out (see Table 1.1). In the early publications of Donzier (1991), Eyre (1997), Beroulle (2003), Sunier (2006) and Herrera (2011) [15, 16, 19, 21, 25] a piezoresistive read-out was used, where the sensor was, on the one hand [15, 35] a simple cantilever and on the other hand [19, 21] a much more sophisticated U-shaped cantilever. Furthermore, in the publications of Kadar (1994) and Emmerich (2000) [17, 18], both authors chose a capacitive read-out, where Kadar et al. (like Eyre et al.) designed a torsional brigde detecting the antisymmetric vibration modes of the excited structure.

Emmerich et al. [18] used a micromachined comb structure measuring in-plane displacements. An optical read-out was only used by Keplinger et al. (2004) and Herrera et al. (2009) [20, 23] detecting flexural vibration modes of the test structures. Bahreyni et al. (2007) and Choi et al. (2011) introduced a totally different detecting concept, where the fundamental resonant frequency of the structures is modified by a Lorentz force generated from the interaction of the device and the ambient magnetic field [22, 36].

In this thesis, a U-shaped cantilever was addressed because this design provides a larger width to stiffness ratio than plates, resulting in an increased sensitivity due to to external exciting forces. The selected capacitive read-out system was designed to distinguish between symmetric and antisymmetric modes. The advantage of this design is that simultaneously with respect to the sensor position and orientation, two magnetic field components are detectable. Additionally, the developed transduction and signal processing allows to detect both static and alternating magnetic fields. In the case of alternating magnetic fields it has turned out that the structure is suitable, e.g. to measure high AC currents contactless by measuring the related AC magnetic flux density. In addition to the capacitive magnetic field transduction, the same arrangement turned out to be an efficient actuation scheme for the micromechanical resonator. It could provide large vibrations without direct physical contact between the resonating proofmass and the electrodes. If the resonator design is carefully optimized by reducing particularly intrinsic damping mechanism (e.g., anchor losses, Chapter 2.3), high performance of the device can be achieved.

Table 1.2: Main characteristics of Lorentz-forced resonant magnetic field sensors based on MEMS technology.

Authors et al.	$B_{\min}$ in µT	$B_{\max}$ in µT	Sensitivity	i in mA
Eyre (1997)	1000	30 000	20 mV/T	10
Kadar (1998)	50	600	500 mV/µ T	30
Emmerich (2000)	5	100	820 V/T	0.072−0.93
Leichle (2001)	2000	100 000	−	−
Beroulle (2003)	10 000	110 000	530 mV/T	−
Keplinger (2004)	−	200 000	−	
Sunier (2006)	1000	13 000	60 kHz/T	−
Bahreyni (2007)	2500	25 000	48−87 Hz/T	1−6
Herrera (2009)	500	30 000	530 nm/T	0.574
Choi (2011)	50	390	−	−
Herrera (2011)	50	2000	1.94 V/T	30

Table 1.2 lists literature dates of resonant magnetic field sensors. One can notice that the achieved minimum and maximum detectable fields are either in the range of the earth's magnetic field or much larger. In the last 20 years no researcher has characterized his sensor over more than two orders of magnitude regarding the magnetic flux density. The Lorentz force F_L provides a linear scalability of the conversion efficiency. The magnitude of the structure deflection depends on the Lorentz force itself, which in turn is directly proportional to the current i on the top of the structure and to the magnetic flux density B. Looking at Table 1.2, the excitation current is already quite large and a further increase would promote a thermal damage of the structure. Therefore, none of the presented structures seems to be suitable to detect smaller magnetic fields than those of Emmerich et al. But Emmerich did not explain how he achieves the lower bound of 5 µT. He gives no explanation how he compensated the Earth's magnetic field or other low frequency magnetic field disturbances. The maximum reposted magnetic flux density is 200 mT, although the Lorentz-force actuated cantilever would provide a direct measurement methode for high magnetic fields. Another important parameter is the frequency-quality factor-product $f_r \cdot Q$ given in Table 1.3 because this quantity is a direct measure for the combined action of all intrinsic damping mechanisms of the whole structure (see Chapter 2.3).

Parameters of a Resonator

The performance of a micromechanical resonator can be influenced by different parameters like ambient pressure or temperature. These different physical conditions can interfere with the natural vibration at resonance and may degrade the performance of the resonator. One of the most important parameters for a resonator is its quality factor (see Chapter 2.1). The quality factor Q can be influenced by several loss mechanisms, which can roughly be divided into intrinsic and extrinsic damping mechanisms. Hence, the design and the placement of anchor points will either improve or degrade the measured quality factor of the resonator. Especially,

Table 1.3: Further characteristics of Lorentz-forced resonant MEMS-magnetic field sensors ([†]atmospheric pressure).

Authors et al.	Resonance freq. f_r in kHz	Quality factor Q	$f_r \cdot Q$	Ambient pressure in Pa
Eyre (1997)	2.5	10	25	≈ 200
Kadar (1998)	2.5	700	1750	5
Emmerich (2000)	1.3	37	48.1	101
Leichle (2001)	1.218	–	–	–
Beroulle (2003)	8.97	59	529.2	–
Keplinger (2004)	4.82	–	–	atm[†]
Sunier (2006)	175	600	105 000	atm
Bahreyni (2007)	38.074	15 250	580 628	≈ 2 Pa
Herrera (2009)	19.4	1.66	32.2	atm
Choi (2011)	≈ 1.5	–	–	–
Herrera (2011)	22.99	96.60	2220.8	atm

for resonators with a capacitive position transduction their quality factor is inversely proportional to the motional resistance. Usually, the damping of this resonator should be small for an easier impedance matching with other integrated circuit electronics.

Beside the quality factor of a resonator, the pressure dependence of the device can be of interest, or how stable are the resonant frequency f_r and the quality factor Q under varying pressure. The performance of resonators with capacitive air gaps or air slits between the vibrating structure and fixed surfaces will deteriorate with pressure variations due to air damping. With an increasing collision frequency of air molecules, the resonator will be hindered during vibration. In the case of a diluted atmosphere, pressure stability of resonators is one of the essential features. Therefore, a clear, physical understanding of the behavior of resonators under different pressure regimes is of most importance (see Chapter 2.3).

A very important criterion for electromagnetic actuated resonators is power handling. How much power the resonator can withstand before its operating deviates from its desired design. These deviations in operation can lead to nonlinear regimes, where the nonlinearity of the resonator is associated with mechanical and electrical nonlinearities. Nonlinearities in continuum mechanics can be found mostly for large deflections or in the structure's geometry, whereas electrical nonlinearities are mainly determined by the capacitive readout system.

A very critical item in the context of electromagnetic actuation are changes of the temperature resulting in corresponding changes of the elastic properties. This can lead to a drift of the resonance frequency during the operation (see Chapter 4.3). Temperature stability is important for all oscillator applications, where a stable reference frequency is required. For mechanical reference oscillators a method for temperature compensation is necessary. On the other hand this resonant frequency drift with temperature can be useful for some applications such as for temperature sensors.

Aim of this Work

This thesis explores the performance of a resonant flexural-mode magnetic field sensor (both symmetric and antisymmetric modes). The performance of the device is analyzed with regard to the following key parameters: quality factor, pressure stability, temperature stability and non-linearity. Fundamentally, the overall performance of a resonator is mainly influenced by the geometry of the resonator. Whether the resonator is used for sensor-, oscillator- or filter applications, an optimized geometry for high performance under various pressures and temperatures is desireable. The focus of this work is on the quality factor in different pressure regimes, where one can observe that losses through anchor supports are the main energy losses especially for intrinsic, e.g. high vacuum damping mechansims. Interestingly enough, two different damping mechanisms dominate in the transition regime of the damping over ambient pressure characteristic: gas-kinetic damping and squeeze-film damping (see Chapter 2.3). This work also presents data concering the pressure and temperature dependence and nonlinearity of various flexural-mode micromechanical resonators. Moreover, a new idea for a MEMS magnetic field sensor characterization and a custom capacitive readout system will be presented. The following chapters will be presented in a strict distinction between mechanical and electrical domains and detection methods, shown in Fig. 1.6.
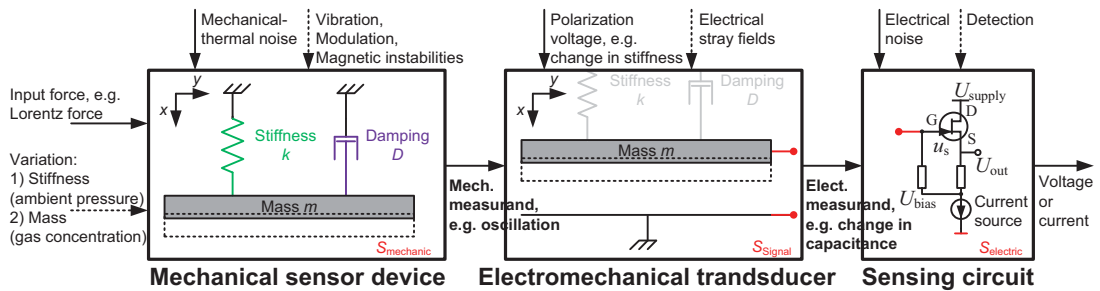
Figure 1.6: Classification of a microelectromechanical system in mechanical sensor device, electromechanical transduction and sensing circuit.

Part II

Middle

Mechanical Fundamentals of MEMS Sensors

Overview

This chapter deals with the mechanical description of the oscillations of MEMS resonant sensors, as shown in Fig. 2.1. The measurement principle is described on basis of a force sensor. Fundamental aspects are derived from well-known concepts, like the harmonic oscillator, where fundamental limits of the system will be discussed.
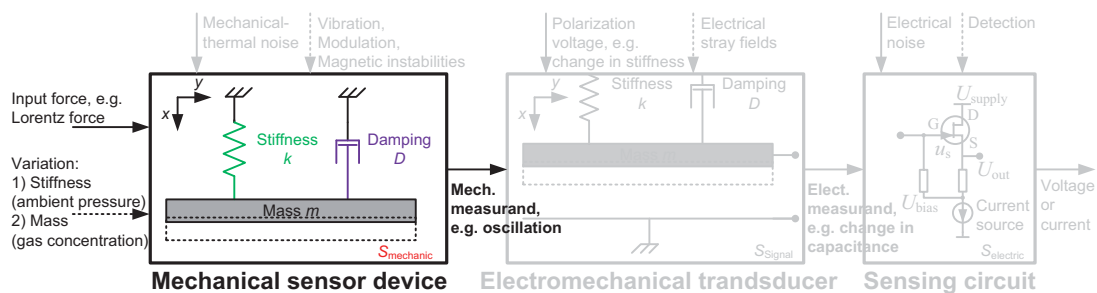
Figure 2.1: Typical structure of a microelectromechanical system. Hence, emphasis is laid on the mechanical part.

2.1 Frequency-Selective Detection Method

Measurement Principle

Normally, vibration sensors work below their resonant frequency because in this range the sensor signal is proportional to the quantity to be measured, whereat the deflection of the sensor is small

compared to the amplitude of the vibration (see Fig. 2.2). A pronounced resonance enhancement limits the proportional range of measurement and therefore, frequency components near the resonance are filtered out.
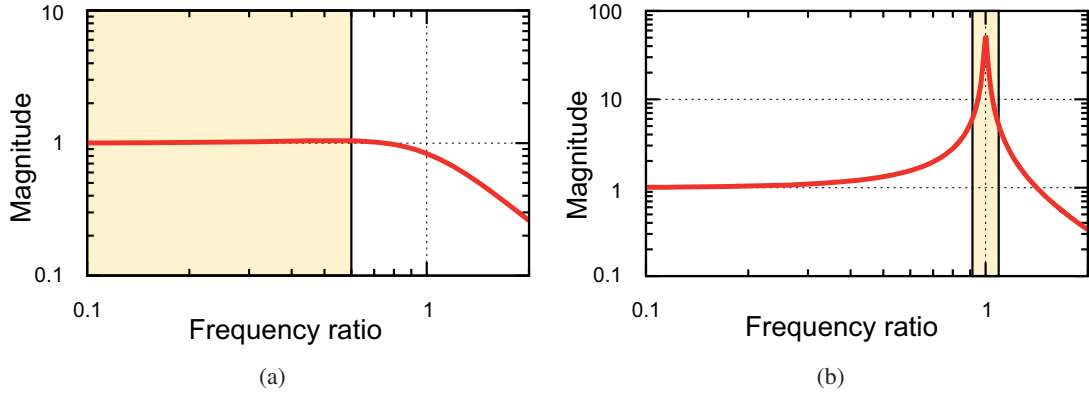
Figure 2.2: Vibration measurement principles demonstrated with Fig. (a) as broadband and Fig. (b) as frequency-selective PT2-system.

The frequency-selective sensor operates in contrast to a broadband sensor exactly at his resonance. It filters out the frequency components of the excitation around its resonance frequency, where the signal is amplified with the quality factor Q (see Fig. 2.2). Hence, the signal-to-noise ratio (SNR) increases because of the resonance enhancement. Interfering signals with large amplitudes beside the resonance are suppressed and do not overdrive the transducer.

Harmonic Oscillator

The study of cantilever oscillations is a rather extensive problem. In many cases the general solution of the cantilever equation of motion can not be obtained in an analytical form. However, if the deflections of the cantilever relating to the equilibrium position are small, Hooke's law is valid and the oscillations of the system can be described by basic theories, like the harmonic oscillator of a spring pendulum

$$F = m\ddot{x} = -kx \tag{2.1}$$

having a stiffness k and some effective mass m. This is a simple differential equation, where the equation of motion becomes

$$\ddot{x} + \omega_0^2 x = 0 \,, \tag{2.2}$$

where $\omega_0 = \sqrt{k/m}$ is the oscillator's angular eigenfrequency. For purposes of generality, the equation in z

$$\ddot{z} + \frac{k}{m\omega_0^2} z = 0 \,, \tag{2.3}$$

represents a nondimensional presentation of a harmonic oscillator, with the nondimensional time τ. If the natural angular frequency ω_0 of the oscillating system should represent the frequency unit, $k/(m\omega^2)$ is set to unity. The solution of Eq. (2.2) is

$$x(t) = A\sin(\omega t + \phi) \,, \tag{2.4}$$

where A is the amplitude of the oscillator and ϕ is the phase between excitation and vibration system. In the case of free oscillations, the amplitude and the phase are specified by the initial conditions

$$A = \sqrt{x^2(0) + \frac{\dot{x}^2(0)}{\omega_0}} \tag{2.5}$$

and

$$\phi = \arctan\left(-\frac{\dot{x}(0)}{\omega_0 x(0)}\right) \,,$$

while the frequency of a natural undamped oscillation is a parameter of the oscillating system [37]. In the case of free oscillations, where external forces are absent, natural oscillations are due to Eq. (2.4) harmonic. The total energy

$$E_{\text{tot}} = \frac{1}{2} m\omega_0^2 A^2 \tag{2.6}$$

stored in the harmonic oscillator at the inital state $t = 0$ is conserved and only its kinetic and potential energy parts vary over time.

Damped Harmonic Oscillator

In real systems dissipation of energy takes place, where the energy losses will damp the vibrations. Until these losses are not compensated from outside with a force F the oscillations will decay in time. These consideration leads to the simplest case of a damped harmonic oscillator with following equation of motion

$$m\ddot{x} + D\dot{x} + kx = 0 \,, \tag{2.7}$$

where D denotes the damping parameter of a viscous medium. The solutions of this homogeneous linear differential equation for free vibrations with constant coefficients have an exponential form $x = Ce^{rt}$. This general solution of Eq. (2.7) leads to the characteristic equation

$$mr^2 + Dr + k = 0 \tag{2.8}$$

with the two roots

$$r_{1,2} = \frac{1}{2}\left[-\frac{D}{m} \pm \sqrt{\left(\frac{D}{m}\right)^2 - \frac{4k}{m}}\right] \quad . \tag{2.9}$$

In the case of a vanishing discriminant of Eq. (2.9) the Damping of the system achieves a critical value

$$D_c = 2\sqrt{km} = 2m\omega_0 \tag{2.10}$$

the so called critical damping parameter D_c. The damping ratio $D/D_c \equiv \zeta$ denotes the dimensionless damping factor. Hence, the relationship between the damping parameter D and the the dimensionless damping factor ζ is

$$\zeta = \frac{D}{2\sqrt{mk}} . \tag{2.11}$$

With Eq. (2.10) the characteristic Eq. (2.9) can be rewritten to

$$r_{1,2} = -\zeta\omega_0 \pm \omega_0\sqrt{\zeta^2 - 1} \tag{2.12}$$

If $\zeta = 1$ the critically damped oscillator attempts to return to its equilibrium position, without any oscillations. The overdamped oscillator with $\zeta > 1$ also returns to its equilibrium position, but more slowly than in the critically damped case, which is shown in Fig. 2.3. In many MEMS applications ζ is smaller than 1, but positiv and the solution of the underdamped oscillator in Eq. (2.7) becomes

$$x = Ae^{-\zeta\omega_0 t}\sin\left(\underbrace{\omega_0\sqrt{1 - \zeta^2}}_{\omega_d}t + \phi\right) , \tag{2.13}$$

where ω_d denotes angular frequency of a damped system and ϕ is the phase angle. The damped angular resonance frequency characterizes the frequency of the free vibration at which the oscillator returns to its position of equilibrium and is therefore, often called natural angular frequency.

For a sensor with a resonant working principle the quality factor Q is of most importance to quantify the energy losses due friction. The Q-factor determines the sensitivity and the dynamic behavior of the sensor. If the dimensionless damping parameter $\zeta < 1$ in Eq. (2.13), there is only a slight difference between the damped angular resonance frequency ω_d and the the
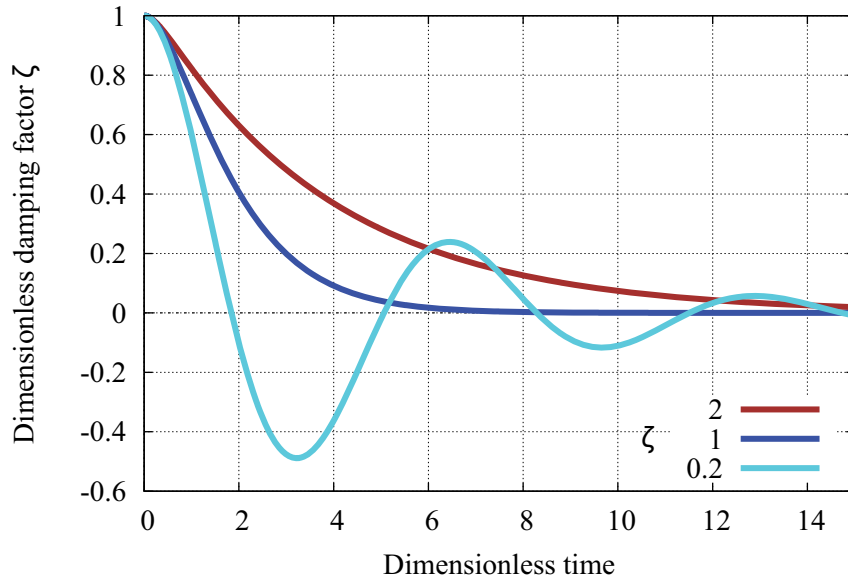
Figure 2.3: Free motion of a 1-DOF system for various damping parameters ζ.

eigenfrequency ω_0. A descriptive mathematical method for the quality factor Q is to compare the spring force to the damping force

$$Q = \frac{kx_0}{D\omega_0 x_0} = \frac{k}{2\zeta m\omega_0^2} = \frac{1}{2\zeta}.$$ (2.14)

For weak to moderate damping, the relationsship between the quality factor Q and the damping ratio ζ simplifies to

$$Q = \frac{m\omega_0}{D} = \frac{1}{2\zeta} = \frac{1}{\eta},$$ (2.15)

where η is the loss factor.

Driven Damped Harmonic Oscillator

If a harmonic driving force $F(t) = F\sin(\omega t)$ acts on a damped oscillator, the equation of motion becomes

$$m\ddot{x} + D\dot{x} + kx = F\cos(\omega t)$$ (2.16)

or in complex notation

$$m\ddot{\tilde{x}} + D\dot{\tilde{x}} + k\tilde{x} = Fe^{i\omega t}$$ (2.17)
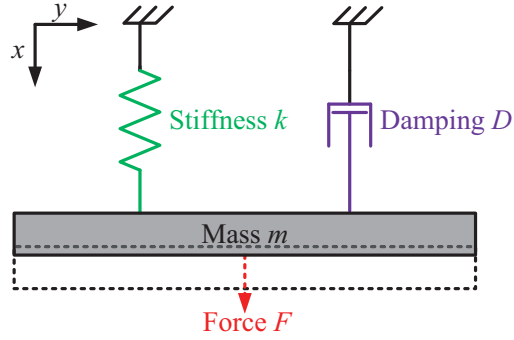
Figure 2.4: Simplified mechanical model of a single degree of freedom (1-DOF) system.

often called as single degree of freedom system (1-DOF) which is schematically shown in Fig. 2.4.

Owing to the harmonic function of the right hand side of Eq. (2.17), the left hand side should be in the steady state with the same frequency. Hence, the complex displacement $\tilde{x}$ can be replaced by $\tilde{A}e^{\mathrm{i}\omega t}$, where the complex form of Eq. (2.17) becomes

$$\tilde{A}e^{\mathrm{i}\omega t}\left(-m\omega^2 + \mathrm{i}\omega D + k\right) = Fe^{\mathrm{i}\omega t}. \tag{2.18}$$

Therefore, the complex displacement leads to

$$
\begin{aligned}
\tilde{x} &= \frac{Fe^{\mathrm{i}\omega t}}{k - m\omega^2 + \mathrm{i}\omega D} \\
&= \frac{\tilde{F}/m}{\omega_0^2 - \omega^2 + \mathrm{i}\omega 2\alpha},
\end{aligned}
\tag{2.19}
$$

where $\tilde{F} = Fe^{\mathrm{i}\omega t}$, $\omega_0^2 = k/m$ and $\alpha = D/(2m)$. The real part of the steady-state displacement of Eq. (2.19) is

$$x = \frac{F}{\omega Z}\sin(\omega t + \phi), \tag{2.20}$$

where $Z = k - m\omega^2 + \omega D$. In the case of a slight difference between the damped angular resonance frequency ω_d and the the eigenfrequency ω_0 because of a small damping parameter $\zeta < 1$ the amplitude of Eq. (2.19) gets
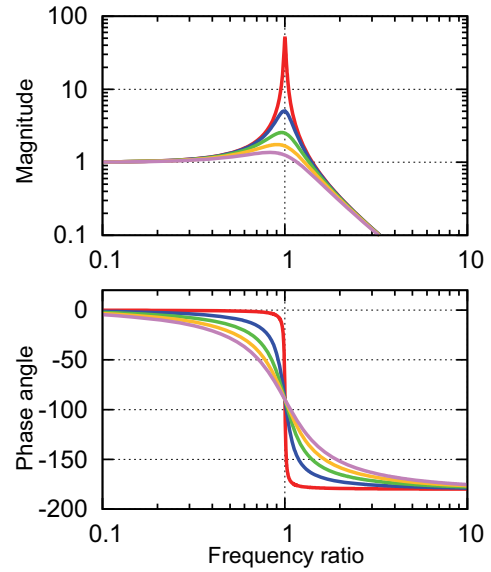
Figure 2.5: Frequency dependence of the magnitude x and the phase ϕ of a simple oscillator.

$$x_0 = \frac{F}{2\alpha m \omega_0} \,. \tag{2.21}$$

With Hooke's Law $F = k \cdot x_\mathrm{s}$ the static displacement of the oscillator due to the load with the magnitude F is at very low frequencies $x_s = F/k$ (see Fig. 2.2). Substituting $D = 2\alpha m$ in Eq. (2.14), $Q = \omega_0/(2\alpha)$ and hence the amplitude becomes

$$x_0 = Q x_s \,, \tag{2.22}$$

where Q acts as an amplification factor at resonance ($\omega = \omega_0 \approx \omega_d$). The phase angle ϕ of the denominator of Eq. (2.19) becomes

$$\phi = \tan^{-1} \frac{2\alpha\omega}{\omega^2 - \omega_0^2} \,, \tag{2.23}$$

representing the phase angle between the displacement x and the harmonic driving force F. The frequency response of a linear harmonic oscillator for different quality factors Q is shown in Fig. 2.5. Two important properties of the mechanical quality factor Q are:

- In contrast to an electronic amplification it requires no power supply, since no active components are involved.

- Thermomechanical noise drops at resonance with $1/\sqrt{Q}$ [38]. Hence, the displacement due to thermomechanical noise only raise with $\sqrt{Q}$, where the signal-to-noise ratio (SNR) improves with $\sqrt{Q}$ (see Chapter 4.3). However, the bandwidth of the sensor is simultaneously reduced by the amplification factor shown in Eq. (2.24). The decline of the SNR can be increased by decresaing the spring constants, according to Eq. (2.60).

Determination of the Quality Factor

Bandwidth Method: For low loss systems there is a direct relationship between the damping coefficient α and the width of the resonance peak. The denominator of Eq. (2.19) determines the shape of the resonance, where its magnitude increases by a factor of $\sqrt{2}$ relative to its amplitude at $\omega = \omega_0$ and in the case of $|\omega - \omega_0| \approx \alpha$ [37]. Similarly the response decreases with the same factor. Each of them represents a 3 dB half-width of the resonance curve, which is equal to the damping coefficient α. Together the full-width $\Delta\omega = 2\alpha$. Therefore, in the case of a weakly damped system it is possible to determine the quality factor using the bandwidth of the resonance

$$Q = \frac{\omega_0}{2\alpha} = \frac{\omega_0}{\Delta\omega} \approx \frac{\omega_r}{\Delta\omega} \,, \tag{2.24}$$

where ω_r is the angular resonance frequency and $\Delta\omega$ the angular bandwidth. If damping is small, the resonant angular frequency ω_r is nearby to the angular eigenfrequency ω_0 of the

system, which is the angular frequency of the unforced vibration of the structure. The angular bandwidth is the width of the frequency range ($\cdot 2\pi$) for which the energy is at least half its peak value. For the determination of the bandwidth the structure has to be excited around its natural frequency and the amplitude of the vibration of the structure has to be detected. If this is done sufficiently slowly at moderate amplitudes a Lorentzian profile will be achieved. Usually, the response is not exactly symmetric about the resonant frequency. When a slightly damped linear oscillator with $2\alpha^2 \ll \omega_0^2$ is excited with a driving angular frequency ω the oscillation amplitude is typically approximated by a formula that is symmetric about the resonant frequency $\omega = \omega_0$

$$x(\omega) = \frac{F/m}{\sqrt{(\omega_0^2 - \omega^2)^2 + 4\alpha^2\omega^2}} \approx \frac{F/2m\omega_0}{(\omega_0 - \omega)^2 + \alpha^2}$$

$$\text{with } \omega_0^2 - \omega^2 = (\omega_0 - \omega)(\omega_0 + \omega) \text{ and } \omega_0 + \omega \simeq 2\omega_0 \,. \tag{2.25}$$

The square of the deflection of Eq. (2.25) leads to

$$x^2(\omega) = x_0^2 \frac{\alpha^2}{(\omega_0 - \omega)^2 + \alpha^2} = x_0^2 \underbrace{\frac{(\Delta\omega/2)^2}{(\omega_0 - \omega)^2 + (\Delta\omega/2)^2}}_{\text{Lorentzian function}} \,, \tag{2.26}$$

where x_0, the height of the peak is specified in Eq. (2.21).
Under the assumption of natural frequencies in the range of $10\,\text{kHz}$ and an assumed resolution of $10\,\text{mHz}$, the maximum quality factor due to Eq. (2.24) should be $1 \cdot 10^6$.

Logarithmic Decrement Method: A common definition of the quality factor of a low damped mechanical system using energy considerations is

$$Q = \frac{2\pi E_i}{E_d} = 2\pi \frac{E(t)}{E(t) - E(t+T)} \,, \tag{2.27}$$

where E_i is the stored vibrational energy and E_d the dissipated energy per oscillation period T [39].
Another possible method to determine the quality factor is to measure the decay time τ of the oscillation, when the system is hit once and not driven. The total energy of a weakly linear damped oscillator (with a damping force proportional to the velocity) decrease exponentially

$$E(t) = E_0 e^{\frac{2t}{\tau}} \,, \tag{2.28}$$

where E_0 is the total oscillator energy at the moment $t=0$ and $\tau = 1/\alpha = 2m/D$ is the time constant of the decay. Due to Eq. (2.27) the quality factor per period T becomes

$$Q = 2\pi \frac{1}{1 - e^{\frac{2T}{\tau}}} \,. \tag{2.29}$$

For $\tau \gg T$ and a series expansion of the exponential function in Eq. (2.29) the quality factor changes to

$$Q = \frac{\omega\tau}{2} \,.$$

(2.30)

Under the assumption of natural frequencies in the range of $10\,\text{kHz}$ and a time constant of $1\,\text{s}$ the measurable quality factor is about $3 \cdot 10^4$. In conclusion, the bandwidth method and the logarithmic decrement method are both appropriate to determine the quality factor for structures with natural frequencies in the range of $10\,\text{kHz}$.

2.2   Modelling

Analytical and Numerical Techniques

The design of micro mechanical components is usually carried out in the synthesis of single simple geometric entities. The positions where these entities are connected together are called nodal points. In the static case the analysis of the physical behavior of all jointed structures is executed under the assumption of the equilibrium of forces in every nodal point and the compatibility of displacements of neighboring nodes. For those kinds of engineering problems a fistful commercial as well as open source programs are suitable, like COMSOL Multiphysics, ANSYS, Elmer or CalculiX. Finally, the possibilities of coupling different physical domains like mechanics with electrostatics or magnetostatics often rules the application.
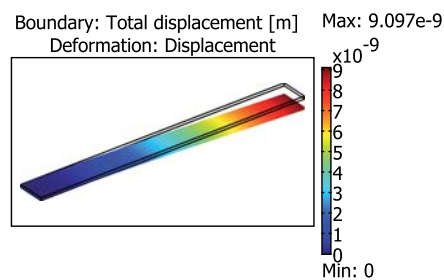
(a) Cantilever l=2mm, b=0.2mm
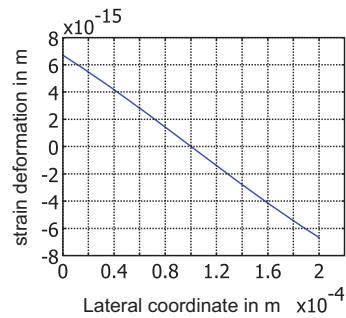
(b) Cantilever l=2mm, b=0.2mm
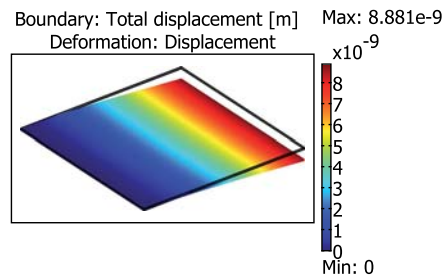
(c) Cantilever l=b=2mm
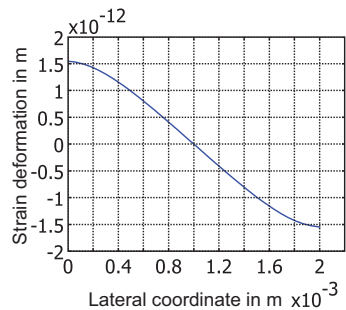
(d) Cantilever l=b=2mm

Figure 2.6: Two single-crystal cantilevers with the same length and height but with a mass ratio of ten, a stiffness ratio of one-tenth and their resultant static displacement in meter due to gravity. The abscissa in Fig. 2.6(b) and 2.6(d) represents the lateral coordinate at the tip of the cantilever.

Through the finite element method (FEM) design parameters can be optimized with a step by step approximation. This e.g. can lead to an optimization of the sensitivity of a quantity to be measured or in the suppression of higher vibration modes or to a low temperature dependence of the device. With the help of the finite element method the analysis of a very large number of equations in the particular nodal points is possible.

For example the static deflection due to gravitational forces of a simple silicon cantilever with the length of 2 mm and the height of 20 µm is 9 nm (see Fig. 2.6). As a first approximation, the deflection is independent from the width of the cantilever, althouth the mass of the structure in Fig. 2.6(c) is ten times higher than that in Fig. 2.6(a), but with a tenfold increase of the stiffness ratio.

Notably, the two solutions in displacement due gravity are not identical in Fig. 2.6(a) and 2.6(c). Due to Fig. 2.6(b) and 2.6(d) it is a result of shear deformations in the cross-sectional area of the plate, which is completely negligible in the cantilever. Vibrating cantilevers are described with the Euler-Bernoulli beam (continuum) equation of motion neglecting the deformations due to shear forces and the inertial resistance due to rotational acceleration of the cross-sectional area of the beam. More detailed beam theories, especially for plates often termed Timoshenko beam theories, lead to slightly different results especially for higher frequencies.

Euler-Bernoulli Beam Theory

In the simplest case, the equation of motion of an undamped flexural resonator can be described by the Euler-Bonoulli beam equation,

$$\frac{\partial^2}{\partial x^2}\left(\underbrace{EJ_z(x)}_{\text{bending stiffness}}\cdot\frac{\partial^2\Psi}{\partial x^2}\right) + \underbrace{\rho A(x)}_{\text{mass per unit length}}\cdot\frac{\partial^2\Psi}{\partial t^2} = \underbrace{q(x,t)}_{\text{transverse loading}} \qquad (2.31)$$

a partial differential equation of 4th order for the flexural deflection $\Psi = \Psi(x,t)$. The importance of stress and strain in vibrating structures has its reason in the dependence of the equation of motion of the resonator due to the Young's modulus E. This modulus describes the tensile elasticity or the tendency of a structure to deform along an axis when opposing forces are applied along that axis. The Young's modulus is defined as the ratio of the tensile stress to the tensile strain with the dimension of a force per unit area.

Many historic mechanics textbooks appreciate Galileo's analytical contributions towards beam theory like Timoshenko's synopsis in History of Strength of Materials [40]. However, one should be aware that Leonardo da Vinci made very fundamental experimental research and some theoretical contributions to Euler-Bernoulli beam theory 100 years before Galileo. For example he explained the product of the cross-sectional area A with the height h in proportion to the length of the beam correctly [41]. Fig. 2.7 is a detail of folio 84 of Codex Madrid I, a hardback of memos, drawings and paintings of da Vinci in the National Library of Spain. Carlo Zammattio refers in [42] to this detail, with following translation of Leonardo's notes:

Figure 2.7: Contributions of Leonardo da Vinci due beam bending theory in the Codex Madrid I.

"Of bending of the springs: If a straight spring is bent, it is necessary that its convex part becomes thinner and its concave part, thicker. This modification is pyramidal, and consequently, there will never be a change in the middle of the spring. You shall discover if you consider all of the aforementioned modifications that by taking part 'ab' in the middle of its length and then bending the spring in a way that the two parallel lines, 'a' and 'b' touch at the bottom, the distance between the parallel lines has grown as much at the top as it has diminished at the bottom. Therefore, the center of its height has become much like a balance for the sides. And the ends of those lines draw as close at the bottom as much as they draw away at the top. From this you will understand why the center of the height of the parallels never increases in 'ab' nor diminishes in the bent spring at 'co." In contrast to Galileo Galilei, Leonardo Da Vinci correctly identifies the stress and strain distribution (in words and not equations) along the deflection of a beam.
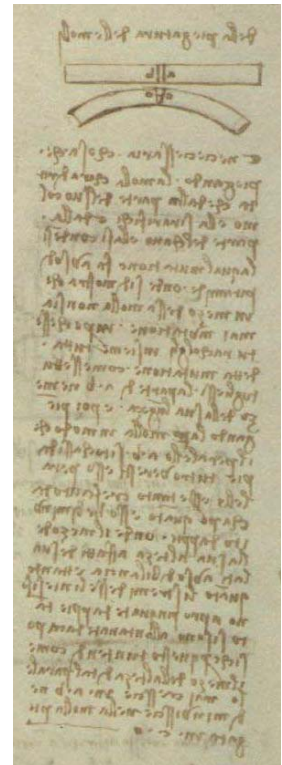
Modal Analysis of an Euler-Bernoulli Beam

Most vibration problems are related to resonance phenomena, where the applied dynamic loads excite one or more modes of vibration. One characteristic of modes is that any forced or free response of a structure can be reduced to a discrete set of modes, where the modal parameters are the modal frequency, the modal damping and the mode shape. The modal parameters determine a dynamic description of the structure, where the modes represent the dynamic properties of a free structure. In the process of modal analysis all modal parameters are determined to formulate mathematical dynamic model, where these parameters can be achieved either through analytical, numerical or experimental techniques.

In Eq. (2.31) damping mechanisms are neglected. The solution of Eq. (2.31) in the frequency domain for symmetric modes is [43]

$$\omega_i = \gamma_i^2 \frac{h}{l^2} \sqrt{\frac{E}{12\rho}}, \tag{2.32}$$

where h is the height, l is the length, E is the Young's modulus and ρ is the mass density of the cantilever. The eigenvalues γ_i are solutions of the transcendental Eq. (2.33)

$$1 + \cos\gamma_i \cosh\gamma_i = 0, \tag{2.33}$$

where i represents the numerical order of the higher symmetric mode shapes pictured in Fig. 2.8.
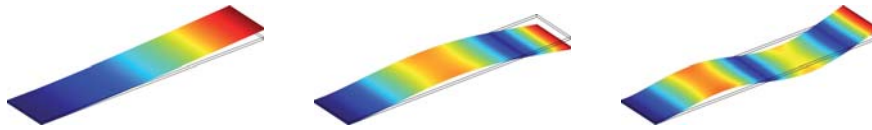
(a) S1 mode with $\gamma_1 = 1.875$ (b) S2 mode with $\gamma_2 = 4.694$ (c) S3 mode with $\gamma_3 = 7.855$

Figure 2.8: Three symmetric mode shapes of an Euler-Bernoulli beam.

The validity of Eq. (2.32) requires that the maximum displacement of the cantilever is much smaller than its length l and that the cross-sectional area A remains constant. These assumptions involve that the width b of an Euler-Bernoulli beam is ditto much smaller than it's length l (approximately two tenth of the length) and that Eq. (2.32) is only valid for uniaxial loads. In the case of a cantilever made up by several layers the neutral axis of each layer does not coincide with all others. Few exceptions allow a homogenization of the cantilever cross section, with one resulting neutral axis.

Another problem arises, in the case of beams with large width. They are more rigid than Eq. (2.32) indicates. This stiffening effect is taken into account by using the flexural rigidity of the plate $E/(1 - \nu^2)$ instead of the Young's modulus E in Eq. (2.32) for wide beams,

$$\omega_i = \gamma_i^2 \frac{d}{l^2} \sqrt{\frac{E}{12\rho(1-\nu^2)}}, \tag{2.34}$$

where ν is the Poisson's ratio [44, 45]. If the deflections of the plate are small compared to its thickness h, the assumption that there is no strain in the middle of the plate will be fulfilled and linearity can be ensured. Otherwise the stress distribution of the plate has to be considered. The solutions for Eq. (2.32) and Eq. (2.34) are in good agreement with FEM-simulations for the natural frequency (S_1).

U-shaped Cantilever

U-shaped cantilevers are more compliant than beams or plates, due to their smaller geometrical moment of inertia. They can be modelled by two slim cantilevers with additional mass at the end of both beams schematically shown in Fig. 2.9.
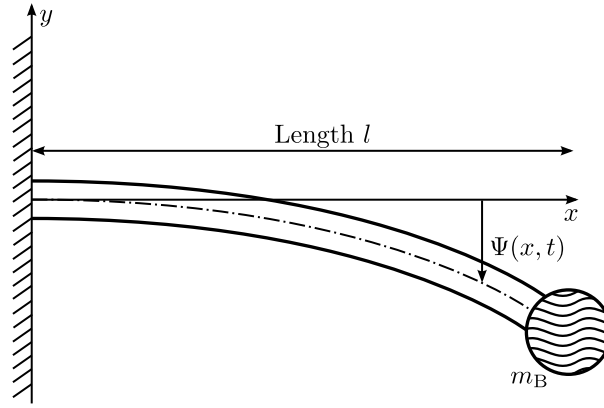
Figure 2.9: In the case of flexural vibrations U-shaped cantilevers can be modeled as simple straight beams with an additional tip mass m_B.

Therefore, the lowest eigenfrequency of a U-shaped cantilever will be much smaller than of a beam or plate with the same enclosed ground area and heigth. In the case of an Euler-Bernoulli Beam, the analysis of Eq. (2.31) in the frequency-domain permits to consider

$$\frac{\partial^4 \Psi}{\partial x^4} + \frac{\rho A}{E J_z} \frac{\partial^2 \Psi}{\partial t^2} = 0 \tag{2.35}$$

which is a simpler differential equation due to the constant coefficients.
Using the separation ansatz for $\Psi(x,t) = \boldsymbol{q}(t)^{\mathrm{T}} \boldsymbol{w}(x)$ and the constraints become $w(0) = w'(0) = 0$, $w''(l) = w'''(l) = 0$ for a single-sided clamped beam with mass m_B at the tip of the cantilever Eq. (2.35) becomes

$$\frac{\partial}{\partial x} \left(E J_z \frac{\partial^2 w}{\partial x^2} \right) \bigg|_l = m_B \left(\frac{\partial^2 w}{\partial t^2} \right) \bigg|_l, \tag{2.36}$$

where a harmonic ansatz (with $q(t)_i \propto e^{j\omega_i t}$) permits an analytical solution of eq. (2.36). With

$$w(x)_i = C_1\cos(\beta x)_i + C_2\sin(\beta x)_i + C_3\cosh(\beta x)_i + C_4\sinh(\beta x)_i\,, \qquad (2.37)$$

where $\beta = \rho A\omega^2/(EJ_z)$, results from the separation ansatz and the constraints it is possible to determine the four unknown $C_{i=1\,to\,4}$ corresponding to the order of the differential Eq. (2.36).
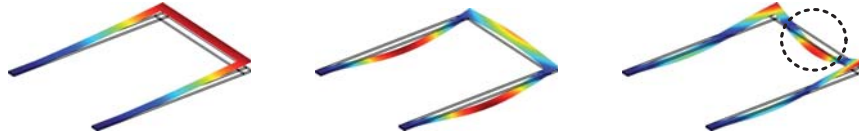
(a) S_1 mode with $\gamma_1 = 1.522$ (b) S_2 mode with $\gamma_2 = 4.147$ (c) S_3 mode with $\gamma_3 = 6.001$

Figure 2.10: Three symmetric mode shapes of a U-shaped cantilever with a length of 2 mm, a height of 20 μm, a width at the attachment of 70 μm (twice).

In a very similar way to the derivation of Eq. (2.33) following equation of eigenvalues

$$1 + \cos\gamma_i\cosh\gamma_i - \gamma_i\left(\frac{m_B}{\rho Al}\right)[\sin\gamma_i\cosh\gamma_i - \cos\gamma_i\sinh\gamma_i] = 0 \qquad (2.38)$$

is a consequence of the ansatz of Eq. (2.37) and the constraints. Evidently, solutions of Eq. (2.38) converges in the case of $m_B = 0$ against the results of Eq. (2.33). If $m_B \neq 0$ the resulting eigenvalues are smaller than for a beam with an additional mass at the tip of the cantilever. After a short auxiliary calculation the equation of eigenvalues for both Euler-Beams and U-shaped cantilevers becomes

$$\frac{1 + \cos\gamma_i\cosh\gamma_i}{\gamma_i\,[\sin\gamma_i\cosh\gamma_i - \cos\gamma_i\sinh\gamma_i]} = \xi\,, \qquad (2.39)$$

where $\left(\frac{m_B}{\rho Al}\right) \equiv \xi$ is the nondimensional tip mass parameter in Fig. 2.11 and $\gamma_i \neq 0$. The intersection points in Fig. 2.11 represents the eigenvalues of an Euler-Beam in the case of $m_B \neq 0$ and for two representative U-shaped cantilevers made of silicon. Usually, the eigenvalues derived by the analytical models in Table 2.1 fit together with those obtained by FEM simulation techniques (modes shapes shown in Fig. 2.10).

For flexural modes higher than S_2 the difference between the analytical solutions and the results of FEM simulation increases. This is a consequence of the influence of the tip of the cantilever, which is analytically modeled as a lumped mass shown in Fig. 2.9. The differences for this mode in Table 2.2 are always greater than 20 % except those for an Euler-Beam because additional deflections of the cross-beam and the two main beams are neglected. For example, the deflections of the bar between both cantilevers in Fig. 2.10 is significant, but totally neglected in the analytical solution for the S_3-mode.
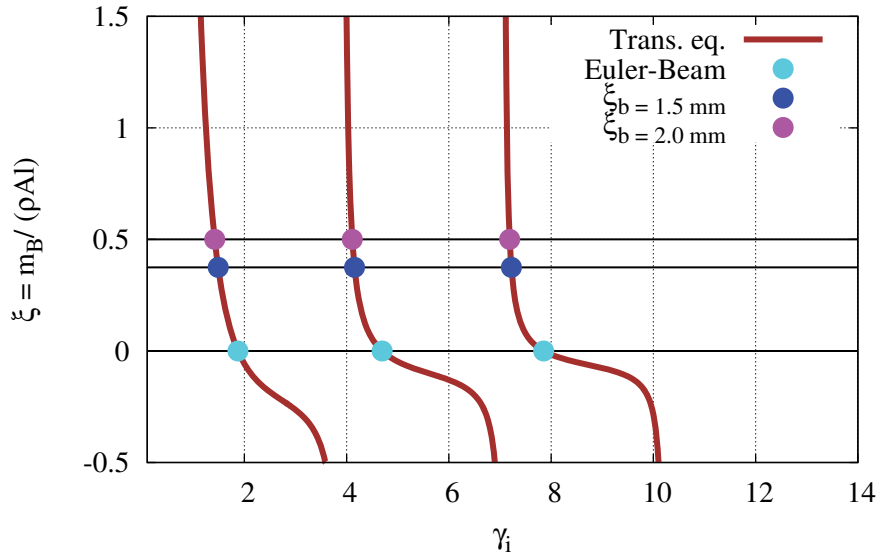
Figure 2.11: Solutions for the first triple of eigenvalues γ_i for an Euler-Beam (1.875; 4.694; 7.855) and two typically U-shaped cantilevers made of silicon with a length of 2 mm, a height of 20 μm, a width at the attachment of 70 μm (twice) and a width at the tip of the beam of 1.5 mm (1.487; 4.155; 7.223) and 2.0 mm (1.420; 4.111; 7.190).

Table 2.1: Typical eigenvalues of an Euler-Beam and two U-shaped cantilevers all with a length of 2 mm, a heigth of 20 μm and made of silicon. The eigenvalues are calculated analytically and are gained by FEM simulations.

γ_i	1st	1^{st}_{FEM}	Deviation	2nd	2^{nd}_{FEM}	Deviation
Euler − Beam	1.875	1.884	0.5 %	4.694	4.724	0.6 %
b = 1.5mm	1.487	1.522	2.3 %	4.155	4.147	1.9 %
b = 2.0mm	1.420	1.447	1.9 %	4.111	3.883	5.9 %

Table 2.2: Characteristic deviations of the S_3-mode.

γ_i	3rd	3^{rd}_{FEM}	Deviation
Euler − Beam	7.855	7.932	0.97 %
b = 1.5mm	7.223	6.001	20.4 %
b = 2.0mm	7.190	5.025	43.1 %

Damped Euler-Bernoulli Beam

If the velocity for the harmonic motion of the beam is written in complex notation $\dot{x} = v = v_0 e^{-i\omega t}$, the drag force $F = D\dot{x}$ becomes also complex and the damping parameter $D = \beta_1 + i\beta_2$ represents a complex constant. A typical structural damping model of a vibrating beam describes the internal damping by

$$F = (\beta_1 + i\beta_2)\, v\,, \tag{2.40}$$

where β_1 and β_2 are real constants. For harmonic motion with the velocity $v = v_0 e^{-i\omega t}$, this results in

$$F = \beta_1 v - i\beta_2 \frac{\dot{v}}{\omega}\,, \tag{2.41}$$

where the first term is proportional to the velocity v and the second term to the acceleration $\dot{v}$ [46]. Due to the proportionality to the velocity this part of the drag is called dissipative term because it leads to energy dissipation. While the acceleration part of Eq. (2.41) denotes the inertial term [47]. Blom et al. presented in 1992 a damped Euler-Bernoulli beam equation,

$$\frac{EJ_0}{l^4} \frac{\partial^4 \Psi}{\partial \xi^4} + f_1 \frac{\partial \Psi}{\partial t} + (\rho A + f_2) \frac{\partial^2 \Psi}{\partial t^2} = 0\,, \tag{2.42}$$

for a homogeneous beam with the normalized parameter $\xi = x/l$, $f_1 = \beta_1/l$ the dissipative drag parameter and $f_2 = \beta_2/(\omega l)$ the inertial drag parameter each per unit length. The damped angular eigenfrequencies of Eq. (2.42) are

$$\omega_i = \left[\gamma_i^4 \frac{EJ_0}{(\rho A + f_2)l^4} - \frac{1}{4} \left(\frac{f_1}{\rho A + f_2} \right)^2 \right]^{\frac{1}{2}}\,, \tag{2.43}$$

where the eigenvalues γ_i are solutions of the mode of resonance [46]. Neglecting damping mechanisms in the limit of $f_1 \to 0$ and $\rho A \gg f_2$, Eq. (2.43) becomes 2.32 the angular eigenfrequency of an undamped Euler-Bernoulli beam.

With the help of the separation ansatz $\Psi(x,t) = q(t)^{\mathrm{T}} w(\xi) = w(\xi) e^{i\omega t}$ and under the assumption of a harmonic motion it is possible to determine the stored vibration energy

$$\begin{aligned} E_i &= E_{kin} \Big|_{max} \\ &= \int_0^1 \frac{1}{2} l\, (\rho A + f_2) \left| \left(\frac{\partial \Psi}{\partial t} \right)^2 \right|_{max} d\xi \\ &= \frac{1}{2} l\, (\rho A + f_2)\, \omega^2 \int_0^1 w^2(\xi) d\xi\,, \end{aligned} \tag{2.44}$$

where $w(\xi)$ represents the mode shape function. The the dissipated energy E_d per oscillation period T

$$E_d = \int_0^T F\dot{\Psi}(\xi, t)dt = \int_0^1 \int_0^T lf_1 \left(\frac{\partial \Psi}{\partial t}\right)^2 dtd\xi, \tag{2.45}$$

is given by the drag F and the velocity $\dot{\Psi}(\xi, t)$, with the period $T = 2\pi/\omega$. Combining Eq. (2.44) and 2.45 with Eq. (2.27) and the assumption of harmonic motion leads to

$$Q = \frac{2\pi E_i}{E_d} = 2\pi \frac{\frac{1}{2}l\left(\rho A + f_2\right)\omega^2 \int_0^1 \boldsymbol{w}^2(\xi)d\xi}{lf_1\omega^2 \int_0^1 \boldsymbol{w}^2(\xi)d\xi \underbrace{\int_0^T \cos^2(\omega t)dt}_{\pi/\omega}}, \tag{2.46}$$

Hence the quality factor of a weakly damped cantilever with $\rho A \gg f_2$ becomes

$$Q_{\text{Cantilever}} = \frac{\rho A \omega_0}{f_1}, \tag{2.47}$$

where ρ is the density of the beam material, A is the cross-sectional area and ω_0 denotes the angular eigenfrequency of the first symmetric mode [47]. It is remarkable that Q is very similar to the quality factor of a 1-DOF system of Eq. (2.15) and can be calculated without knowing the mode shape function $\boldsymbol{w}(\xi)$. Evidently, the quality factor increases if the dissipative drag parameter decreases. To get rid of the fluid damping, the vibrating structure has to operate under vacuum conditions.

Sensitivity of Resonant Sensors

A driven weakly damped harmonic oscillator provides an amplified response due to an excitation source applied with a frequency equal to the resonant frequency of the structure, shown in Eq. (2.22). This enhancement is a result by the efficient energy transfer from the excitation source to the oscillator. Due to the measurement principle, the deflection x of the oscillator is transformed into a capacitance change ΔC. The capacitance change ΔC results from the deflection of the cantilever in respect to the equilibrium position

$$\Delta C = C(\Theta) - C(\Theta = 0), \tag{2.48}$$

where $\Theta = 0$ is the angle of deflection, which is schematically shown in Fig. 2.12.
If the deflections are small compared to the height of the cantilever, the electric field between the electrodes can be assumed homogeneous without distortion and stray fields, where the capacity becomes

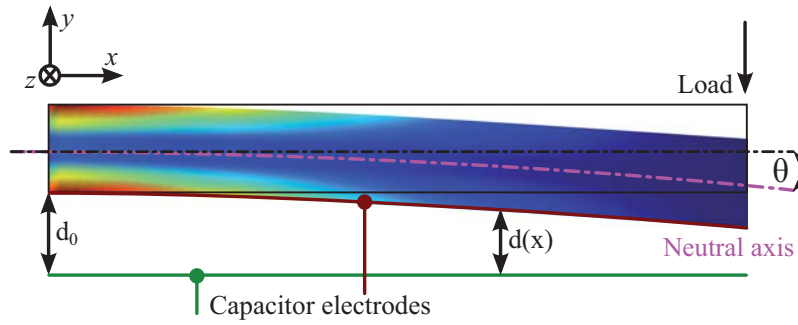$$C(\Theta = 0) = \varepsilon_0 \frac{A_{\text{eff}}}{d_0} \tag{2.49}$$

Figure 2.12: Schematic measurement principle of a capacitance change due to the deflection of a loaded beam.

The effective ground area A_{eff} of the cantilever is a result of the deflection curve of the cantilever. Assuming a harmonic oscillator with $\omega_0^2 = k/m_{\text{eff}}$ and the natural frequeny of Eq. (2.32), the effective mass m_{eff} of the moving cantilever becomes

$$m_{\text{eff}} = \frac{3}{\gamma_1^4} \underbrace{\rho lbh}_{m} = 0.243 \cdot m, \tag{2.50}$$

where $\gamma_1 = 1.875$ and m is the mass of the cantilever with the density ρ. Assuming a cantilever with the same width b and height h, the effective length changes to

$$l_{\text{eff}} = 0.243 \cdot l, \tag{2.51}$$

where the product $b \cdot l_{\text{eff}}$ finally forms the effective area A_{eff}. To determine $C(\Theta \neq 0)$ the infinitesimal part of the capacitor dC along the x-axis with the width ∂x at the position becomes

$$\partial C = \varepsilon_0 \frac{b}{d(x)} \partial x, \tag{2.52}$$

where the shifting distance between the electrodes becomes in a linear approach

$$d(x) = d_0 - x\tan(\Theta). \tag{2.53}$$

With the previous constraints $l \gg b \gg d_0$ and small deflection angles Θ, the capacitor value can be obtained by integrating along the effective length $l_{\text{eff}} = 0.243 \cdot l$

$$C(\Theta) = \varepsilon_0 \int_0^{l_{\text{eff}}} \frac{b}{d_0 - x\tan(\Theta)} dx = -\varepsilon_0 \frac{b}{\tan(\Theta)} \log \frac{d_0 - x\tan(\Theta)}{d_0} \bigg|_0^{l_{\text{eff}}}. \tag{2.54}$$

Combining Eq. (2.49) and 2.54 gives the change in the capacity

$$\Delta C = -\varepsilon_0 \frac{b}{\tan(\Theta)} \log \frac{d_0 - l_{\text{eff}} \tan(\Theta)}{d_0} - \varepsilon_0 \frac{A_{\text{eff}}}{d_0}, \tag{2.55}$$

obviously a nonlinear function due to the deflection angle Θ, shown in Fig. 2.13.
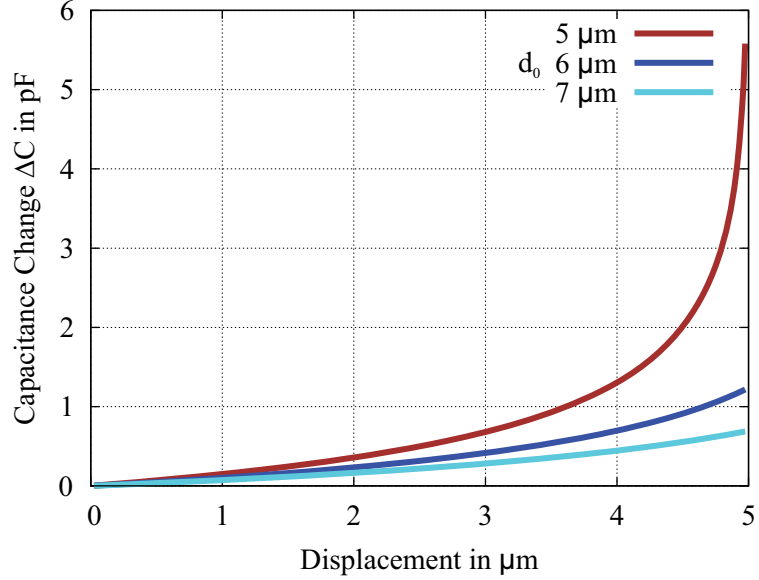
Figure 2.13: Capacity change of the sensing electrode, with typical parameters of the cantilever ($l_{\text{eff}} = 0.243 \cdot 2\,\text{mm}$, $b = 1.5\,\text{mm}$) and different capacitor gaps d_0.

But in the case of small signal analysis, the capacitance change behaves almost linear, which is schematically shown in Fig. 2.14.

The total sensor sensitivity S is a product of several independent sensitivities terms like

$$S = \frac{\partial \tilde{F}}{\partial B} \cdot \frac{\partial \tilde{x}}{\partial \tilde{F}} \cdot \frac{\partial \Delta C}{\partial \tilde{x}},$$

with

$$S = S_{\tilde{F}} \cdot S_{\tilde{x}} \cdot S_{\Delta C}, \tag{2.56}$$

where $\tilde{F}$ is the excitation force due to the external magnetic field B and $\tilde{I}$ the current along the gold lead of the structure. This current induces a voltage drop along the lead, which generates in combination with the sensing electrode a electrostatic force

$$F_{\text{e}} = \frac{1}{2} \frac{\partial C}{\partial x} \tilde{U}^2, \tag{2.57}$$

which is independent from the quantity B. This lowers the sensitivity regarding the magnetic flux density B. In consequence the excitation current has to be minimized to detect a minimum
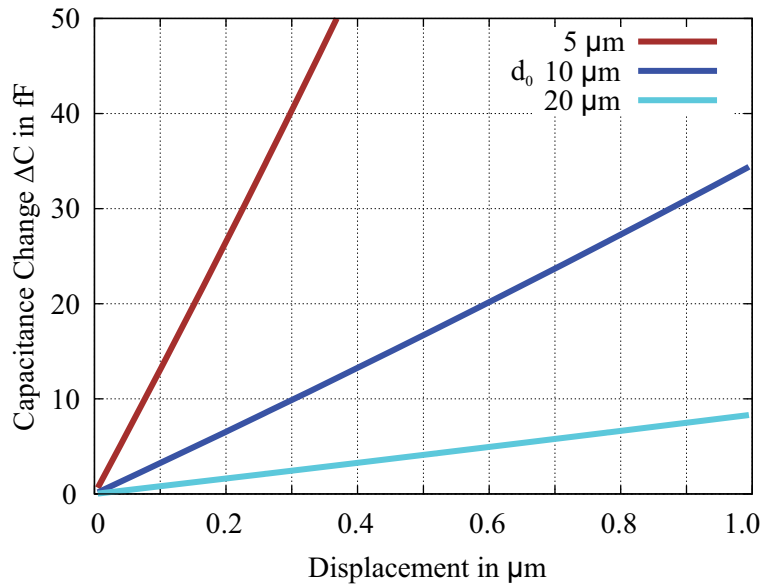
Figure 2.14: Capacity change of the sensing electrode, with typical parameters of the cantilever (l=2 mm, b=1.5 mm) and different capacitor gaps d_0 in the limit of small signal analysis.

of the external magnetic field. However, the Lorentz force $F_\mathrm{L} = \tilde{I}bB$ acting on the lead along the tip, induces a torque M along the elastic axis l, which is dependent on the magnetic field B and the current $\tilde{I}$. The derivative $\partial\tilde{F}/\partial B$ becomes

$$S_{\tilde{F}} = Ib,\tag{2.58}$$

where the sensitivity $S_{\tilde{F}}$ is proportional to the excitation current $\tilde{I}$ and b the width of the cantilever. Furthermore the deflection $\tilde{x}$ of the oscillator in Eq. (2.19) is a result of the applied harmonic force $\tilde{F}$ at the tip of the cantilever

$$S_{\tilde{x}} = \frac{\partial \tilde{x}}{\partial \tilde{F}},\tag{2.59}$$

where the sensititvity of the oscillator due to the deflection becomes at resonance

$$S_{\tilde{x}} = \frac{1}{D\omega_0} = \frac{Q}{k}.\tag{2.60}$$

From this result it is obvious that the sensitivity of the oscillator is most affected by the quality factor Q. But the reasons of the quality factor Q are versatile. Consequently, this topic will be discussed in a further chapter in more detail.

Perturbation Analysis

The typically electrostatic excitation of micromechanical resonators with a capacitive gap is realized with an ac source u_s along with polarization DC bias U_p.

$$F_e = \frac{1}{2}\frac{\partial C}{\partial x}\left(U_p + u_s\right)^2 . \tag{2.61}$$

This section will present how the mechanical resonator is modeled with electrical circuit components, where the electro-magneto-mechanical system is modeled as a suspended mass-spring resonator in Fig. 2.15, and described by an ordinary second-order differential equation

$$m\ddot{x} + D\dot{x} + kx = F(x, \dot{x}, t), \tag{2.62}$$

where m is the mass of the movable structure in kg, D the damping coefficient in Ns/m, k the stiffness in N/m and F the applied external force in N.
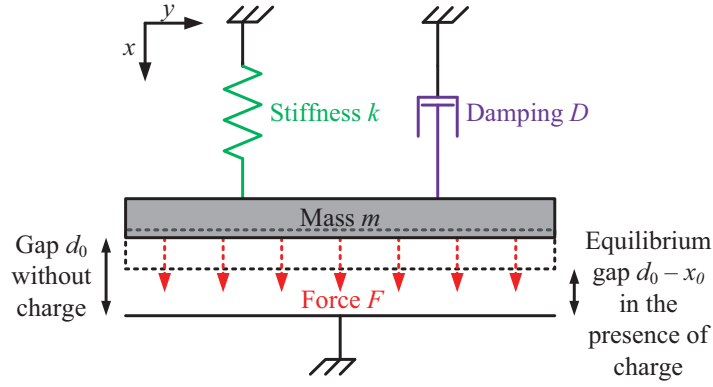
Figure 2.15: Schematic mechanical model of the time-varying MEMS capacitor.

Without the capacitive read-out system, the structure would only be deflected or harmonically excited by the Lorentz force F_L, where Eq. (2.62) describes a harmonic oscillator

$$\ddot{x} + \omega_0^2 x = f, \tag{2.63}$$

where $\omega_0^2 = k/m$ and $f = (F - D\dot{x})/m$. If the nonlinearities of damping D and the driving force F are negligible, the solution of Eq. (2.63) has the sinusoidal form $x(t) = a\cdot\sin(\omega_0 t + \varphi)$, where a is the amplitude and φ is the phase of the oscillation. In the case of small nonlinearities compared to the left side of Eq. (2.63), the stationary solution will almost be the same of a harmonic oscillator, but the oscillator will move with the exciting frequency.

Energy considerations allow a more fundamental aspect of the nonlinear origin of electro-magneto-mechanical system [48]. The potential energy of the resonator is given by

$$E_{pot} = \frac{1}{2}k_m x^2 + \frac{1}{2}\frac{\varepsilon A}{(d-x)}\left(U_p + u_s\right)^2 + mgd, \tag{2.64}$$

where k_{m} is the mechanical stiffness, ε the permittivity, A is the area of the parallel-plate capacitor, $d = d_0 - x_0$ is the electrode gap at rest, x is the vibration displament of the resonator, $U_{\mathrm{p}} + u_{\mathrm{s}}$ is the voltage across the variable capacity and due to gravity, the potential energy mgd of the oscillator. The current through the lead of the cantilever is driven by an ac voltage u_{ac} which combines with the polarization voltage U_{p}. The ac voltage developed at the sense electrode u_{s} is generated by the vibration of the cantilever and is dependent on the drop of the drive voltage u_{ac}. In the presence of charge on the resonator or on the sense electrode, a new equilibrium position $d_0 - x_0$ in Fig. 2.15 will be reached. In the case of perturbation analysis $x \ll d$ and $u_{\mathrm{s}} \ll U_{\mathrm{p}}$, the potential energy $E_{\mathrm{pot}}(x)$ along with the electrostatic force $F_{\mathrm{e}} = \frac{1}{2} \frac{\varepsilon A}{(d_0 - x_0 - x)^2} U_{\mathrm{p}}^2$ acting on the resonator can be expanded in a power series

$$F_{\mathrm{e}}(x) = \frac{1}{2} \frac{\varepsilon A}{(d_0 - x_0)^2} U_{\mathrm{p}}^2 + \frac{1}{2} \frac{\varepsilon A}{(d_0 - x_0)^3} U_{\mathrm{p}}^2 \cdot x \qquad (2.65)$$
$$+ \frac{3}{2} \frac{\varepsilon A}{(d_0 - x_0)^4} U_{\mathrm{p}}^2 \cdot x^2 + 2 \frac{\varepsilon A}{(d_0 - x_0)^5} U_{\mathrm{p}}^2 \cdot x^3 + \mathcal{O}(x^4),$$

where the coefficient of the linear term is equivalent to the electrostatic stiffness k_{e}. Clearly arranged the homogeneous differential equation has the form

$$m\ddot{x} + D\dot{x} + \left(k_{\mathrm{m}} - \frac{\varepsilon A}{(d_0 - x_0)^3} U_{\mathrm{p}}^2 \right) x + \underbrace{\beta x^2 + \alpha x^3 + \mathcal{O}(x^4)}_{h(x(t))} = 0, \qquad (2.66)$$

where $h(x(t))$ in Eq. (2.66) represents a nonlinear function, vanishing if $x \to 0$. Lifshitz and Cross showed in 2010 that the terms $\beta x^2 + O(x^4)$ can be replaced by $\eta x^2 \dot{x}$, the nonlinear damping term [48]. In small signal analysis, the linear term of Eq. (2.66) becomes

$$k = k_{\mathrm{m}} - \underbrace{\frac{\varepsilon A}{(d_0 - x_0)^3} U_{\mathrm{p}}^2}_{k_{\mathrm{e}}}, \qquad (2.67)$$

where the stiffness of the system becomes most affected on the polarization voltage U_{p}, which has to be considered in the calculation of the sensitivity (see Eq. (2.60)). In general, this cubic equation leads to the well-known snap-in or pull-in effect published by Seeger et al. in 1995 [49]. Because of the nonlinear relationship between the polarization voltage U_{p} and the gap between the sens electrodes, a characteristic equilibrium distance always leads to mechanic instabilities. This statement is consistent with the Earnshaw's theorem. The theorem reveals that any configuration of point charges cannot be retained in a stable stationary equilibrium only by the electrostatic interaction of the charges, which is a result of Gauss's law ("The divergence of any possible electric force field is zero in free space"). In the equilibrium of forces, with a new equilibrium position $d_0 - x_0$, the mechanical restoring force

$$k_\mathrm{m} x_0 = \frac{1}{2} \frac{\varepsilon A}{(d_0 - x_0)^2} U_\mathrm{p}^2$$

where

$$x_0 \cdot (d_0 - x_0)^2 = \underbrace{\frac{\varepsilon A}{2 k_\mathrm{m}} U_\mathrm{p}^2}_{y(x_0)}, \tag{2.68}$$
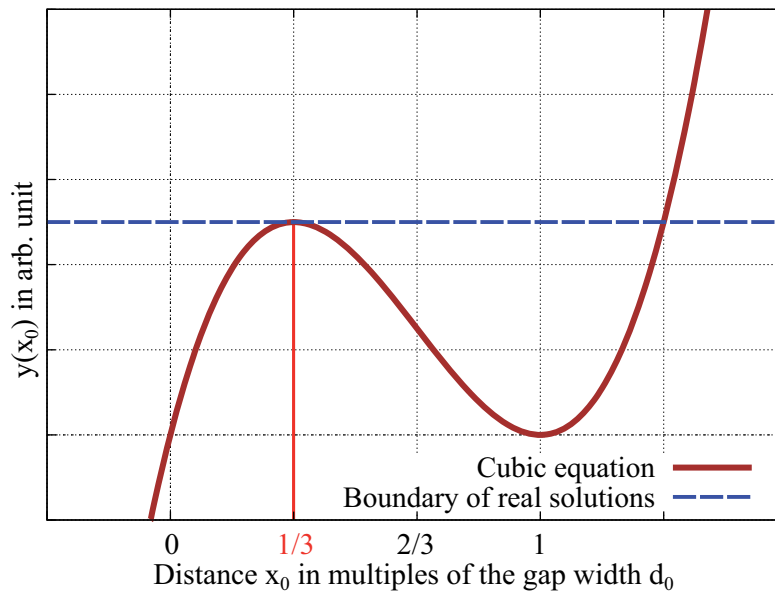

Figure 2.16: Cubic equation to calculate the limit of the snap-in.

is equal to the electrostatic force, which leads to a cubic equation to determine the limit of the possible stable equilibrium displacement (see Fig. 2.16). The solution of Eq. (2.68) becomes $x_0 = d_0/3$. It is worth mentioning that this displacement is independent of the voltage and the stiffness and therefore snap-in isn't preventible in the stationary case until the limit is achieved. Due to Eq. (2.67) it is obvious that unlike linear systems, nonlinear systems may vibrate in a frequency other than their natural frequencies when they are perturbed from their equilibrium position.

Because of Eq. (2.19) it is obvious that the third significant sensitivity, $\partial \Delta C / \partial \tilde{x}$ will become nonlinear in the case of large deflections, e.g. due to huge external magnetic fields. In small signal analysis it is reasonable to use the much simpler suspended mass-spring resonator. Then the sensitivity of ΔC regarding the deflection x of the parallel-plate capacitor, becomes
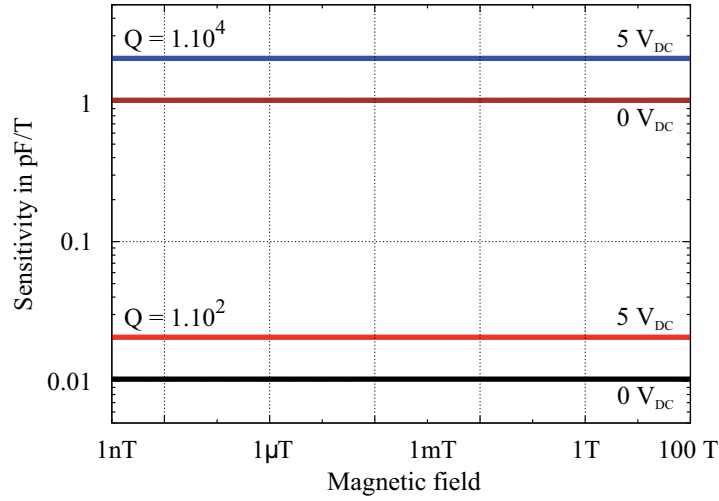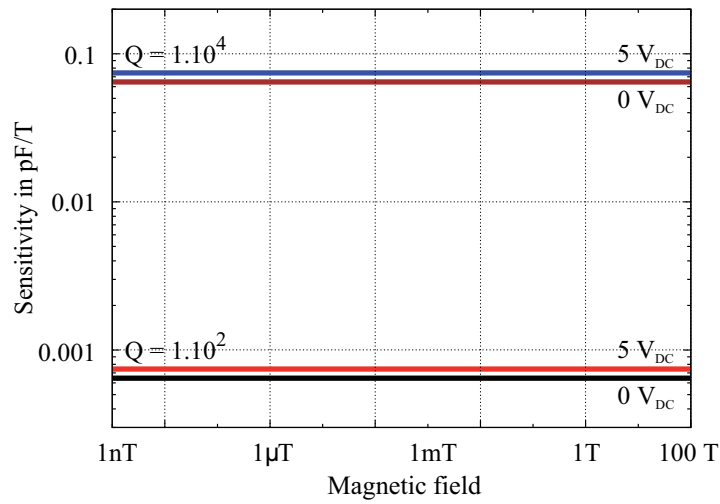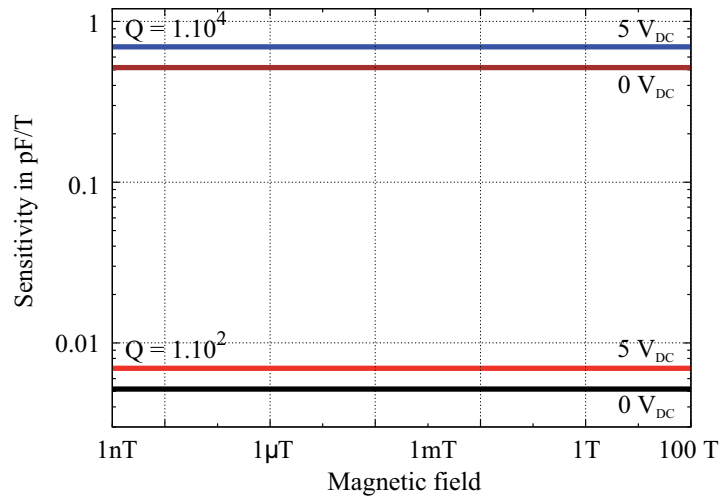
Figure 2.17: Sensitivity as a function of the external magnetic field, with typical parameters of the cantilever (l=2 mm, b=1.5 mm, h=20 µm, d=5 µm) and two different polarization voltages U_p in the limit of small signal analysis.

$$S_{\Delta C} = \frac{\partial \Delta C}{\partial x} = \varepsilon_0 \frac{A_{\mathrm{eff}}}{(d-x)^2} = \varepsilon_0 \frac{A_{\mathrm{eff}}}{(d_0 - x_0 - x)^2}$$

with

$$\Delta C = C(x) - C(x=0) = \varepsilon_0 A \left(\frac{1}{d-x} - \frac{1}{d} \right), \tag{2.69}$$

considering the influence of the polarization voltage U_p on the new equilibrium distance $d - x_0$. Combining Eq. (2.58), 2.60 and 2.69 the total sensitivity due to Eq. (2.56), becomes for an electrode gap with 5 µm and a quality factor of $1 \cdot 10^4$ about 1 pF/T (Fig. 2.17). By comparison of Fig. 2.17 and 2.18 the total sensitivity decreases, with an increasing electrode gap.

In the case of a decreasing stiffness, e.g. with a smaller width of the beam, the electrode area will decrease too, and therefore the sensitivity will not benefit. But if the height of the cantilever gets smaller, the stiffness will decrease and the sensitivity will increase, which is shown in Fig. 2.19.

Figure 2.18: Sensitivity as a function of the external magnetic field, with typical parameters of the cantilever (l=2 mm, b=1.5 mm, h=20 µm), two different polarization voltages U_p and a electrode gap of 20 µm.

Figure 2.19: Sensitivity as a function of the external magnetic field, with typical parameters of the cantilever (l=2 mm, b=1.5 mm, h=10 µm), two different polarization voltages U_p, a electrode gap of 20 µm, but half the height of Fig. 2.18.

General Dynamics, Stability, Nonlinearities and Chaos

Microcantilevers, especially in MEMS-applications possess several distinct eigenmodes and the tip-sample interaction forces are under certain circumstances highly nonlinear. Therefore, cantilevers can vibrate in interesting, often unanticipated ways. Some of these states are detrimental for the mechanical stability, while others may exploite the enhancement of M/NEMS performance. A deeper insight of these phenomena can offer further improvements MEMS applications. Resonance of micromechanical components can result in vibration amplitudes that are not negligible compared to characteristic lengths of the device. For large amplitudes the governing equation of motion of the resonator becomes a non-linear character, which results in nonlinear oscillations. A small signal analysis of the sensor provides only a limited insight into the performance of the sensor. This chapter deals with the large signal behavior of the resonator. Nonlinear dynamic behavior of the resonator can influence the quality of the measurement signal substantially. The reasons of nonlinear behavior can be manifold, but the most important causes are [50]:

Material nonlinearities are masked in the stress-strain relationships of the applied materials. This relationships include non-linear elasticity, plasticity and viscoelastic behavior (see Chapter 2.3) plus nonlinearities of the $B - H$ relation regarding electromagnetic actuation.

Geometric nonlinearities are dependencies of the deflection due changes in the stiffness of the specimen, without violation against Hooke's law. Some examples are the stress-stiffening effect as well as a mechanical bumper and a bearing clearance. In an analogy, stationary, but not isotropic electrostatic and magnetic forces can lead to similar effects.

Kinematic nonlinearities, where the motions of the moving components of the system have a nonlinear relationship, e.g. connections between a piston and crank.

Inertia nonlinearities, where the kinetic energy of the system is the source, e.g. centripetal and Coriolis acceleration terms. The nonlinear terms usually comprise velocities and/or accelerations in the equations of motion.

Nonlinear fluid damping, which is mainly determined by squeezing of the surrounding fluid around the moving body. The effect is not only determined by the place, but also through the velocity of the solid.

Nonlinear systems neither satisfy the principle of superposition nor of proportionality. If the trigger function is a composition of several subfunctions, like different spectral components, the system response can not be superimposed by calculating all individual responses. Neither leads a scaling of the trigger amplitude an equivalent scale of the response amplitude. According to the consequences of nonlinear terms in the equation of motion one has to distinguish between weakly and strongly nonlinear effects on the oscillating system [51]. For weakly nonlinear systems, no qualitative changes occur regarding the system response compared to the linear system. The differences are simply of quantitative nature, e.g. the dependence of the amplitude of the resonance frequency. Strong nonlinear effects usually include following phenomena:

- Hysteresis behavior and jumps in the amplitude of the system response

- Different eigenfrequencies with an integer ratio and resonances far away from the excitation frequency (sub-harmonic resonance, super-harmonic resonance, and super-sub-harmonic resonance)

- Quasi-periodic, non-periodic and stochastic vibrations, despite periodic excitation

- Stationary self-oscillations and linear parametrically oscillations with finite amplitudes

For frequency-selective and frequency-analog micromechanical sensors these effects will deteriorate the performance of the sensor. The following sections will deal with the question whether the limits of the weakly nonlinear case are exceeded, and if the achievable sensor characteristics in the weakly nonlinear case can be quantified.

Outgoing from an electromagnetic actuation with a capacitive sensing, Eq. (2.66)

$$m\ddot{x} + D\dot{x} + \left(k_{\mathrm{m}} - \frac{\varepsilon A}{(d_0 - x_0)^3} \left(U_{\mathrm{p}} + u_{\mathrm{s}} \right)^2 \right) x + \underbrace{\beta x^2 + \alpha x^3 + \mathcal{O}(x^4)}_{h(x(t))} = 0$$

$$m\ddot{x} + \left(D + \eta x^2 \right) \dot{x} + \left(k_{\mathrm{m}} - \frac{\varepsilon A}{(d_0 - x_0)^3} \left(U_{\mathrm{p}} + u_{\mathrm{s}} \right)^2 \right) x + \alpha x^3 = 0\,, \qquad (2.70)$$

permits a quantification of weak and strong nonlinear effects, where the reason of nonlinearities is the electrostatic force. One can easily determine different nonlinear regimes, even though Eq. (2.66) is a result of small signal analysis ($x \ll d$).

If the nonlinear function $h(x(t))$ in Eq. (2.66) is negligible, Eq. (2.70) becomes

$$m\ddot{x} + D\dot{x} + \left(k_{\mathrm{m}} - \frac{\varepsilon A}{(d_0 - x_0)^3} \underbrace{\left(U_{\mathrm{p}} + u_{\mathrm{s}} \right)^2}_{U_{\mathrm{p}}^2 + 2U_{\mathrm{p}}u_{\mathrm{s}} + u_{\mathrm{s}}^2} \right) x = 0\,, \qquad (2.71)$$

where the coefficient of the linear term contains a time-dependent expression u_{s} [52]. In contrast to the case of external excitations, in which a small excitation cannot produce a large response unless the frequency of the excitation is close to one of the natural frequencies of the system, this kind of (parametric) excitation can produce a large response, even if the frequency of excitation is far away from the primary resonance. In the case of a harmonic parametric excitation, the stiffness of the system becomes time-dependent with a characteristic 2ω dependence, through the expanded term u_{s}^2. Hence, a small parametric excitation can produce a large response if the frequency of the excitation is close to twice of one of the natural frequencies of the system [50]. Other possibilites for parametric excitation of a forced oscillating system are e.g. modulating the moment of inertia or the length of a pendulum or a periodic shift of the center of mass, like a child on a swing in Fig. 2.20 or a pendulum with a moving support.

Beside the simple but instructive approach to parametric excitation with the children's swing, many M/NEMS devices tend to parametric resonance, as described in literature [53–57]. In the past century nonlinear behaviour in mechanical and electrical devices has been extensively studied. Since the fundamental publication of Turner et al. in 1998, several applications of M/NEMS devices like very-high frequency resonators, devices with respect to motion and mass detection or up-converter amplifiers have been published, where nonlinear behavior plays an important role [53, 58–64].

Figure 2.20: The children's swing as the simplest example of parametric resonance.

Additionally to the experimental investigations various profound theoretical publications regarding nonlinear oscillators have to be mentioned, like the publications of Nayfeh & Mook or the contributions of Lifshitz & Cross and DeMartini et al., and not least the very comprehensive overview over the past decade by Rhoads et al. [48, 50, 65, 66].

Mathieu Equation

M. Faraday described in 1831 parametric resonance behavior, where he noticed that surface waves in a fluid-filled cylinder exhibits a frequency under vertical excitation that is twice the period of the excitation itself [67]. But it was E. Mathieu in 1868, where he described the dynamic behavior of elliptical vibrations through membranes using differential equations [68]. In the case of an undamped system, without a polarization voltage ($U_{\mathrm{p}} = 0$), Eq. (2.71) becomes

$$m\ddot{x} + \left(k_{\mathrm{m}} - \frac{\varepsilon A}{(d_0 - x_0)^3} u_{\mathrm{s}}^2 \right) x = 0 \,. \tag{2.72}$$

With a harmonic component $u_{\mathrm{s}} = \hat{u}_{\mathrm{s}}\sqrt{2}\cos\omega t$, Eq. (2.72) contains a characteristic 2ω dependence. With the help of Eq. (2.67), where in contrast the electrical stiffness is determined by the amplitude $\hat{u}_{\mathrm{s}}^2$ and the normalization of $\omega t = \tau$ and $x/d = z$, Eq. (2.72) becomes

$$\ddot{z} + \left[\underbrace{\frac{\Omega_{\mathrm{m}}^2 + \Omega_{\mathrm{e}}^2}{\omega^2}}_{a} - \underbrace{\left(\frac{\Omega_{\mathrm{e}}}{\omega} \right)^2}_{2q} \cos(2\tau) \right] \cdot z = 0 \,, \tag{2.73}$$

where $\Omega_{\mathrm{m}}^2 = k_{\mathrm{m}}/m$ and $\Omega_{\mathrm{e}}^2 = k_{\mathrm{e}}/m$. The standard presentation of a parametric forced system is

$$\ddot{z} + [a - 2q\cos(2\tau)] \cdot z = 0 \,, \tag{2.74}$$

the Mathieu equation, where a and q are the parameters of the differential equation and τ represents the normalized time. It is a linear, second order, homogeneous ordinary differential equation with real periodic coefficients. The stability behavior of the Mathieu equation was analyzed in detail by van der Pol and Strutt [69]. Only the homogeneous part of the differential equation is responsible for the stability of the solutions of the Mathieu equation, even under complex physical conditions. Stable solutions can be presented by periodic functions with the period of π, which are explicit dependend on the parameters a and q. It is a characteristic of the Mathieu equation with periodic coefficients that stable or unstable frequency bands alternate with each other (see Fig. 2.21).
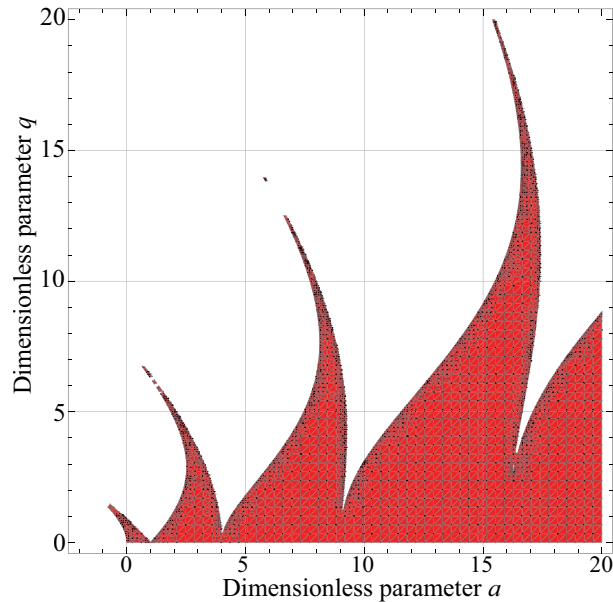
Figure 2.21: Stability chart of the Mathieu Eq. (2.74). The stable (red) and unstable (white) regions alternate with each other. On the transition (in stability) curves, there are periodic solutions of the Mathieu equation.

Choosing the values of the parameters a and q arbitrarily, there are three possibilities of evolution:

- Both the linearly independent solutions are periodic with frequencies incommensurate with each other. Then the general solution is quasiperiodic and the $a - q$ point belongs to the stable region in the $a - q$ parameter plane.

- One linearly independent solutions grow and therefore the other decays exponentially in time. The solution in general is unstable and the $a - q$ point belongs to the unstable region.

- One solution is periodic (with period either 2π or 4π) and the other is linearly growing in time. The corresponding $a - q$ point lies on the stability boundary.

Parametric resonance occurs, due to Eq. (2.74) when the parameter changes twice during one period, once during one period, twice during three periods, and so on, but the maximum energy transfer to the vibrating system occurs when the parameter is changed twice during one period of the natural frequency [70]. Another difference between parametric excitation and forced vibration is the dependence of the growth of energy regarding the energy already stored in the system. The increment of energy during one period in a forced system is proportional to the amplitude of vibrations, which corresponds to the square root of the energy. Meanwhile the increment of energy at parametric resonance is proportional to the energy stored in the system.

In the presence of a polarization voltage U_p the situation becomes even worse. As long as $u_\mathrm{s} \ll U_\mathrm{p}$ and u_s is harmonically, Eq. (2.70) is a kind of Hill equation[1], with an additionally time-dependent term. But with increasing excitation voltages, the amplitude of the resonator will further increase, where the cubic term αx^3 of Eq. (2.70) will play an important role. This term is the so-called Duffing term, with the characteristic Duffing-parameter α.

Duffing Equation

Even neglecting the nonlinear characteristics of the modulated spring constants ($k = k_\mathrm{m} - k_\mathrm{m}$) on the dynamic behavior of the resonator, leads to nonlinearities due to the cubic term of Eq. (2.70). With increasing exciting voltages and without damping, Eq. (2.70) becomes

$$m\ddot{x} + \underbrace{\left(k_\mathrm{m} - \frac{\varepsilon A}{(d_0 - x_0)^3}\left(U_\mathrm{p} + u_\mathrm{s} \right)^2 \right)}_{k} x + \alpha x^3 = 0$$

$$m\ddot{x} + kx + \alpha x^3 = 0 , \tag{2.75}$$

the so-called Duffing equation, where k and α can suppose both positive and negative values. Generally, in a nondimensional representation, Eq. (2.75) becomes

$$\ddot{z} + \frac{k}{m\omega^2}z + \frac{d^2\alpha}{m\omega^2}z^3 = 0 , \tag{2.76}$$

where $z = x/d$ and $\tau = \omega t$, the nondimensional time. If the natural frequency of the oscillating system, should represent the frequency unit, $k/(m\omega^2) \equiv 1$ and $d^2\alpha/(m\omega^2) \equiv \epsilon$. The parameter ϵ respresents the degree of non-linearity of the differential equation

$$\ddot{z} + z + \epsilon z^3 = 0 . \tag{2.77}$$

---

[1]The Mathieu equation is a special case of the Hill's equation.

In the limit of $\epsilon \to 0$, the normalized Duffing equation merge into the differential equation of an undamped suspended mass-spring resonator. In the case of small non-linearities ϵ, the solution can be obtained by a power series method. For large time scales ($\epsilon\tau > \mathcal{O}(1)$) this approach lose his validity, as explained by Nayfeh and Mook in 1979 because of compounds of algebraic and trigonometric terms [50]. To avoid mixed terms, Nayfeh and Mook introduce different techniques, like the Lindstedt-Poincare technique, the method of multiple scales, the variation of the parameters and the method of averaging. Starting from Eq. (2.67), the frequency of vibration always decreases in the presence of exciting voltages (softening effect). The effect of cubic nonlinearity on the other hand depends on its sign; for $\epsilon > 0$ the frequency of vibration increases (hardening effect) and for $\epsilon < 0$ it decreases (softening effect), which leads to one characteristic of the Duffing equation, the hysteresis effect.
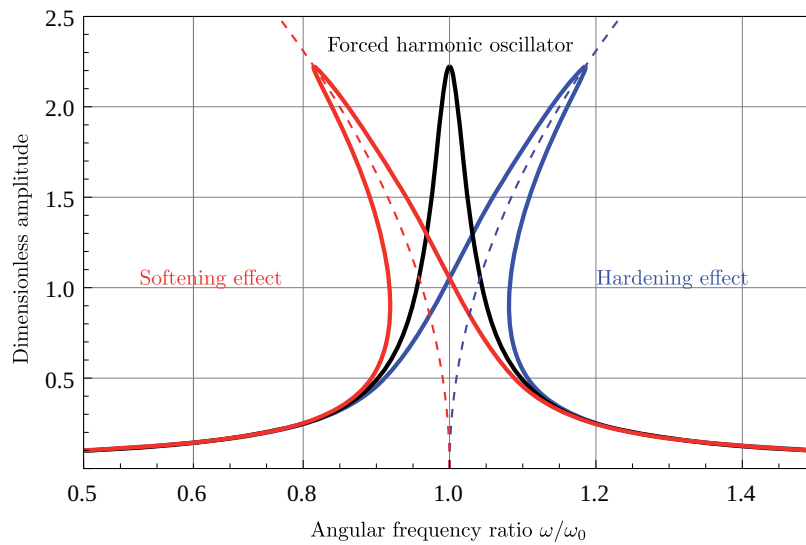
Figure 2.22: Frequency-response curve for the (slightly damped, but forced) Duffing equation for a linear spring (black, $\epsilon = 0$), a hardening spring (blue, $\epsilon > 0$) and a softening spring (red, $\epsilon < 0$).

The ambiguity of the amplitude, due to a unique excitation frequency in the frequency–response curve leads to the phenomena of hysteresis and jumps, illustrated in Fig. 2.23.

In a stability analysis of the solutions, it turns out that the solution on the lower branch (dashed line in Fig. 2.24) of the peak is always unstable. Hence, the system can settle on two different stable amplitudes at one unique excitation frequency. This depends on factors, like the initial conditions of the system, which can be demonstrated in a frequency-sweep test. Exemplarily this jump and hysteresis phenomena will be shown in Fig. 2.23(b). Sweeping ω from small values to the maximum amplitude $a_{\max}$ leads to a jump in the response to a lower value ($\overline{AB}$), where a further sweep of ω leads to a further decrease of the amplitude. Sweeping ω back from large values leads to a jump to a higher amplitude ($\overline{CD}$), but smaller than $a_{\max}$.

Similar phenomena occur in the case of Fig. 2.23(a). These jumps and hysteresis phenom-

(a) Negative cubic nonlinearity.

(b) Positive cubic nonlinearity.
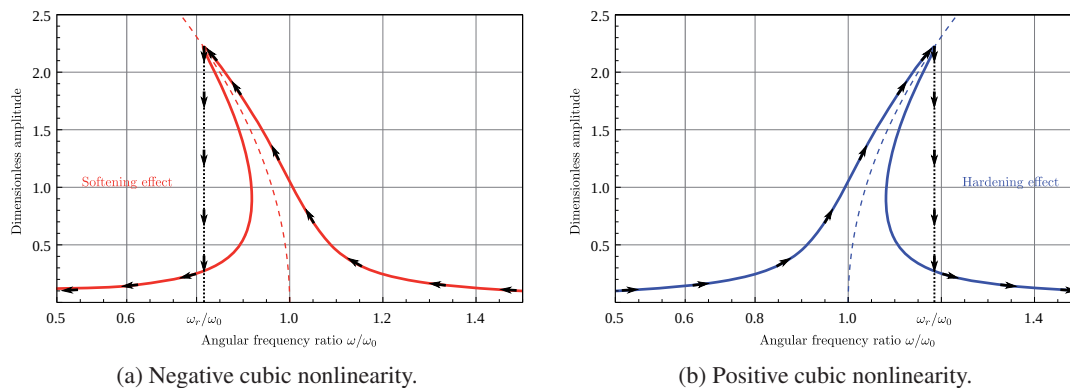
Figure 2.23: Frequency–response curves of the harmonic forced Duffing equation near primary resonance.
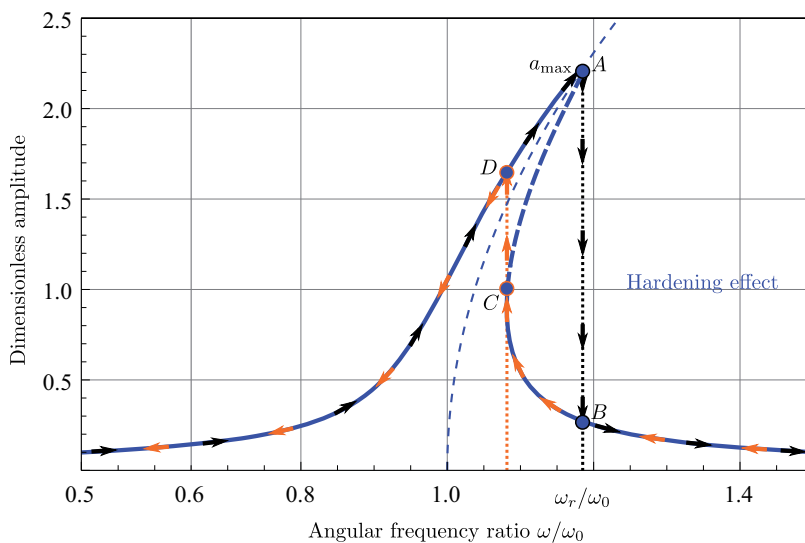
Figure 2.24: Nonlinear response and hysteresis effect for the Duffing equation, with small non-linearity ϵ. The vertical dotted lines depict the transitions as the frequency is swept with a constant exciting force.

ena lead to serious consequences on the stability and reliability of oscillators and resonators. Furthermore occur these jumps at bifurcation points, where the dynamic behavior can result for growing amplitudes in chaotic oscillations of the resonator. That chaotic motions can occur in a single degree of freedom system (1-DOF) possessing one unstable equilibrium and two stable equilibra. This is result of a twin-well energy potential, due to the interaction of the quadratic potential of the spring with the quadratic potential of the cubic nonlinearity in force [71].
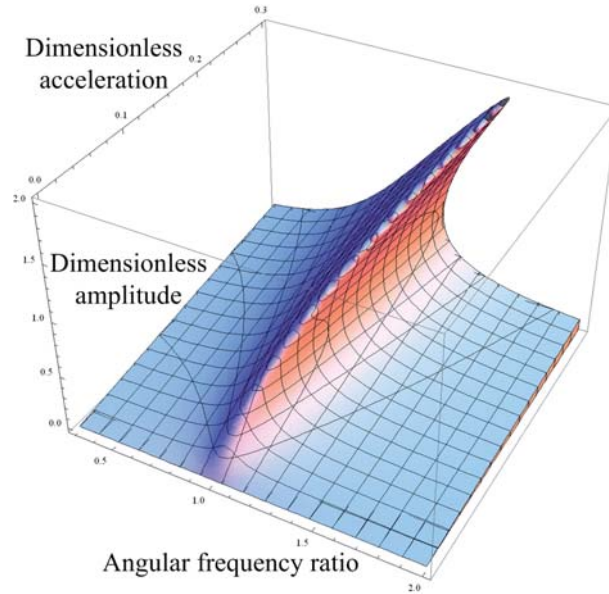
Figure 2.25: Frequency-response curve as a function of the nondimensional exciting frequency and the maximum nondimensional acceleration, where at large vibration amplitudes the response shows hysteresis.

With the method of multiple scales (a perturbation technique), and assuming weak nonlinearity ϵ and forcing, the angular resonance frequency ω_r can be approximated as

$$\omega_r = \omega_0 + \frac{3\epsilon}{8\omega_0}a_{\max}^2, \tag{2.78}$$

where $a_{\max}$ is the maximum amplitude response at ω_r. This amplitude is obviously dependent on the forcing of the system [50]. Equation (2.78) indicates that the maximum amplitude response does not occur near the natural frequency ω_0, but rather near the angular resonance frequency ω_r, which is called the nonlinear angular resonance frequency. This proposition is in contrast to the properties of the Mathieu-equation, where stability problems of a linear system is in the center of interest. The eigenfrequencies of the Duffing-equation depend on the amplitude of the vibration. This frequency–amplitude interaction is a characteristic of nonlinear systems like Eq. (2.76).
Generally, the (normalized) governing equation describing a 1-DOF system with capacitive driving force or sensing becomes

$$\ddot{z} + [a - 2q\cos(\tau)] \cdot z + \epsilon z^3 = 0 = 0 \,, \tag{2.79}$$

where in the case of external excitation, the nonlinearity of the system surpass the response in the instability tongue and makes it finite instead of infinite [72]. Nevertheless, the instability tongue itself is not affected by the presence of the cubic nonlinearity.

Other characteristics of nonlinearities are the generation of higher harmonics of the fundamental oscillation (harmonic distortion). In the case of music instruments these higher harmonics are the "overtones" of the specific instrument. Furthermore, nonlinearities can cause forced oscillations at submultiples of the driving frequency and finally, nonlinearities can excite chaotic oscillations.

Another nonlinearities than the Duffing term, can arise from nonlinear damping behavior $\eta x^2 \dot{x}$, where η represents the coefficient of nonlinear damping, a kind of damping that increases with the amplitude of oscillation [48]. In an actual paper, the nature of nonlinear damping was analyzed in nanotubes and graphene sheets [73]. To differentiate non-linear damping from other reasons, it was assumed that the excitation voltage is always smaller than the unit of voltages $k_B T/e$, where k_B is the Boltzmann constant, T is the temperature und e is the electron charge, in order to prevent electronic nonlinear effects or local heating [38].

In summary one can say that the maximum linear vibration amplitude is limited by nonlinearity and the nonlinear effects. These effects represent the upper limit to the resonator dynamic range, where the lower limit is set by stability or noise.

2.3 Damping Mechanisms

Damping is often a superposition of various mechanisms, where the isolation of the specific mechansim is important for classification and determination of the damping amount under certain conditions. Such damping mechanisms can have mechanical, electrical, optical or even gravitational reasons. The two last mentioned reasons are in this work negligible. For example electrical mechanisms can be classified into electromotive and electrostatic damping mechanisms, just as mechanical mechanisms into intrinsic and extrinsic damping mechanisms [74]. A detailed description of all relevant mechanisms is represented in this chapter.

Mechanical Damping

The basic principal of mechanical damping is an irreversible energy conversion process from kinetic into heat energy. If somebody rub one's hands when shivering under cold he generates heat to warm up. This is a simple example of the thermodynamical result of friction. Generally damping in structural systems is more complex, occurring in different characteristics. Commonly in literature it is categorized into intrinsic and extrinsic damping mechanisms. Usually the damping effects are distributed over the whole volume or surface of the structure, but in case of point forces or moments the damping mechanisms are strongly localized.

Intrinsic Damping

The cause of intrinsic damping is the material itself. If materials are subjected to stress σ they undergo strain ε. Plotting stress against strain for different materials can lead to different graphs. In the simplest case the material behaves linear elastic, stress and strain are related by Hooke's Law

$$\frac{\sigma\,(\text{stress})}{\varepsilon\,(\text{strain})} = \text{constant}\,, \tag{2.80}$$

where the constant is known as elastic modulus (see Eq. (2.80)). For normal stresses the constant is known as Young's modulus E. The validity of the Hooke's Law has two constraints: Firstly, predefined stress must have a strain equilibrium condition which is independent of previous loads. No lasting deformation may appear. Secondly the Young's modulus has to be time-independent. That means that the balanced state has to adjust instantaneous, when a predefined stress to the material specimen is applied. Because of the finite sound of velocity, there occurs always a temporal delay to the state of equilibrium, where a phase shift between stress and strain arises. As a result, a hysteresis loop in the stress-strain plot like Fig. 2.26 appears.

The enclosed area of the hysteresis loop is equivalent to the dissipated energy per unit volume of the material and per stress cycle. Therefore, the hysteresis loop is consequently equivalent to the cyclic motions like vibrations [75]. Possible reasons of intrinsic damping mechansims can be microstructural defects, crystal grain boundaries, dislocations in metals or doped crystals, chain motion in polymers and eddy currents in ferromagnetic media [36, 76–79]. The simplest possibility to model hysteretic damping is to use a Kelvin-Voigt model
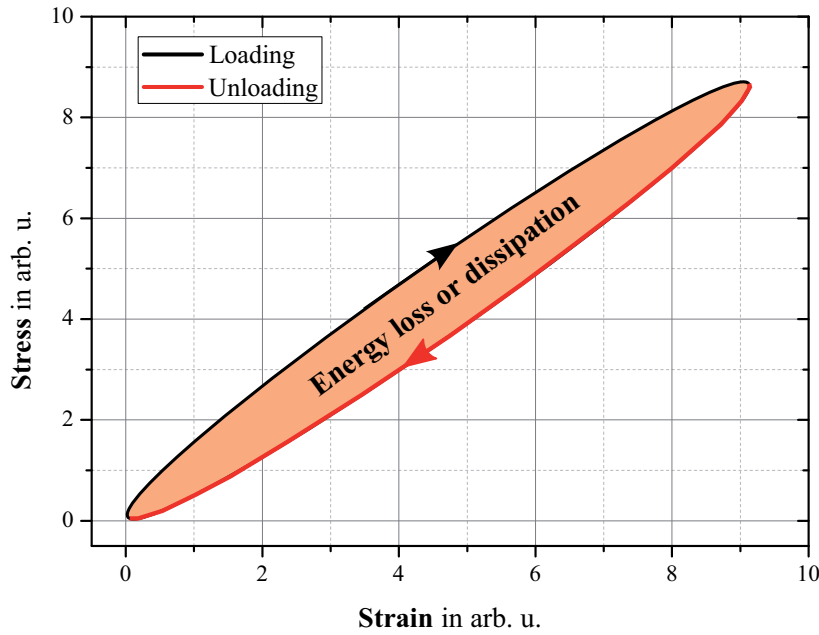
Figure 2.26: The stress-strain plot due to intrinsic damping mechansim.

$$\sigma_x = \underbrace{E \cdot \varepsilon}_{\text{elastic term}} + \underbrace{E^* \cdot \frac{\partial \varepsilon}{\partial t}}_{\text{damping term}} , \qquad (2.81)$$

where the term $E \cdot \varepsilon$ represents the elastic behavior of the material, which does not contribute to the damping. On the other hand $E^* \cdot \dot{\varepsilon}$ is responsible for damping effects, where E^* is the complex Young's modulus. This complex modulus can be expressed in different ways up to the used model. One common approach uses the following expression

$$E^* = E \cdot (1 + \mathrm{i}\eta) , \qquad (2.82)$$

where η is the loss factor, the reciprocal quality factor Q of a vibrating system. The quality factor Q is a dimensionless parameter describing how underdamped an oscillator or resonator is. The application of the hysteretic model is reasonable, when a material is subjected to cycling loads or if the system is not linear. If the response to a sinusoidal excitation is also sinusoidal the loss factor is well defined. Otherwise η can not be determined that easily [39]. Then it is necessary to restrict to the case where the stress cycles as well as the deformation responses are harmonic. In this case, the strain can be expressed sinusoidal. As a result, the stress consists due to Eq. (2.81) of two components. The elastic term is in phase with the strain, while the hysteretic damping term will be delayed in time by a phase angle ϕ, where $\tan\phi = \eta$.

An Excursion into Thermoelastic Damping: A very similar damping mechanism due to the stress of a vibrating structure is thermoelastic damping. Thermoelastic damping represents the energy transfer between the thermal and the mechanical domains of the resonator. The flexural oscillations are modeled as acoustic modes interacting with the thermally excited phonons of the vibrating structure. Through the interaction between the field of the mechanical stress and strain and the temperature field of thermal phonons, energy can be dissipated [80, 81]. Starting point of the thermal analysis is the linear one-way coupled heat-transfer equation

$$\underbrace{\rho c \frac{\partial T}{\partial t} = \lambda \nabla^2 T}_{\text{heat equation}} \underbrace{- \alpha T_0 \frac{\partial \sigma_x}{\partial t}}_{\text{thermoelastic term}} \,, \qquad (2.83)$$

where ρ is the density and c is the specific heat capacity of the structure, λ is the thermal conductivity, α denotes the coefficient of thermal expansion and T_0 is the nominal average temperature (300 K) [82]. The qualifier "one-way" implies that the stress field affects the temperature field, but not vice versa because for most crystalline solids the relative temperature change resulting from the thermoelastic effect is very small [83]. Both fields, the stress field $\sigma_x(\boldsymbol{x}, t)$ as well as the temperature field $T(\boldsymbol{x}, t)$ can be modeled with a harmonic ansatz introduced in the Kelvin-Voigt model of Eq. (2.81).
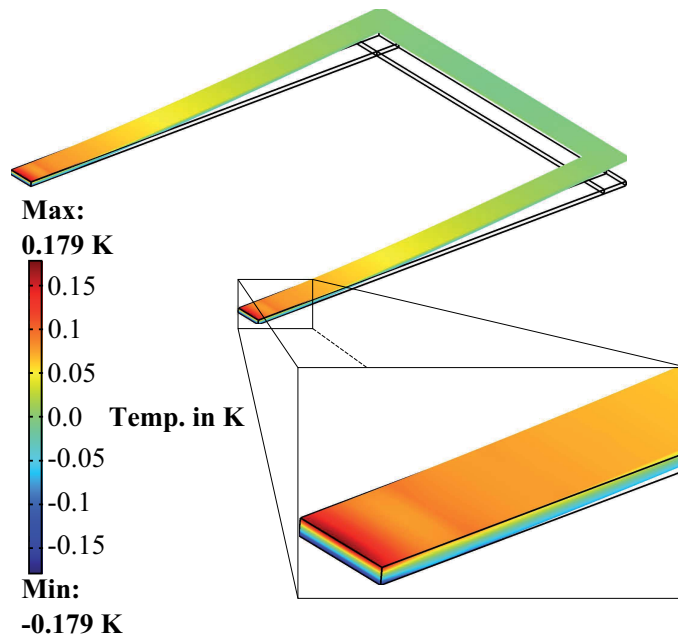
Figure 2.27: FEM simulation of thermo-elastic damping (TED) in an U-shaped cantilever with a length of 2 mm, a height of 20 μm and a width of one arm of 120 μm.

The FEM-simulation in Fig. 2.27 is a result of thermoelastic damping of a single-crystalline silicon U-shaped cantilever with a loss factor η of 0.001 or more conveniently written with a quality factor Q of 1000. Temperature differences in the range of 0.2 K pictured in Fig. 2.27

between the tip of the cantilever and the rigid suspension result in a length variation smaller than 1 nm (due to the geometric shape of the structure). This change in length is negligible due to the length of the cantilever in range of 2 mm. In the frequency regime of its fundamental resonances the influence of thermoelastic damping as measured by the total damping mechanism is negligible. Due to the analysis of Zener in 1937 and Lifshitz in 2000, where he introduced the quality factor of a thermoelastic damped beam

$$Q_{\text{TED}} = \left(\frac{E\alpha^2 T_0}{\rho c_{\text{p}}} \right) \cdot \left(\frac{6}{\xi^2} - \frac{6}{\xi^3} \frac{\sinh(\xi) + \sin(\xi)}{\cosh(\xi) + \cos(\xi)} \right)^{-1}$$

with

$$\xi = b\sqrt{\frac{\rho c_{\text{p}} \omega_0}{2\lambda}}\,, \tag{2.84}$$

where b is the width and ω_0 the eigenfrency of the beam [80]. The physical constants are E the Young's modulus, α the coefficient of thermal expansion, T_0 the nominal average temperature (300 K), ρ the density of the beam, c_{p} and λ denotes the specific heat capacity and the thermal conductivity of the structure. Due to Eq. (2.84) the quality factor of a thermoelastic damped U-shaped silicon cantilever, with a length of 2 mm and the width of one arm of 90 μm would be around $8 \cdot 10^{10}$. Assuming an effitive mass of 30 % of the computed oscillating mass of 24.5 ng and a theoretical stiffness of 7.65 N/m, the damping parameter D would be approximately $3 \cdot 10^{-15}$ Ns/m. With the experimental investigations of Sandberg et al. in 2004, thermoelastic damping is of no significance for eigenfrequencies below 100 kHz [84].

Beside this theoretical results it is worth thinking of the microscopic reason of thermoelastic damping in single-crystalline silicon. The lack of defects associated with grain boundaries gives monocrystals unique properties. However, the small but not negligible coefficient of thermal expansion of single-crystalline silicon require to take deviations from the linear law of force between the lattice atoms into account. Thermal expansion is an effect of higher terms of the potential between lattice atoms. They are responsible for the fact that for higher excited-states the equilibrium distance between neighboring atoms increases. Hence, the lattice constant increase with increasing temperature too. With the knowledge of anharmonicity one can explain the microscopic origin of thermoelastic damping in single-crystalline silicon as a result of a phonon scattering processes, like Umklapp (phonon-phonon) scattering at room temperature with sufficient acoustic phonon momentum. With increasing total phonon momentum $\mathbf{p} = \hbar\mathbf{k}$ the sum of two interacting phonon wave vectors $\mathbf{k}_1$ and $\mathbf{k}_2$ may point outside the 1$^{\text{st}}$-Brillouin zone. A $\mathbf{k}$-vector outside the first Brillouin zone is physically equivalent to vectors inside and can be transformed into each other by the addition of a reciprocal lattice vector $\mathbf{G}$. This process is called Umklapp scattering, which cause a change in the total phonon momentum. It is responsible for the limited thermal conductivity at high temperatures T for low defect crystals, with a characteristic $1/T$ dependence.

Additionally, it is worth mentioning that thermoelastic losses can be reduced by the MEMS-design. It was demonstrated by Candler et al. in 2006 using geometric techniques, like carefully placed open areas on the structure minimizing thermoelastic losses [85]. This is obvious when looking at Zener's description of thermoelastic damping in 1937. His calculation was based

on fundamental thermodynamic expressions for stored mechanical energy and thermal energy. He used coupled thermal-mechanical relations for stress and strain, entropy and temperature. Furthermore, he proposed that the strain and temperature solutions from uncoupled dynamical solutions are sufficient. Zener calculated the eigensolutions of the mechanical equation and separately from the uncoupled thermal equation. By applying these solutions to the coupled thermodynamic relationsships he calculated the quality factor Q_Z of a thermoelastic damped beam

$$Q_Z^{-1} = \left(\frac{E \alpha^2 T_0}{\rho c_p} \right) \cdot \frac{\omega_r \tau}{1 + (\omega_r \tau)^2} \tag{2.85}$$

for the fundamental flexural vibration mode [78]. With the mechanical resonance frequency ω_r and the characteristic time constant τ for a given thermal mode, he assumed that only thermal gradients across the beam width were significant. Hence, the characteristic time constant is

$$\tau = \frac{1}{\pi^2} \cdot \frac{\rho_p}{\lambda} \cdot b^2 \,, \tag{2.86}$$

where λ and b are the thermal conductivity and the width of the beam, respectively.

Support and Surface Losses

Further dependencies of the quality factor on the geometry of the vibrating structure was subject of systematic studies concerning support and surface losses [86–89]. Support loss, sometimes called as anchor loss is a result of the elastic vibration of the chip carrier, where the vibration energy of the beam resonator entering the support of the structure is lost. Judge et al. published in 2007 the energy dissipation due to the support loss of a cantilever based on a two-dimensional theory of elasticity, where the chip carrier is modeled as an semi-infinite elastic medium [90, 91]. During the flexural vibration of the beam, vibrating shear forces and moments will act on its clamped end, where they excite elastic waves. This waves will propagate into the support, absorbing some vibration energy of the cantilever. The support quality factor of a cantilever for the first flexural vibration mode is

$$Q_{\text{support}} = 3.226 \cdot \frac{l}{b} \left(\frac{l}{h} \right)^4 \,, \tag{2.87}$$

where l is the length, b is the width and h denotes the height of the cantilever, assuming a Poisson's ratio ν of 0.3. One important assumption of this model is that the vibration energy of the cantilever entering its support propagates away to large distances. As a result no energy is returned to the beam and the elastic wave in the support will not have an influence on the resonant modes of the cantilever.

Another damping effect was introduced by Yang et al. in 2002, where the surface to volume ratio of the cantilever plays an important role [87]. The surface to volume increases as the height

h compared to the length l scales down. As a result, the surface loss increase, most affected by the surface stress, which can be modified by absorbates or defects on the surface. The surface dissipation is modeled with a hysteretic model introduced in Chapter 2.3, where the surface quality factor of a cantilever becomes

$$Q_{\text{surface}} = \frac{bh}{2(b+3h)} \cdot \frac{E}{\delta E_{ds}} \,, \tag{2.88}$$

where E is the Youngs's modulus, b is the width and h denotes the height of the cantilever. The parameter δ and E_{ds} represents the thickness and the dissipative Young's modulus of the surface layer. In the case of a single-crystalline silicon cantilever, without an additionally surface layer, Hao et al. estimated the term $\delta E_{ds} = 0.81$ with a best-fit to minimize the error between the model and the experimental data [86].

A widely used quantity to determine the quality of the intrinsic damping mechnism is to build the resonance-frequency-quality-factor product. Additionally to Eq. (2.27) and with the knowledge of an acoustic wave propagating the solid, Landau and Lifshitz defined the sound aborption coefficient $\alpha(\omega)$ [44],

$$\alpha(\omega) = \frac{1}{2} \frac{\text{Mean energy dissipated}}{\text{Energy flux in the wave}} \,, \tag{2.89}$$

which is very similar to Eq. (2.27). The sound absorption coefficient is a measurable quantity and describes the variation of the wave amplitude with continuously propagation distance. Due to the strong relationship, the definition of Q and $\alpha(\omega)$ are related through

$$Q = 2\pi \frac{\omega_r}{2\alpha(\omega_r)c} \,, \tag{2.90}$$

where c represents the the wave velocity and ω_r is the resonance frequency of the structure [92]. Building the product $f_r \cdot Q$ leads to

$$f_r \cdot Q = \frac{\omega_r^2}{2\alpha(\omega_r)c} \,, \tag{2.91}$$

which is a fundamental measure for intrinsic dissipation mechanisms like thermoelastic, phonon-electron, and phonon-phonon interactions. The latter mechansim is the dominant intrinsic loss mechanism in semiconducting specimen at room temperature.

Extrinsic Damping

External damping results from boundary effects. An important form is structural damping. The origin of structural damping is rubbing friction, which result in stick-and-slip contact or impact. This can take place between structural components, which is often modeled by Coulomb damping. This damping mechanism describes the energy dissipation of rubbing dry-friction.

Another important form of external damping is fluid damping. When a structure, surrounded by air or water, moves in the fluid, a drag force appears. The energy dissipation due to this force may happen through internal fluid mechanisms such as viscosity, convection or turbulence.

Conditions in Modeling Structural Damping

Structural damping has its origin usually in nonlinear damping mechanisms, like fluid damping. If the interacting flow is turbulent the drag is nonlinear. On the other hand, structural damping in semiconductors is very small, where the damping parameter D is much smaller than unity. Therefore, the ambitious investigations to model structural damping result in simple damping models, such as linear viscous damping or coulomb damping where the friction only depends on the velocity and its sign. Nevertheless, all kinds of damping mechanisms attenuate resonance effects. In the simplest case of a mass-spring system the equation of motion is linear and, therefore, mode superposition applies. These model-simplifications results in Rayleigh damping, a special case of viscous damping.

Viscous Damping for Low-loss Systems

As musicians strike a single note with a tuning fork to reference to standard pitch, engineers can excite micro mechanical components due to their natural oscillations. The oscillations or modes are characteristic to the vibrating system itself and allow in addition to the static analysis a description of the dynamic system. Besides the experimental characterization of the dynamic behavior of oscillating bodies with e.g., Laser-Doppler vibrometry the eigenmodes of MEMS components can be analyzed and displayed graphically with FEM. Crucial modes can be discovered and eliminated by specific changes of the design of the components, e.g. by the choice of the materials or by changing the stiffnesses. Additionally, modal analysis can afford a more complex analysis of the structure as a starting point for a transient or harmonic analysis. Modern finite element programs like COMSOL Multiphysics determines automatically during the analysis of the Jacobi matrix or the specified contraints whether it uses linear or nonlinear solvers which e.g are necessary for problems of the fluid mechanics, described by the incompressible Navier Stokes equation. Furthermore, the modal analysis of COMSOL Multiphysics permits the integration of possible damping mechanisms such as Rayleigh damping.

Rayleigh Damping and Results of FEM-Simulations: This model describes the damping matrix as a linear combination of the mass $\boldsymbol{m}$ and stiffness $\boldsymbol{k}$ matrices and is therefore often called proportional damping. In the simplest case m and k represents scalars. A general assumption of the Rayleigh damping model is that the damping parameter

$$D = \alpha m + \beta k \tag{2.92}$$

depends linear on the mass and the stiffness with α and β as the predefined constants. Rayleigh damping is one of the simplest velocity dependent damping models. Velocity dependent damping models are so-called general viscous damping models, a special form of modal damping, where a dimensionless damping factor

$$\zeta_i = \frac{\alpha}{2\omega_i} + \frac{\beta\omega_i}{2} \tag{2.93}$$

is defined for each mode featuring an angular eigenfrequency ω_i. For weakly damped systems hysteretic damping introduced in this chapter evolves convergently into viscous damping [39]. Rayleigh damping takes into account that modal (or generalized) mass participation decreases as D will increase for higher modes. Although Rayleigh damping for 1-DOF system deals with constants α and β, where the prediction for higher modes will surely not be realistic, Fig. 2.28 demonstrates some interesting results. For lower frequencies the mass term prevails and the curve is nonlinear. While for higher frequencies the relationship becomes linear. In the case of high quality factors this relationsship gets constant because as β decrease the quality factor Q increases.
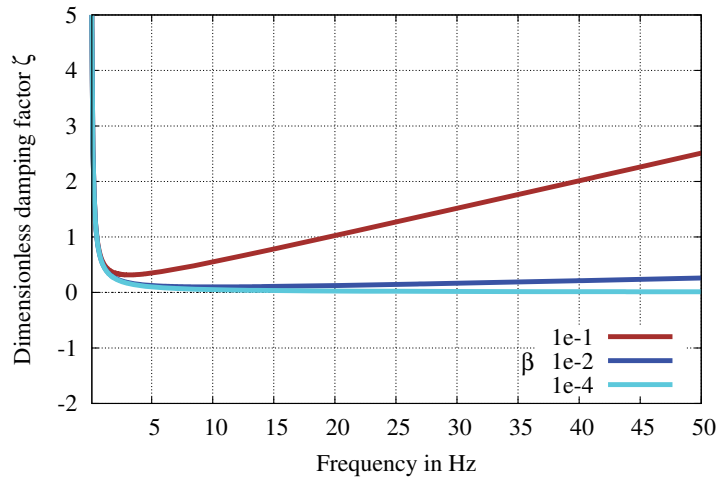
Figure 2.28: Dependence of the damping parameter ζ on the resonance frequency and the damping constant β of the system (α=1).

In summary, modal damping can be neglected for vibrating structures with resonant frequencies around 10 kHz and quality factors in the range of a few thousands. This independence of the resonance frequency from weak modal damping is demonstrated in a parametrized FEM-simulation for different geometries in Fig. 2.30, where one can recognize a characteristic cut off for quality factors smaller than 500.

In a more detailed simulation Fig. 2.31 one gets a geometry dependence of modal damping for decreasing quality factors, where U-shaped cantilevers promise a proper functionality down to Q-factors of 60. Therefore, only U-shaped cantilevers will offer resonant enhancement of sensitivity close to atmospheric pressure, as the the quality factor decrease dramatically with increasing ambient pressure. In Fig. 2.30 the resonance frequency of the vibrating structure depending on the quality factor Q is depicted. For a lightly damped mass-spring system, the quality factor Q represents the effect of viscous damping or drag. Combining Eq. (2.11) and 2.15 leads to

$$Q = \frac{\sqrt{mk}}{D},$$ (2.94)

where the drag or damping force is proportional to the velocity of the body mass. Due to Eq. (2.94) one has to know the mass and the stiffness of the cantilever. One possibility to calculate the stiffness of a trapezoidal shaped cantilever is with the aid of the strain energy

$$\frac{1}{2}Fx_s = \frac{1}{2}\int_0^l \frac{M^2(x)}{E\,J_z(x)}dx$$ (2.95)

with

$$J_z(x) = \frac{c\,h^3}{12} \cdot \left[1 + \left(\frac{a}{c} - 1\right)\frac{x}{l}\right],$$
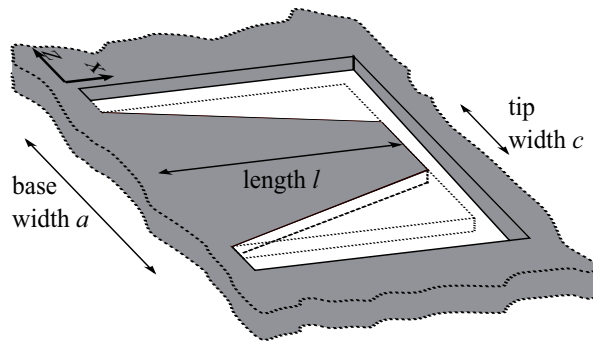
Figure 2.29: A cantilever with constant height, but a linear shifting width b.

where F is the applied force and x_s is the static displacement due to the load at the tip of the cantilever, M denotes the bending moment and $EJ_z(x)$ the bending stiffness schematically shown in Fig. 2.29. After a short supplementary calculation the displacement u_A becomes

$$x_{\mathrm{s}} = \frac{F\, l^3}{E\, J_0} \cdot \frac{c^3}{(a-c)^3} \cdot \left[\frac{1}{2}\left(\frac{a}{c}\right)^2 - 2\frac{a}{c} + \frac{3}{2} + \ln\frac{a}{c} \right] \tag{2.96}$$

where

$$J_0 = \frac{c\, h^3}{12} \; .$$

With the help of l'Hospital's rule it is possible to show that Eq. (2.96) merge into

$$\lim_{a \to c} x_{\mathrm{s}} = \frac{F l^3}{3\, E\, J_0} \; , \tag{2.97}$$

the well known formula of the deflection of a simple loaded cantilever. So it is possible to get the stiffness k with Hooke's Law $F = k \cdot x_{\mathrm{s}}$. Together with Eq. (2.94) a rough estimation of the quality factor Q is feasible.
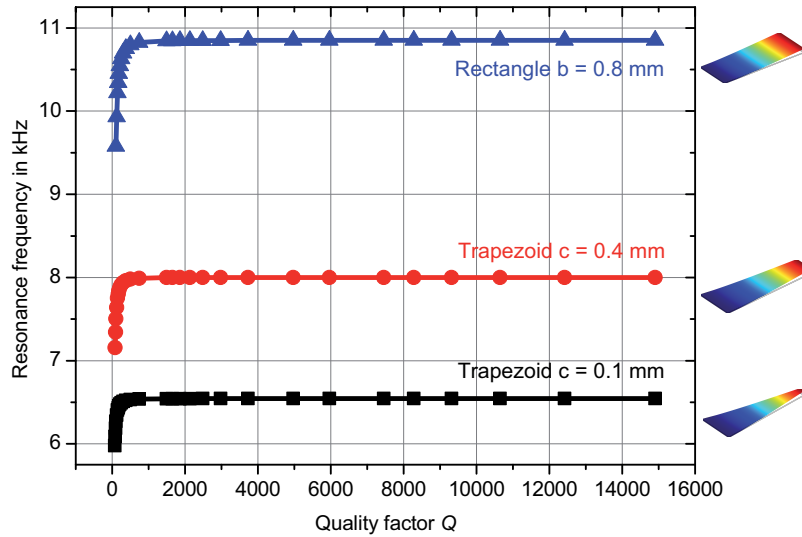
Figure 2.30: The resonance frequency of the flexural mode as a function of the quality factor for three different geometries due to their different base length but of the same height $h = 20\,\mu\mathrm{m}$.
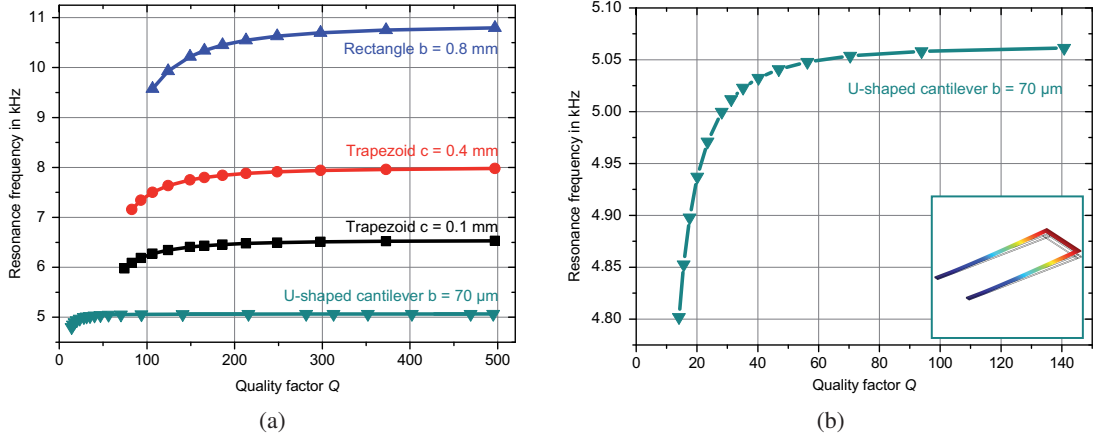
Figure 2.31: Extended quality factor over a wide pressure range due to the U-shaped cantilever. Fig. (a) depict qualitiy factors of different shaped cantilevers, where Fig. (b) shows typical quality factor values of an U-shaped cantilever around standard pressure.

Eddy Current Losses

When a electrical conductive material is subjected to a time-varying magnetic field, eddy currents are generated in the conductor. This time-varying magnetic field can be induced either by the movement of the conductor or by changing the strength of the source of the magnetic field. Once the eddy currents are generated, they circulate in such a way that they induce a magnetic field with opposite polarity as the applied field B (dependent on the shape of the conductor). This induces a repulsive force. Due to the electrical resistance of the conducting material, the induced currents will dissipate heat whereas the external force will be partly compensated.

In the case of a dynamic system, the conductive material is continuously moving in the magnetic field sensing a continuous change in magnetic flux causing an electromotive force. Furthermore, the induced currents causes a repulsive force that is proportional to the velocity of the conductive metal. Since the currents are dissipative, power is drawn from the system, where the magnet and the conductor acts like a viscous damper [93].

In the case of a moving highly doped cantilever with a maximum displacement u_A und the width b the structure encircles a magnitude change in flux $\dot{\Phi} = \omega B b u_\mathrm{A} = U_\mathrm{ind}$. The induced voltage will dissipate into $P_\mathrm{E} = U_\mathrm{ind}^2/R$ and

$$1/R = \sigma \frac{hl}{2b}, \tag{2.98}$$

where σ is the electric conductivity, h the height, b is the width and l is the length of the cantilever. Owing to the high doped cantilever one can assume an ohmic behavior of the structure and $h \ll b$. The assumption that the heat will dissipate through the whole length l of the cantilever is the worst-case scenario and scarcely thinkable. However, the power dissipation
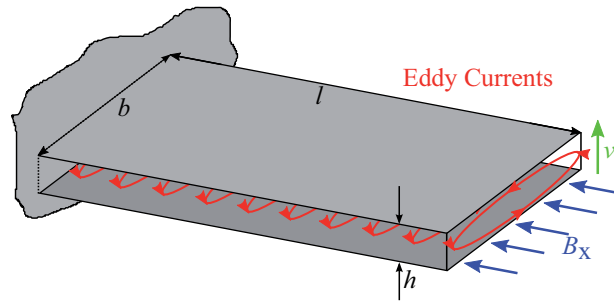
Figure 2.32: Schematic diagram of a cantilever passing through a magnetic field and the generation of eddy currents.

$$P_{\mathrm{E}} \approx \underbrace{\frac{1}{2}\sigma h b l B^2}_{D_{\mathrm{E}}} v^2 = F \cdot v = D_{\mathrm{E}} v \cdot v \qquad (2.99)$$

allows an upper bound estimation of the viscous damping parameter D_{E} due eddy currents. For typically parameters like $\sigma \leq 1 \cdot 10^4 \, \Omega^{-1} m^{-1}$, h =20 µm, b =1.5 mm, l =2 mm and a magnetic field B =10 µT of air-core coil, the damping parameter D_{E} becomes at its maximum $3 \cdot 10^{-11}$ Ns/m. Additionally the driving frequencies are in the range of 10 kHz and amplitudes less than 1 µm. Hence, eddy current losses in single-crystalline silicon cantilevers are small, but measurable [94]. In reality eddy current problems are very challenging from the mathematical point of view due to the Helmholtz equation. A comprehensive introduction was represented by Kriezis et al. in 1992 [95].

Fluid Damping

Beside structural damping, fluid damping mechanism are of most importance. The energy dissipation of fluid damping may happen through internal fluid mechanisms such as viscosity, convection or turbulence. Fluid damping tends towards nonlinearity if the interacting flow is turbulent, where the drag force is nonlinear in the relative velocity. Generally fluid-structure interactions can be classified either in internal or external, i.e. fluid-structure problems. External fluid-structure interactions are, e.g. the flight of airplanes or birds and the swimming of fish. Internal fluid-structure interactions govern, e.g. the flow through pipes or blood vessel and sloshing of liquids in containers.

One of the simplest fluid-structure models deals with added masses. When somebody moves his hands and arms in the air and afterwards in the water he will feel an additionally resistance. In the case of an oscillating pendulum in the air and in the water, one can give an elementary theory for the period of the pendulum motion. Stokes assumed in 1850 a pendulum with a solid sphere with the radius r and the mass m suspended by a string of the length l like Fig. 2.33. The square of the angular eigenfrequencies becomes

$$\omega^2_{\text{vacuum}} \approx \omega^2_{\text{air}} = \frac{g}{l} \tag{2.100}$$

$$\omega^2_{\text{water}} = \frac{1}{1+\alpha}\frac{g}{l}, \tag{2.101}$$

where g is the gravitational acceleration and $\alpha = m_{\text{a}}/m$ with the added mass m_{a} [96]. The equation of motion under the approximation of small-angles ($\sin\Theta \simeq \Theta$) is

$$\ddot{\Theta} + \frac{1}{1+\alpha}\frac{g}{l}\Theta = 0 \tag{2.102}$$

where

$$\lim_{m_{\text{a}}\to 0} \alpha = 0 \tag{2.103}$$

including a fluid drag mechanism with an added mass. In 1850 G. G. Stokes presented the effects of the added mass,

$$\alpha = \left(\frac{1}{2} + \frac{g}{4\nu r}\right) \cdot \frac{\rho_{\text{fluid}}}{\rho_{\text{sphere}}}, \tag{2.104}$$

taking account the buoyancy, hence the densities of the ρ_{fluid} and of the solid ρ_{sphere} and the kinematic viscosity ν of the fluid, too. The effect of an added mass results in a reduction of the system resonant frequency. Although the added mass model neglects the air stiffness, it helps to understand the physics of fluid-structure interactions. In general, further refinements are necessary, often leading in a challenging complexity of the model.

The fluid–structure interaction of vibrating cantilevers immersed in a fluid has been extensively studied [47, 97, 98]. Essentially there are two ways of modeling a flow field around the structure. Either from the atomistic point of view, modeling the fluid as a collection of molecules, or phenomenolgical as a matter of continuum. The atomistic models make use of probabilistic methods, while the continuum approach deals

Figure 2.33: A simple pendulum oscillating in a fluid. The string on which the solid sphere swings is massless and inextensible.

with macroscopic quantities like density, pressure, velocity, etc. which are defined for every spatial and temporal condition of the fluid. Conservation principles lead to nonlinear partial equations. The continuum approach covers the Navier-Stokes equations, applicable to numerous flow situations. For rarefied gas flows near equilibrium, the Navier-Stokes equations are easier to handle both analytically and numerically than the molecularly-based Boltzmann equation. As a consequence, continuum models are used as long as they are applicable [99].

To consider wether to use a continuum approach or an atomistic one, there are three dimensionless parameters which determine the flow regime: the Mach number M, the Knudsen number Kn and the Reynolds number Re [100]. For typical MEMS applications two of them, $M \propto Re \ll 1$, are negligible because of subsonic vibration velocities. This leaves the Knudsen number as the most important fundamental parameter,

$$Kn = \frac{\lambda}{b} = \frac{k_{\mathrm{B}}T}{\sqrt{2}\pi p \sigma^2 b}, \tag{2.105}$$

where λ is the mean free path, k_{B} is the Boltzmann constant, T is the ambient temperature, in case of air, the diameter of molecules is $\sigma = 4.19 \cdot 10^{-10}$ m and b denotes a characteristic length of the vibrating structure [101]. For gases, the mean free path is the average distance of a traveling gas molecule between successive collisions with other interaction partners. Due to Eq. (2.105) the Knudsen number is a comparatively dimension and therefore scalability is ensured. Rarefied gas flows are encountered as well as flows through small geometries like MEMS devices or low-pressure applications such as high-altitude flying and high-vacuum apparatus. The Knudsen number in the flow determines the quality of rarefaction effects, hence the Knudsen number Kn is a quantitative criterion for the continuum approach.

At the lower bound, where $Kn \to 0$ the time- and length-scales of molecular collisions are infinitesimal small compared to those for the continuum flow. For example, each air molecule experiences at standard conditions 10 collisions per nanosecond and travels thereby 1 µm on the average [102]. The velocity along the fluid dimensions instantaneously adjusts to the equilibrium thermodynamic state. This equilibrium is appropriate to the local macroscopic properties of the molecules moving through the flow field.

As Kn increases, rarefaction effects are more pronounced, where the continuum approach breaks down. In the continuum regime, the gas molecules interact with the borders of the surrounding structures, where the gas adjust to the ambient temperature. This adaption process is called full momentum accommodation, due to fundamental relation between temperature and movement of the molecules. This boundary condition is the challenge of rarefied gas flows. Due to the small collision frequency of the molecules with the boundaries, a thermic jump between the wall and the gas temperature can appear, hence a component of the gas-velocity tangential to the wall occur, where the molecules can slip along the borders (without accomodation).

At the upper bound of Eq. (2.105), where $Kn \to \infty$, the mean free path of the molecules exceeds the characteristic length. Here the molecules moves ballistic, only interacting with the boundary and molecular collisions become irrelevant. The different Knudsen number regimes are determined empirically and listed in Table 2.3.

Both in the continuum and molecular regime the quality factor of a vibrating cantilever is pressure independent [47]. The transition or quasi-molecular regime coincides with Knudsen numbers in the range of 0.1 to 10, whereas at the lower bound the molecular flow enters into the slip flow. The names molecular and quasi-molecular regime indicate that the conventional equations of continuum theory are inappropriate to describe rarefied gas transport. Continuum damping requires a sufficient particle density in the flow, which is not guaranteed in the transition regime. The calculation of transition flows can only be carried out on the basis of the gas kinetic theory, where the characteristic equation is the Boltzmann-equation.

Table 2.3: Knudsen number regimes and their corresponding flow.

Characteristic flow regime			
Continuum reg.	0	$< Kn <$	10^{-2}
Slip-flow reg.	10^{-2}	$< Kn <$	10^{-1}
Transition reg.	10^{-1}	$< Kn <$	10
Free-molecular flow reg.	10	$< Kn <$	∞

The dominant damping mechanisms in the transition regime are structure-molecular and intermolecular collisions. Analytical solutions of the Boltzmann equation in the quasi-molecular regime do not exist, but several approximations like the Burnett equation are available. Rarefaction effects were incorporated by Veijola et al. into the linearized Reynolds equation using an effective viscosity model, which permits the predictions of the flow in rarefied gases [103]. The Reynolds equation is a simplification of the Navier-Stokes equation. Hence, it stands for a continuum approach that is adapted to the transition between the macroscopic and microscopic description of rarefied gas flows [104]. But the Navier-Stokes equation in turn applies only to a subset of problems covered by the Boltzmann equation. The latter ensures not only a complete description of the free molecular flow, but implies also continuum flows as an approximation. A numerical solution of the latter based on the DSMC (direct simulation Monte Carlo) method was chosen by Alexeenko et al., and a promising analytical ansatz was introduced by Suijlen et al. in 2009 [105, 106].

Gas Kinetic Damping in the Transition Regime

One possibility to get a better insight into the transition regime is to use the assumptions of the free molecular flow and to compare the systematic deviations of the measurement results with the analytical solutions of the free molecular flow. As an important precondition for the experimental investigation, surrounding surfaces from the bulk silicon, the chip support and the measurement chamber are sufficiently distant from the cantilever so that their influence on the damping of the fundamental mode of the device can be neglected. This situation was treated first by Drawin in 1962. The related dissipative drag parameter describes

$$f_1 = k_{\mathrm{m}} b p, \tag{2.106}$$

where k_{m} is the damping coefficient, b the width of the cantilever and p the ambient pressure [107]. The idea of his derivation is based on a net difference of the particle density between the top and the bottom side of the vibrating cantilever. In consequence, a nonzero molecular pressure difference acts on the cantilever, which counteracts the propulsive forces. Several publications have laid emphasis on the determination of the damping coefficient due impinging molecules, but Martin et al. in 2008 has given an upper limit

$$k_{\mathrm{m}} = \frac{C_{\mathrm{D}}}{c} = 3.9008/c, \tag{2.107}$$

with full momentum accommodation, where the damping coefficient is expressed in terms of the most probable speed c (= thermal speed) and a damping parameter C_D [47, 108, 109]. Thermal effects, like thermic jumps are completely neglected, but the result of Eq. (2.107) is valid for a wide range of MEMS cantilevers, where the height h is much smaller than the width b of the beam. The minimum quality factor of a cantilever can be retrieved by combining Eq. (2.47), 2.106 and 2.107

$$Q_\mathrm{kinetic} = \frac{\rho h \omega}{p} \frac{c}{C_\mathrm{D}}, \qquad (2.108)$$

with a dominant damping mechanism due to structure-molecular collisions in the quasi-molecular regime.

Squeeze-film Damping in the Transition Regime

In the range of Knudsen numbers $Kn \ll 1$ viscous damping mechanisms like squeeze-film damping dominate the gas-structure interactions. Viscous squeeze-film damping is well known and exactly analyzed [99, 110]. Due to flexural vibrations of the cantilever perpendicular to a fixed wall the gas in between is compressed [110]. The gas can partially escape through air slits between the moving cantilever and the fixed surface, which induces losses since compression work is removed from the compartment and therefore not fully recovered.

Suijlen et al. proposed in 2009 a model of a squeezed-film damped beam in the molecular regime [106]. The basic idea of this derivation is a variation of the particle density between the vibrating cantilever and the fixed wall. The dynamic behavior of the beam counteracts the random walk of the gas molecules which are forced to sustain a steady-state particle density in the gap. For harmonic motion, this results in a complex-valued force, where the imaginary part of the force is out of phase with the amplitude and in counter-phase with the velocity of the moving cantilever. This results in an additional damping. But the gas will not move instantaneously through the gap, which contributes to the phase shift. The molecular diffusion maintain to equalize the pressure differences in- and outside the gap, where the diffusion time

$$\tau = \frac{8}{\pi^3} \cdot \frac{A}{(d\bar{c})} \qquad (2.109)$$

of the gas molecules is calculated from the Brownian motion. In Eq. (2.109) A is the surface area of the cantilever, d is the averaged distance between the moving cantilever and the fixed wall and $\bar{c}$ is the mean speed of the gas molecules (Maxwell–Boltzmann distribution). If $1/\tau \gg \omega$ the real part of the of the complex-valued force is negligible. Hence the dissipative drag parameter per unit length (of the cantilever) becomes

$$f_1 = \frac{pb}{d} \frac{\tau}{1 + (\omega\tau)^2}. \qquad (2.110)$$

In an earlier publication by Legtenberg et al. in 1995 it was already speculated that in the quasi-molecular regime not only kinetic, but also squeeze-film damping lowers the quality factor Q [111]. According to the calculations of [46, 47, 106] the quality factor of a squeezed-film damped cantilever in the free molecular regime becomes

$$Q_{\text{squeeze}} = \frac{\rho h d \omega}{p} \cdot \frac{1 + (\omega\tau)^2}{\tau} .$$ (2.111)

In a superposition of both damping mechanisms, kinetic and squeeze-film damping, a satisfactory characterization of the damping behavior of an oscillating cantilever in the quasi-molecular regime with Knudsen numbers in the range of 10 down to 0.02 can be achieved.

Superposition of Damping Effects

Due to Eq. (2.27) the total quality factor of a cantilever is

$$Q_{\text{tot}} = \frac{2\pi E_i}{E_d} = \frac{2\pi E_i}{E_{d|\text{int}} + E_{d|\text{ext}}} ,$$ (2.112)

where $E_{d|\text{int}}$ and $E_{d|\text{ext}}$ denotes the dissipative energy parts of E_d due to intrinsic and extrinsic damping mechansims. Hence the quality factor Q can then be written as an inverse sum of an intrinsic quality factor Q_{int} and an extrinsic quality factor Q_{ext}

$$Q_{\text{tot}} = \left(\frac{1}{Q_{\text{int}}} + \frac{1}{Q_{\text{ext}}} \right)^{-1} .$$ (2.113)

Intrinsic damping mechanisms include thermoelastic and structural damping, support and surface losses, while extrinsic damping mechanisms comprise gaskinetic and squeeze-film damping in rarefied gases, viscous damping mechanisms at the upper bound of the ambient pressure regimes and eddy current losses. For driving frequencies in the range of 10 kHz, amplitudes less than 1 μm and Knudsen numbers Kn in the range of approximately 0.01 up to 10, viscous damping, thermoelastic damping and eddy current losses are negligible. Therefore the most important damping mechansims can be summarized to the total quality factor

$$Q_{\text{tot}} = \left(\frac{1}{Q_{\text{support}}} + \frac{1}{Q_{\text{surface}}} + \frac{1}{Q_{\text{kinetic}}} + \frac{1}{Q_{\text{squeeze}}} \right)^{-1} .$$ (2.114)

Combining Eq. (2.87), 2.88, 2.108 and 2.111 enable the determination of the maximum total quality factor according to the length l and ambient pressure p, whereas the height h and width b of the cantilever are fixed, which is shown in Fig. 2.34. With decreasing ambient pressures the quality factor increases. The maximum computed quality factors for cantilevers with a length of at most 10 mm is approximately $2 \cdot 10^6$, which is in the range of measured quality factors for single-crystalline silicon structures in literature [112]. In practise, several constraints can lower these maximums of the total quality factor, like the assembly of several layers of the vibrating structure or of the chip carrier [113]. Another limitation results from the assumption of a semi-infinite elastic medium of the chip carrier in contradiction to a finite mass ratio of the vibrating structure to the support [89].

Nevertheless, the computed maxima of the total quality factors in respect to the length of the cantilever and to the ambient pressures enable to determine intrinsic and extrinsic dominated damping regimes, which is schematically shown in Fig. 2.35.
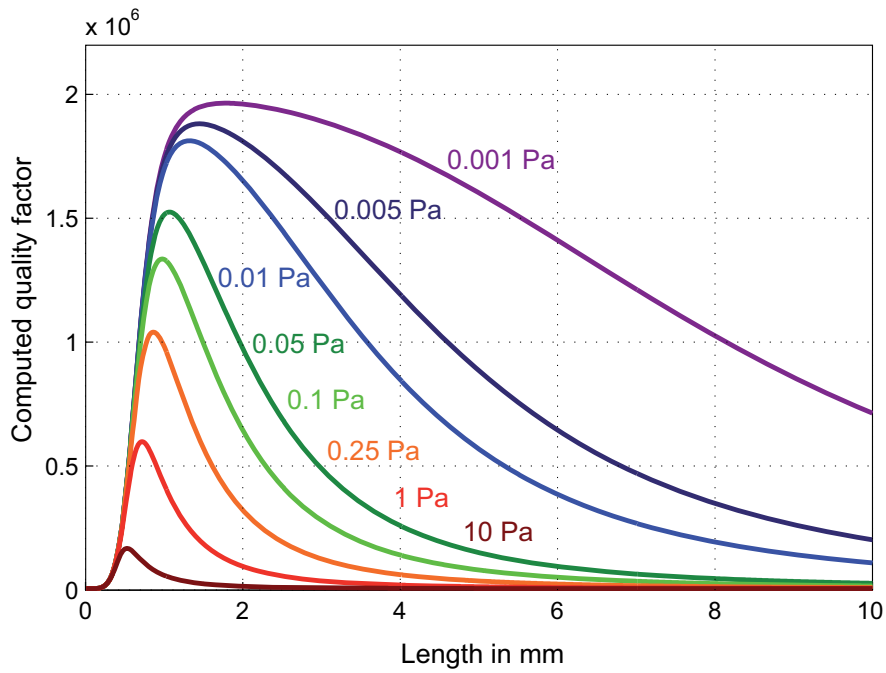
Figure 2.34: The total quality factor Q_{tot} as a function of the length l for cantilevers with the same height h=20 μm and width b=1.5 mm.

The most important geometrical parameter for the quality factor are the length and the height of the cantilever. In Fig. 2.36 both parameters are varied over a wide range, resulting in a typical crest, which seperates the inctrinsic from the extrinsic damped dominated region.

To get a feeling what maximum quality factors can be found in literature see Table 2.4.
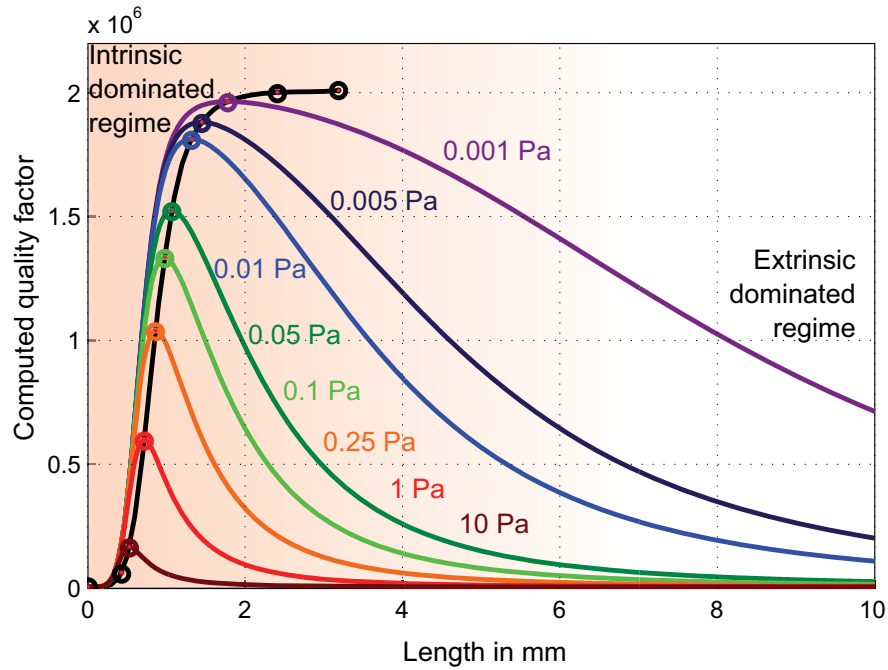
Figure 2.35: A quantitative determination of intrinsic and extrinsic dominated damping regimes at room temperature.

Table 2.4: Resonant frequency and quality factor of high-Q resonators reported in literature.

Resonator design	Res. freq. f_r in MHz	Quality factor Q	$f_r \cdot Q$	Ambient pressure in Pa	Temp. in K
Cantilever [114]	0.075	$3.51 \cdot 10^5$	$2.63 \cdot 10^{10}$	Vacuum	Room temperature
Lamé-mode [115] square	6.35	$1.7 \cdot 10^6$	$1.08 \cdot 10^{13}$	$5 \cdot 10^{-3}$	n.s.
Wine glass [116] disk	5.4	$2 \cdot 10^6$	$1.08 \cdot 10^{13}$	1.3	n.s.
Lamé-mode [117] square	4.126	$5.49 \cdot 10^6$	$2.27 \cdot 10^{13}$	5	n.s.
Torsional [118] plate	0.0085	$6.7 \cdot 10^7$	$5.7 \cdot 10^{11}$	n.s.	0.4
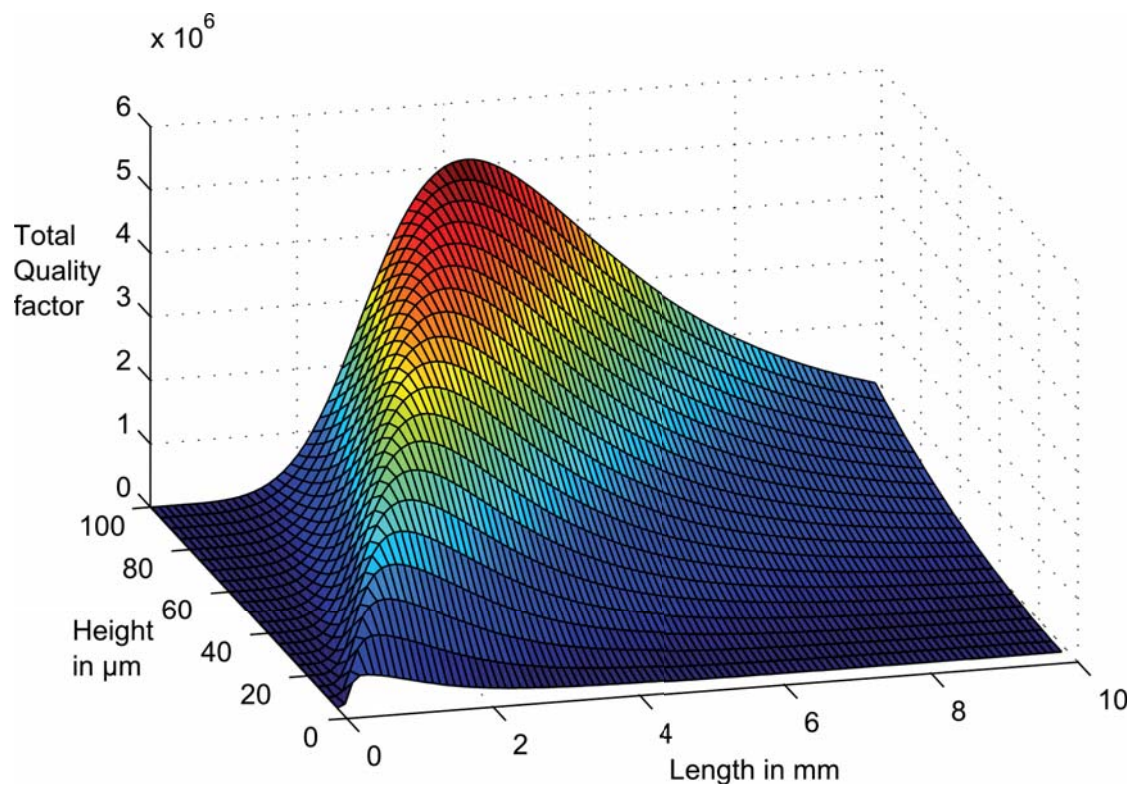
Figure 2.36: A 3D-view of the maximum of the total quality factor as a function of the length and the height of the cantilever at constant ambient pressure of 0.01 Pa and at room temperature.

Basics of Microelectromechanical Systems

Overview

This chapter exclusively deals with the transducer properties of the MEMS resonant sensor, shown in Fig. 3.1. Fundamental aspects are derived from the well-known concepts, like the plate capacitor.
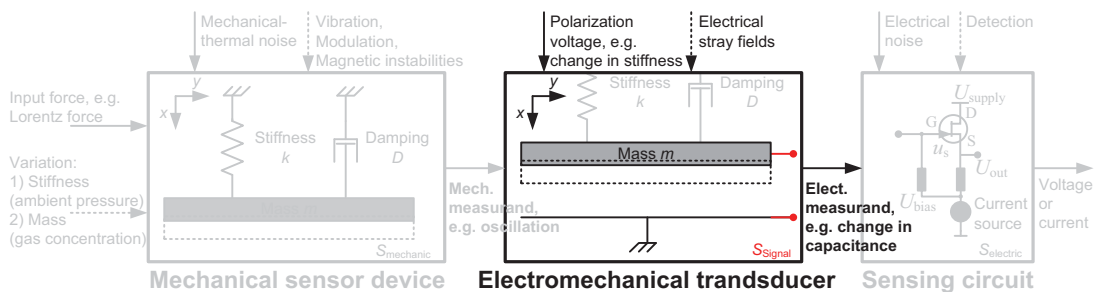
Figure 3.1: Classification of a microelectromechanical system, where the emphasis is laid on the electromechanical transducer.

3.1 Electrical Equivalent Model

One Port Configuration

Due to the electrostatic sensing the cantilever is set to a polarization voltage U_p to provide the bias for a capacitive detection. The polarization voltage $U_p = U_{ext} - U_{bias}$ is a combination of

the bias voltage U_{bias} of the sens electrode and the DC-part U_{ext} along the cantilever. Owing to the reciprocal quadratic dependence of the electrostatic force to the distance of the charges, the driving force in Eq. (2.62) becomes nonlinear. The current through the lead of the cantilever is driven by an ac voltage u_{ac} which combines with the polarization voltage U_{p}. The ac voltage developed at the sense electrode u_{s} is generated by the vibration of the cantilever and is dependent on the drop of the drive voltage u_{ac}. The origin of the motional feedback is the product of the DC polarization voltage U_{p} and the ac sense voltage u_{s}. Hence the 1D-differential equation describing the motion of a linear electro-mechanical system (neglecting the Lorentz force F_{L}) is

$$m\ddot{x} + D\dot{x} + (k_{\text{m}} - k_{\text{e}})x = \frac{\varepsilon A}{(d_0 - x_0 - x)^2}U_{\text{p}}u_{\text{s}} \tag{3.1}$$

where $d = d_0 - x_0$ is the equilibrium distance. A source follower is assumed to be the amplifier to sense the cantilever vibrations. At the sense electrode $U_{\text{s}} = U_{\text{p}} + u_{\text{s}}$ is valid, and the current

$$i_{\text{s}} = \frac{\mathrm{d}}{\mathrm{d}t}(C \cdot U_{\text{s}}) = U_{\text{s}}\frac{\partial C}{\partial t} + C\frac{\partial u_{\text{s}}}{\partial t} \tag{3.2}$$

is flowing through the sense electrode capacitance $C(t)$ and is injected into the input node of the source-follower. $C(t)$ varies according to the motion of the cantilever. Apart from the possibility to control the dynamic behavior of the cantilever through the polarization voltage U_{p}, harmonics with double frequency will occur, as a result of the quadratic dependence of the electrostatic force.
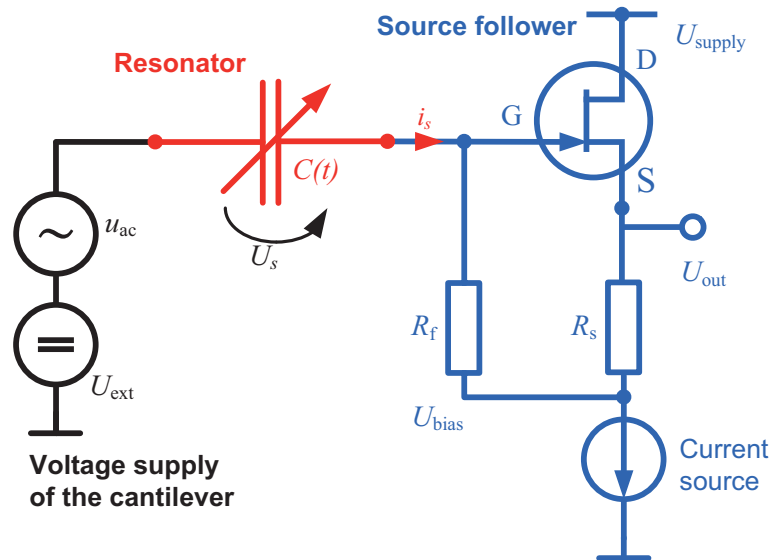
Figure 3.2: Capacitive detection scheme for one sensing electrode used to detect the cantilever's vibration. With a capacitive decoupling, the voltage component U_{ext} is kept constant throughout the cantilever.

Consequently the coefficient of $\partial u_s/\partial t$ in Eq. (3.2) can be approximated as a static capacitance $C_e = \varepsilon A/(d_0 - x_0)$ of the new equilibrium position. In the case of $U_p \gg u_s$ the sensing current i_s of Eq. (3.2) simplifies to

$$i_s = \frac{\mathrm{d}}{\mathrm{d}t}(C \cdot U_s) = \underbrace{U_p \frac{\partial C}{\partial t}}_{i_m} + \underbrace{C_e \frac{\partial u_s}{\partial t}}_{i_e} \tag{3.3}$$

where electrical network theory can be applied. This step allows us to split the electro-mechanic oscillating system into a mechanic domain and a therefrom separated electric domain [119]. Thus, the expression of the motional current simplifies to

$$i_m = U_p \frac{\partial C}{\partial x} \frac{\partial x}{\partial t} \approx U_p \frac{\varepsilon A}{d^2} \frac{\partial x}{\partial t} , \tag{3.4}$$

which leads to an electromechanical coupling between the motional current and the velocity of the resonator

$$\left. \frac{\partial x}{\partial t} \right|_{x \ll d} = \frac{d^2}{\varepsilon A} \cdot \frac{i_m}{U_p} . \tag{3.5}$$

This assumption allows to perform Eq. (3.1) into an equivalent electrical differential equation

$$\frac{d^2}{\varepsilon A U_p} m \ddot{x} + \frac{d^2}{\varepsilon A U_p} D \dot{x} + \frac{d^2}{\varepsilon A U_p}(k_m - k_e)x = u_s$$

$$\underbrace{\left(\frac{d^2}{\varepsilon A U_p}\right)^2 m \cdot \frac{\partial i_m}{\partial t}}_{L} + \underbrace{\left(\frac{d^2}{\varepsilon A U_p}\right)^2 D \cdot i_m}_{R} + \underbrace{\left(\frac{d^2}{\varepsilon A U_p}\right)^2 (k_m - k_e)}_{1/C} \cdot \int i_m dt = u_s . \tag{3.6}$$

The resulting differential equation is the description of a RLC-serial resonant circuit. Using the definition of an electromechanical coupling factor $\kappa^2 \equiv (\varepsilon A U_{DC}/d^2)^2$, an equivalent relationship between elecrical and mechanical quantities can be specified to

$$L = \frac{m}{\kappa^2}, R = \frac{D}{\kappa^2} = \frac{\sqrt{mk}}{\kappa^2 Q} \text{ and } C = \frac{\kappa^2}{k_m - k_e} . \tag{3.7}$$

One interpretation of the coupling factor κ could be the amount of energy conversion from the electrostatic domain into mechanical energy. Typical values of these lumped parameters in MEMS applications are L=40 kH, R=30 kΩ and C=10 fF, where C_e=1 pF. The capacitor C_e builds a parallel-resonance, where the parasitic feedthrough capacitance can influence the measured signal. This can lead to a shift of the resonant peak level, where usually the peak becomes

to small to evaluate the quality factor Q. In order to increase the system response, the electromechanical coupling factor κ^2 can be increased by increasing the polarization voltage U_p or decreasing the equilibrium electrode gap d.

In summary, the motional current i_m is related to the velocity of the resonator and i_e is the electric capacitive current of the static capacitance C_e, schematically shown in Fig. 3.3. Both current paths together build a so-called BVD (Butter-worth Van-Dyke)-resonator, which plays an important role in the modeling of piezoelectric resonators [120, 121]. Starting from these considerations it is possible to model the electromechanical system with an equivalent electrical circuit composed of inductors, resistors, and capacitors. This electromechanical analogies are the result of similarities of the differential equations that are suitable to describe both the mechanical system and their electrical equivalent circuit.

Furthermore, is the motional current of most importance for the spectral dependence, due to the sense voltage u_s. He generates a power dissipation through the characteristic high impedance of the source follower, which is substituted by a high-resistance R_sub and a capacitor C_sub in parallel. A major difference between the electric current i_e and the motional current i_m is that i_e is a purely capacitive current, whereas i_m contains a coupling to the equivalent of the mechanical oscillation velocity of the resonator. Hence the losses of the resonator are covered to the motional current and damping equivalent resistor. The power dissipation appearing through the input impedance of the source-follower,
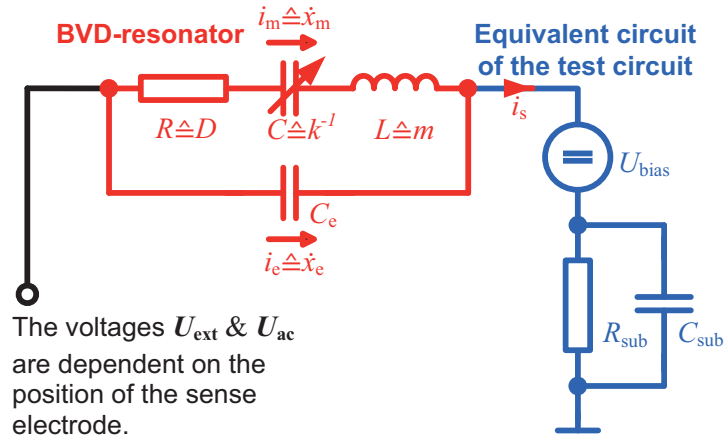
Figure 3.3: Equivalent schematic of the mechanical oscillating system modeled as a Butterworth Van-Dyke (BVD)-resonator for one sensing electrode.

$$P_{i_\mathrm{m}} = \left(\frac{\varepsilon A}{d^2} U_\mathrm{p}\right)^2 \cdot \underbrace{\left(\frac{1}{1 + \frac{R_\mathrm{sub}}{X_{C_\mathrm{sub}}}}\right)^2 \cdot R_\mathrm{sub} \cdot \dot{x}}_{F_{i_\mathrm{m}} = D_\mathrm{e} \cdot \dot{x}} \cdot \frac{\partial x}{\partial t} \tag{3.8}$$

contains a characteristic electrostatic damping coefficient D_e. In consequence of a harmonic approach, the electrostatic damping coefficient for a sensing electrode is

$$D_e = (\frac{\varepsilon A}{d^2} U_p)^2 \cdot \frac{R_{sub}}{1 + (R_{sub}\omega C_{sub})^2} \qquad (3.9)$$

which is an additional damping mechanism beside intrinsic and extrinsic effects [122]. Hence the electrostatic response to the dynamic behavior of the resonator is specified by the damping force $D_e\dot{x}$, neglecting the influence of internal friction or possible support loss. The solution of Eq. (3.1) with a harmonic approach leads to

$$\hat{x} = \frac{\hat{F}}{k_{tot} + j\omega D_{tot} - m\omega^2} \qquad (3.10)$$

where k_{tot} and D_{tot} implies the sum of overall mechanic and electrostatic stiffnesses and damping coefficients, respectively. Hence the analytical equivalent to the signal of a laser Doppler-vibrometer is

$$\hat{v} = \frac{j\omega \hat{F}}{k_{tot} + j\omega D_{tot} - m\omega^2} \, , \qquad (3.11)$$

the peak velocity of the resonator.

Two Port Configuration

So far only a single electrode configuration was taken into account. As a result, only sysmmetric modes can be detected. The possibilities of the sensor can consequently be improved with two electrodes depicted in Fig. 3.4, but requires a deeper understanding of the electromechanical system.

In the case of two sensing electrodes the treatment is a bit sophisticated, although any stray fields have been neglected in the analytic derivation. The equation of motion becomes

$$m\ddot{x} + D\dot{x} + (k_m - k_{e1} - k_{e2})x = \frac{\varepsilon A}{d^2}(U_{p1}u_{s1} + U_{p2}u_{s2}) + F_L \, , \qquad (3.12)$$

where $U_{p1,2} = (U_{ext} - U_{bias1,2})$. The potentials U_{bias1} and U_{bias2} are a result of slightly different electrical bias potentials of the independently sensing electronic assemblies connected to the two sensing electrodes (see Fig. 3.5).

In the case of negligible mechanic damping mechanisms and negligible magnetic forces F_L, and balanced applied forces, $U_{p1}u_{s1} + U_{p2}u_{s2} \equiv 0$, where after a short auxiliary transformation U_{ext} becomes

$$U_{ext} = \frac{U_{bias1}u_{s1} + U_{bias2}u_{s2}}{u_{s1} + u_{s2}} \qquad (3.13)$$
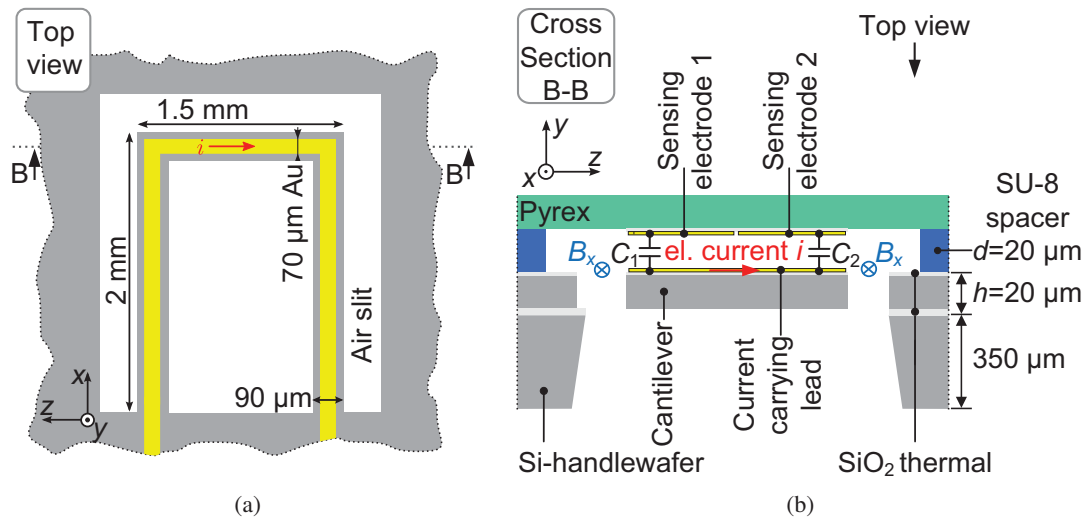
Figure 3.4: 3.4(a) Enlarged schematic top view of the U-shaped cantilever and 3.4(b) schematic cross section of the test device at the tip of the cantilever.
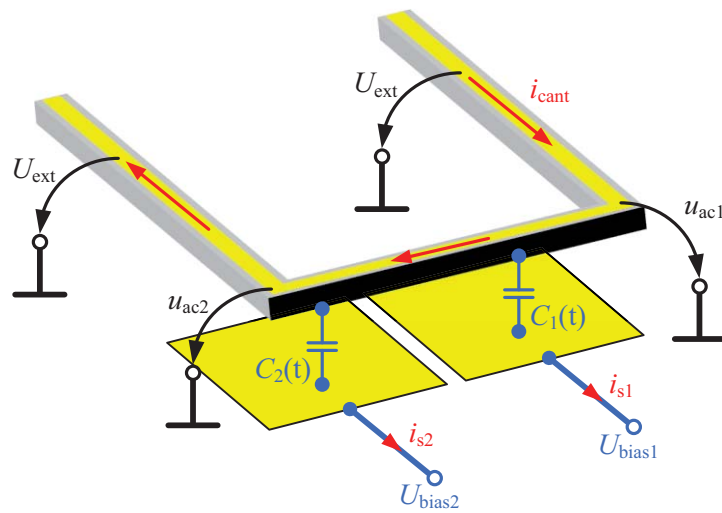
Figure 3.5: Simplified electric scheme of the resonator with it's capacitive read-out system of two sensing electrodes.

a mixing potential dominated by the two bias voltages. According to the equivalence of the capacitive read-out of one sensing electrode with a voltage divider schematically shown in Fig. 3.6, the alternating voltage becomes
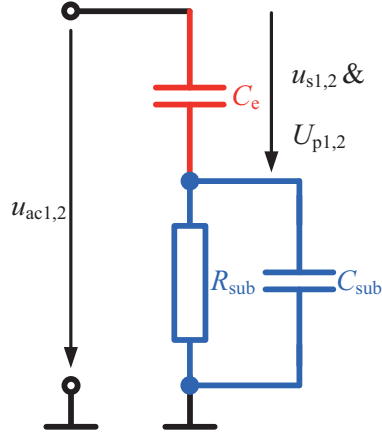
Figure 3.6: The voltage divider as a appropriated model for the electric signal through sensing electrode.

$$u_{\text{s}1,2} = \frac{1 + j\omega R_{\text{sub}}C_{\text{sub}}}{1 + j\omega R_{\text{sub}}(C_{\text{sub}} + C_{\text{e}})} u_{\text{ac}1,2} \; . \tag{3.14}$$

Owing to Fig. 3.6 the sensing current $i_{\text{s}1,2}(t)$ through the voltage divider generates the sensing voltage

$$U_{\text{s}1,2} = \frac{i_{1,2}(t)}{\frac{1}{R_{\text{sub}}} + j\omega C_{\text{sub}}} \tag{3.15}$$

at the first gate of the capacitive read-out system. The sensing current is a result of Eq. (3.3),

$$i_{\text{s}1,2} = \underbrace{\frac{\varepsilon A}{d^2} \hat{v} U_{\text{p}1,2}}_{i_{\text{m}}} + \underbrace{\frac{1 + j\omega R_{\text{sub}}C_{\text{sub}}}{1 + j\omega R_{\text{sub}}(C_{\text{sub}} + C_{\text{e}})} \cdot j\omega C_{\text{e}} u_{\text{ac}1,2}}_{i_{\text{e}}} \tag{3.16}$$

in the limit of small signal analysis.

Part III

End

<div style="text-align: right;">

CHAPTER 4

</div>

Experiments and Results

4.1   Device Fabrication

The fabrication process for the device is based on the silicon-on-insulator (SOI) technology, where two monocrystalline silica layers are separeted by a thin layer of silicon dixoxide (SiO_2). Compared to the use of simple silicon wafers this technology offers a defined etch stop due to the large selectivity of the etching chemical between silicon (Si) and silicon dioxide. The thickness of the device layer and the handle layer were $20\,\mu m$ and $350\,\mu m$, where the surfaces of the SOI wafer are passivated with silicon dioxide. The wafer was bought with a passivation of SiO_2, where coating of the device layer is completely removed by a plasma etching process.

   Several physical and chemical processes are needed to produce the test devices. Fig. 4.1 depicts the sequence of these processes:

1. After the passivation, the lithography for the metal layer is performed. Metal lines are evaporated and patterned with lift-off technique using an image reversal photoresist (AZ 5214), where the metal is removed except for areas where the metal is in a direct contact with the silicon. Both the current-carrying leads and the bond pads consist of a $300\,nm$ thick gold layer and a $70\,nm$ chromium layer acting as bonding adhesion to the waver surface. The intrinsic mechanical stresses in the chromium and in the gold layer almost compensate each other. Therefore, the structure remains nearly undeflected. This is essential for the proper function of the capacitive readout. The lead has a width of $70\,\mu m$.

2. Then flat $300\,nm$ deep trenches for the expansion of the epoxy-based negative photoresist (SU-8) are etched with a DRIE (Deep Reactive Ion Etching) process.

3. The device layer is etched from the top side towards the openings for the bonding process and partially covered with a protective layer.

4. A lithography of the handle wafer will define the backside openings of the test structure. The passivation in those openings is removed by DRIE (Deep Reactive Ion Etching)

<div style="text-align: right;">

85

</div>
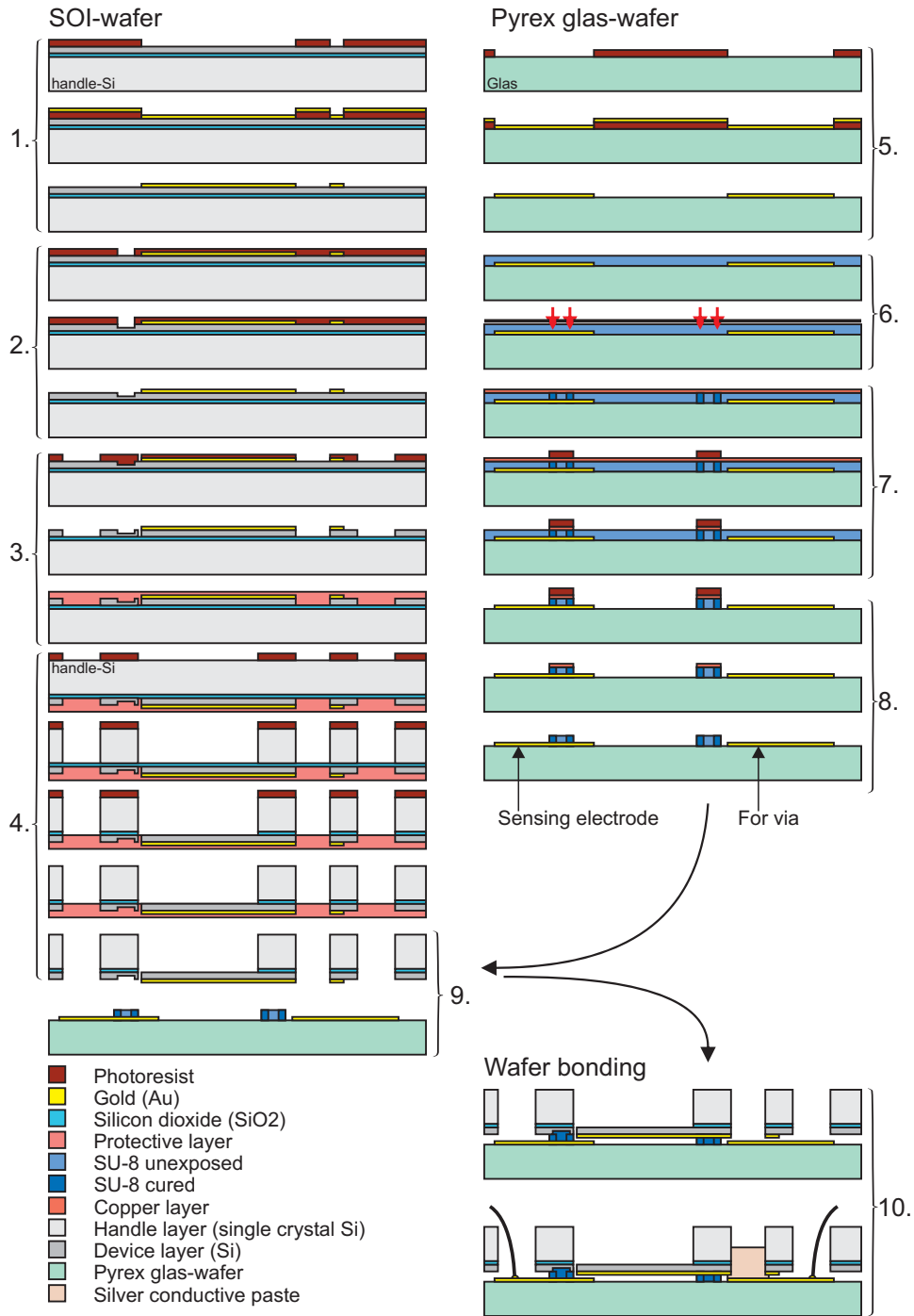
Figure 4.1: Schematic of the fabrication process. The sequence of these processes steps are explained in the text, whereas the numbering of the corresponding schematics is identical with the paragraphs.

process. Afterwards, the silicon wafer is etched anisotropically from the back side with 30 wt % KOH (potassium hydroxide) solution at 75 °C. A thin SiO_2 membrane, the insulation between device layer and handle wafer remains. Afterwards, this membrane is dry etched using a DRIE process from the top, which finally releases the cantilever.

5. The counterpart of the free vibrating planar structure, i.e. the sensing electrodes is fabricated on a Pyrex glass-wafer. The lithography for the metal layer of the electrodes is similiar to the silicon-wafer. However, titanium was used instead of chromium as bonding agent.

6. Afterwards, a SU-8 layer is applied on the Pyrex glass-wafer, where a suitable mask allows to expose two nested frames around the opposite openings of the silicon wafer to UV radiation.

7. With a sacrificial Cu (copper) thin film the SU-8 can be removed. Only the cured frames and the unexposed SU-8 between the frames remain after exposure.

8. A custom SU-8 bonding process on wafer level creates a 20 µm high spacer, which is equal to the equilibrium distance d of the sensing electrodes compared to the vibrating structure.

9. The two wafers are mounted on top of each other.

10. The device was investigated in upside down orientation in order to enable an optical access to the free vibrating cantilever additionally to the capacitive read-out. An electrical contact between the two wafers is performed with a silver conductive paste.

The wafer is coated with a protection layer, where after wafer dicing the test devices are die-bonded on printed circuit boards (PCB). The electrical connections from the chip to the PCB are performed by gold wire-bonding, where the wire bonds can be protected by a two-part epoxy resin. The geometrical parameters of the test device are summarized in Fig. 4.2, wherein the height of the bar has been experimentally verified, which is depicted in Fig. 4.3.
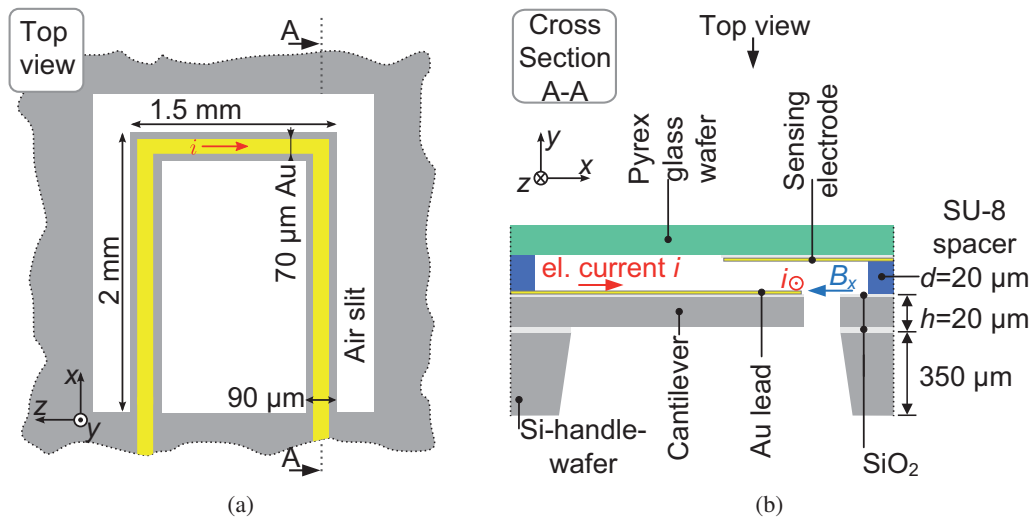
Figure 4.2: (a) Geometric dimensions of the U-shaped cantilever and (b) schematic cross section of the test device.
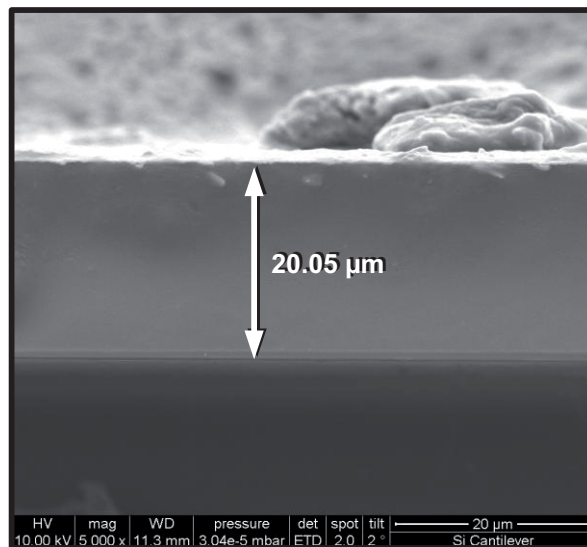
Figure 4.3: Scanning electron micrograph of the fabricated cantilever. The dimension arrow indicactes the height h of the cantilever.

4.2 Experimental Setup

The test device is placed in a vacuum chamber to minimize extrinisic damping mechanisms like gas damping. The chamber in Fig. 4.4 is surrounded by a pair of coils, configured as Helmholtz coil. This configuration provides a homogeneous magnetic field around the device. The Helmholtz coil generates either a static or alternating magnetic field.
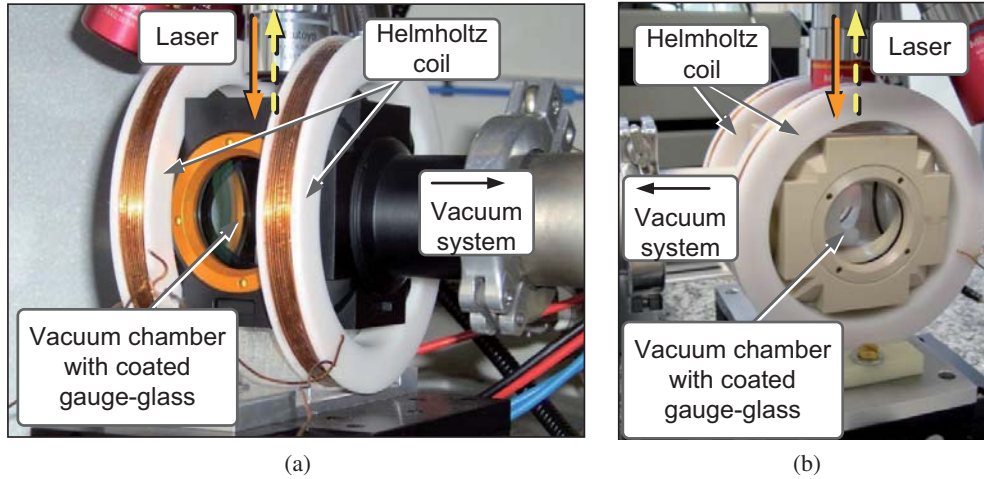
Figure 4.4: (a) Vacuum chamber made of aluminum and (b) made of PEEK, both attached with the Helmholtz coil.

Both designs of the vacuum chamber have been made by the same pattern and offer an optical access through four glass windows. In order to use the vacuum chamber for AC-measurements, the vacuum chamber of Fig. 4.4(b) is made of electrically insulating PEEK (Polyetheretherketon). Additionally, the vacuum system is also connected to a nitrogen gas line. The nitrogen pressure in the vacuum-chamber is measured with a high vacuum gauge (Pfeiffer IMR 265) and maintained by a flow controller (MKS 50 sccm) at the high vacuum port of a turbomolecular pump, enabling a dynamic equilibrium in the pressure range of 20 mPa to 200 Pa. As a result a fully automated control of the nitrogen atmosphere is established for interactions with the vibrating test structure. The homogeneity of the Helmholtz coil configuration was tested with a search coil (point coil PKS 5, Magnet-Physik Dr. Steingroever GmbH), shown in Fig. 4.5.

The inductivity of the Helmholtz coil is 3.49 mH, measured at a frequency of 120 Hz (Agilent LCR-Meter), whereas the resistance of the configuration is 5.71 Ω. Three linear stages (micos, PLS-85) controlled by a PC, move the search coil along the axial principle axis of the Helmholtz coil configuration. Fig. 4.6 depicts a typical data set.

During operation under vacuum conditions, there are two possible configurations of the Helmholtz coil, as seen in Fig. 4.4. Regarding to the orientation of the device in respect to the external magnetic field, two different vibration modes will be favored, namely the symmetric and the antisymmetric modes (see Fig. 4.7). In this section it is assumed that the magnetic field

(a)   (b)
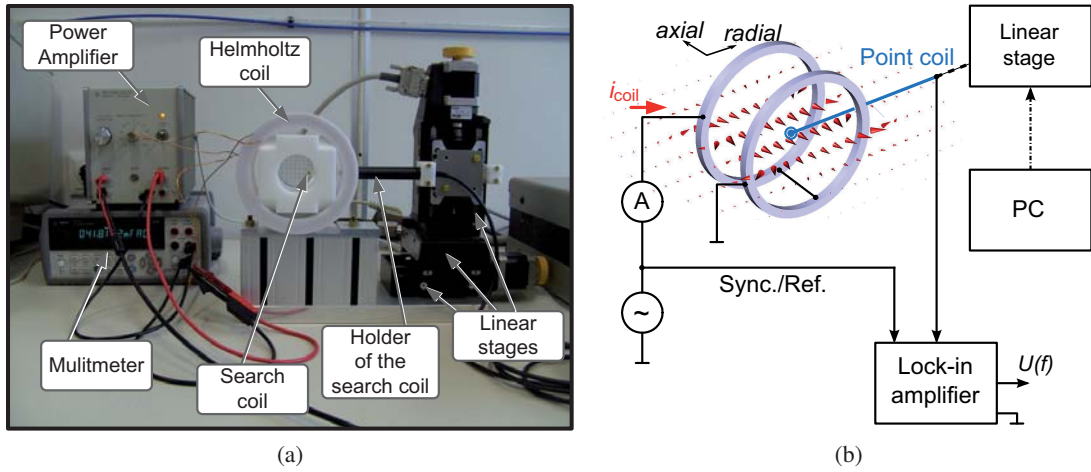
Figure 4.5: (a) Measurement setup to test the magnetic flux inside the Helmholtz coil configuration. (b) Schematic setup for the characterization of the Helmholtz coil configuration.
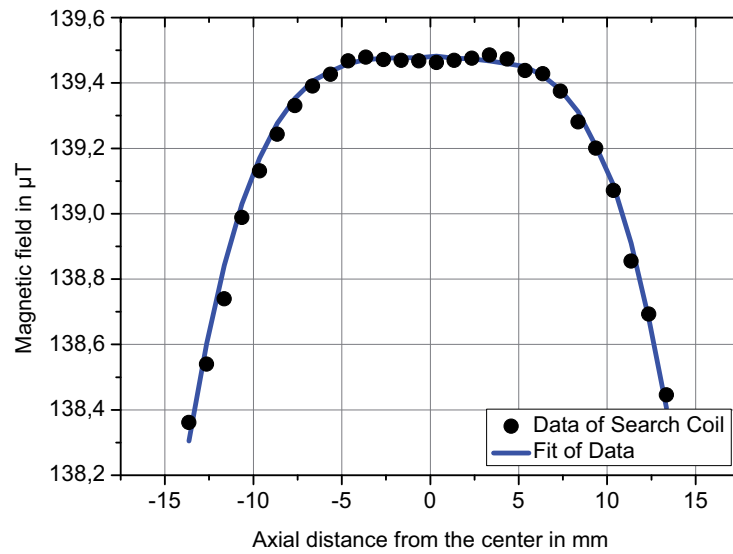
Figure 4.6: Homogeneity of the Helmholtz coil field along the axis, tested with a sinusoidal magnetic field, where i_{coil}=100 mA and f=256 Hz.

is homogeneous, due to the Helmholtz-coil and that only components in the x- or z-direction exist. Therefore, field distributions do not need to be considered.

(a)   (b)
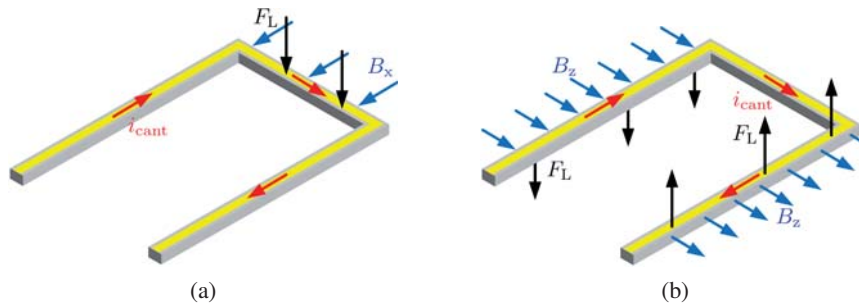
Figure 4.7: Schematic views of different vibration mode shapes. (a) Depicts the symmetric excitation mode and (b) the antisymmetric excitation mode in dependence of the acting Lorentz force.

Thus, the pronounced excitation of two different vibration modes (S1 and AS1) is possible (see Fig. 4.8).

(a)   (b)
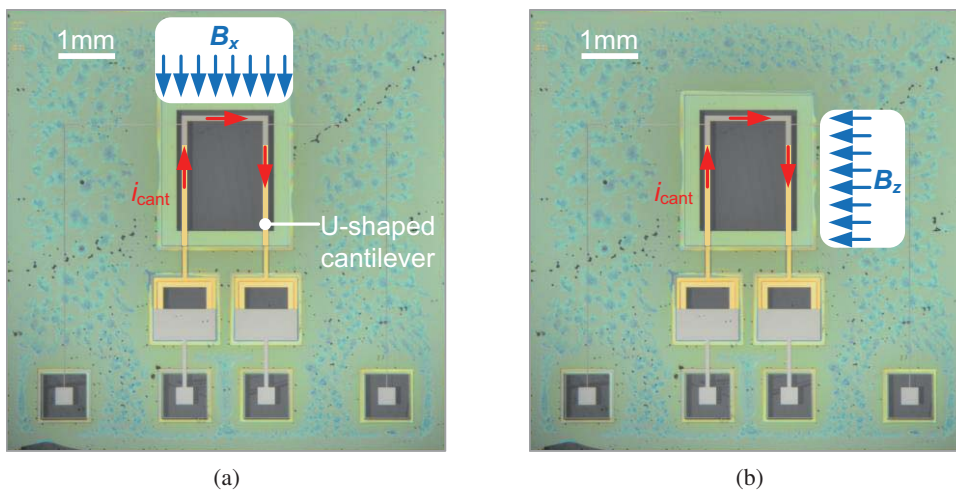
Figure 4.8: Micrograph of the MEMS structure for magnetic field detection. The small blures are a result of the SU-8 bonding process. (a) Magnetic field orientations for the excitation of the first symmetric (S1) and (b) a possible orientation to excite the antisymmetric mode (AS1) of the cantilever.

Two different measurement principles were taken into account to characterize the out-of-plane vibrations of the cantilever structure: Firstly, a scanning laser Doppler-vibrometer (Polytec MSA400 Micromotion Analyzer) with displacement and velocity decoders, and secondly, a custom-built capacitive read-out system. Laser Doppler-vibrometry (LDV) is a non-contact velocity and displacement measurement technique, where the most important component is a laser

beam focused on the tested structure. The oscillations of the device causes the Doppler effect in the laser reflection. In the case of a proper reflection of the incident laser beam, it is possible to calculate its displacement and velocity. Therefore, an optical interferometer is used to mix the backscattered light coherently with the reference beam, where the intensity of the mixed light is measured with a photodiode. Usually, a frequency shift is generated by a Bragg cell, or acousto-optic modulator into reference beam. As a consequence, the output of the photodetector is a frequency modulated signal, where the Bragg cell frequency is the carrier frequency and the Doppler shift is the modulation frequency. Therefrom, the signal can be demodulated to derive the velocity in the time domain of the oscillating test structure. The output signal of a Laser Doppler-vibrometer is a continuous analog voltage that is directly proportional to the vibration velocity of the vibrating surface. Because of the considerable broadband noise of the velocity decoder, the vibrometer's output signal is measured with a lock-in amplifier (Stanford Research Instruments SR830). The output signal can also be analyzed with a spectrum analyzer that deliver without an additional effort the mechanical spectrum of the oscillation, but with the loss of accuracy.

A programmable waveform generator excites the sinusoidal current through the lead, which allows spectroscopy of the mechanical structure oscillations. The vibrometer's digital signal processor (DSP) and the Lock-in amplifier are synchronized at the fundamental frequency to measure the vibrometer's output signal. Because of the high intrinsic quality factor of $1 \cdot 10^4$ at an ambient pressure of $0.2\,\mathrm{Pa}$, the cantilever vibration may take several seconds to settle.

In the case of electrostatic sensing, depicted in Fig. 3.2, the cantilever is set to a polarization voltage U_{ext} to provide the bias for the capacitive detection. The sinusoidal current through the lead is driven by an ac voltage u_{ac}, which combines with the voltage U_{ext} and finally forms the driving force of the cantilever ($u_{\mathrm{s}} \ll U_{\mathrm{p}}$).

Therefore, the ac voltage at the sense electrodes u_{s} is generated by the vibration of the cantilever. A sophisticated kind of source follower, which is capable of measuring changes in the capacitance at frequencies up to 1 MHz, is used as amplifier to sense the cantilever vibrations. To ensure linearity of the electro-mechanical system, the amplitude of the cantilever vibration due to the Lorentz-forced excitation is always much smaller than its thickness h and the equilibrium distance d between the vibrating cantilever and the sensing electrodes.

4.3 Stability and Noise Sources

Stability of Driven Damped Cantilevers

The problems caused by noise are well known: First a degradation of performance is observed and second the deterioration of the output at the lower limit of the sensors or measurement systems results [123]. Because of the miniaturization, the interaction of noise (energy) with typical masses much less than a few µg can cause disturbance that will affect the performance of the M/NEMS device [124]. The main influences affecting the stability of a resonator can be categorized as follows, according to the publication of Walls et al. in 1995 [125]:

- temperature (both static and dynamic frequency vs. temperature; warmup and thermal shock)

- acceleration (gravity, shock, acoustic noise, vibration effects) [126]

- temporal changes (short-term - phase noise, intermediate-term - environmental temperature fluctuations, and long-term stability - aging)

- electromagnetic fields, electronic switching power supply, load impedance in case of electromechanical interaction

- atmospheric pressure (altitude, air pressure fluctuations), humidity

Some of these interferences are easily determined by experiments but others are difficult to quantify [127]. Cleland and Roukes presented in 2002 a self-contained formalism for describing the resonance and noise properties of micro- and nanomechanical resonators, based on the Euler–Bernoulli beam bending theory [128]. With respect to phenomena of short-term stability, the resonator will be limited by certain stochastic processes. These fundamental phenomena comprises the thermomechanical noise generated by internal loss mechanisms in the resonator, Nyquist–Johnson noise from the readout system, and adsorption–desorption noise from ambient gas molecules around the resonator [125, 129–132]. It is worth mentioning that there is another noise source due to temperature fluctuations caused by the finite thermal conductance of the resonator [132]. These fluctuations are fundamental to any object (with finite heat capacity) and have to be distinguished from environmental thermal drifts that can be monitored using a temperature controlled chamber. Other physical limitations can be caused by particular transducer implementations. For example, electrostatically detected (and driven) resonators suffer from surface charge accumulation.

In this work the magnetic field sensor operates in a resonant condition (see Fig. 4.9), at low ambient pressure to reduce extrinsic damping mechanisms like gas damping and to get close to the cantilever's fundamental frequency [39]. Therefore, **vibration of the chip fixture**, caused, e.g. by the turbomolecular pump of the vacuum system, will contribute significant acoustic noise. Another important cause of noise will result from **short-term changes of the magnetic field** inside the Helmholtz coil, e.g. because of low frequency field fluctuations caused by nearby subway DC supply lines, as well as magnetic noise produced by power lines. The third important influence on the stability and drift of the MEMS magnetic field sensor will arise due
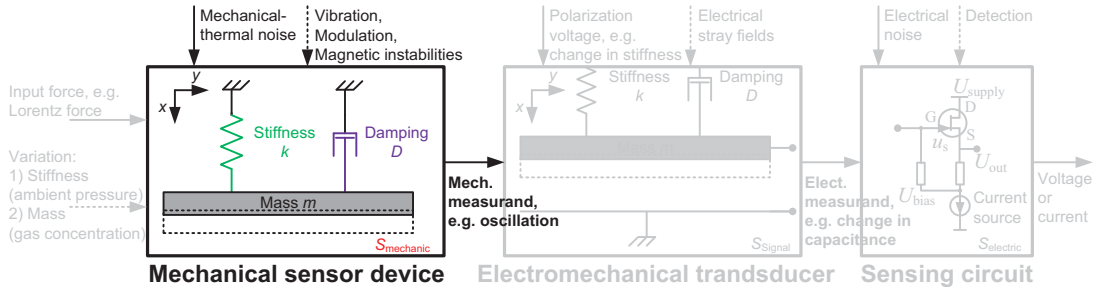
Figure 4.9: Classification of a microelectromechanical system in mechanical sensor device, where emphasis is laid on the stability and noise of the resonator.

to **thermal expansion** leading to lateral drift of the tip relative to the sense electrode and shifting the resonance frequency. All three sources will mainly affect and deteriorate the sensitivity of the sensor and decrease its linearity and accuracy.

Interfering Mechanical Vibrations

One of the first theoretical considerations on noise in microsystems was published by Gabrielson in 1993 [129]. He discussed various effects of mechanical–thermal noise for MEMS, where he reviewed several techniques for calculating the mechanical–thermal noise in simple MEMS structures, such as a mass-spring accelerometer. In an analog to the Johnson noise of electrical resistances, the Nyquist's relation gives the spectral density of the fluctuating force related to the mechancial resistance of the device. According to this paper the noise is at any frequency $\omega \ll \omega_0$

$$P_{\text{noise}} = 4k_B T \frac{\Delta f \omega_0}{mQ} , \tag{4.1}$$

where k_B is the Boltzmann constant, T is the ambient temperature, Δf is the measurement bandwidth, ω_0 is the natural frequency, m is the oscillatory mass and Q is the quality factor of the device. Equation (4.1) indicates that the SNR can practically be improved by increasing the quality factor Q, reducing the natural frequency ω_0, or increasing the mass m of the 1-DOF. The latter also lowers the natural frequency of the system.

Increasing the mass of the system is usually contradictory to the miniaturization of the system. Lowering the natural frequency of the system, as far to be within the band of expected signals can cause a nonlinear phase into the system response. In the end, one can increase the quality factor Q, always be aware that out-of-band amplitudes in nonlinear systems will also be magnified (with the magnification factor Q). Additionally, the mechanical system must be able to handle these large movements to guarantee a large dynamic range. Furthermore, the vibrations of a mechanical system with high Q may take several seconds to settle. Assuming that thermo-mechanical noise is a fundamental limit of the noise level for this device, the accelerometer resolution within a bandwidth of 1Hz is given by

$$\langle a \rangle \approx \sqrt{\frac{4k_B T \omega_0}{mQ}} \, . \tag{4.2}$$

Externally induced vibrations of the MEMS chip, like acoustic couplings due to the turbo-molecular pump essentially determined the noise floor during the device characterization at low ambient pressures. They add an acceleration related signal to the elelctromagnetically generated vibration. However, if a resonator is excited externally, the time dependent acceleration can change the oscillation of the device, too. Even in the simple case of a harmonic chip acceleration with the frequency f_1, the frequency will be modulated at the rate of f_1 [126]. For a small modulations resonator motion, a sinusoidal vibration produces spectral lines at $\pm f_1$ (=vibration frequency) from the natural frequency f_0. Most of the energy is in the fundamental frequency f_0, but a small amount is in the first spectral line pair, where the higher order spectral lines are negligible in case of weak nonlinearity of the system. In the case of a random vibration, a massive increase of the phase noise can occur. Another vibration effect results from acoustic sounds, where this kind of vibration can produce significant oscillations similar to that produced by mechanically transmitted vibrations. In contrast to mechanical vibrations of the ambient, pressure fluctuations of the acoustical noise directly hit the mechanical resonator. The (broad-band) response of the MEMS structure extends towards low frequencies due to the different mechanical transmission process. The acoustic noise modulates the oscillation, where the modulation depends on the vibration amplitudes, their directions and their frequencies.

Experimental Analysis of the Influence of External Vibrations: A scanning laser Doppler-vibrometer (Polytec MSA400 Microsystem Analyzer, shown in Fig. 4.10) comprising displacement and velocity decoders is used to characterize the out-of-plane vibrations of the cantilever structures. The vibrometer output signal is measured with a spectrum analyzer (Stanford, SR780), schematically shown in Fig. 4.11).

A waveform generator excites the vibrating structure around its natural frequency (S1) or at higher harmonic modes (AS1 or S2) in a static magnetic field. The waveform generator provides the sinusoidal current in the lead on the top of the cantilever. This causes a harmonic oscillation due to the Lorentz force. Owing to high intrinsic quality factors in vacuum, the cantilever vibration may take several seconds to settle (Fig. 4.4).

The measurements in Fig. 4.12 were done with minimal exciting current $i_{cant} = 6.19 \, \mu A$ at resonance $f_{r0} = 4.359 \, kHz$. The device is a U-shaped cantilever with capacitive read-out, where deflection data were both taken by the vibrometer at the middle of the tip on the U-frame and on the chip carrier (see red dots points 1) & 2) in Fig. 4.11). Fig. 4.12 depicts the frequency spectra of the chip carrier vibrations (black line) and the cantilever movement (red line) during excitation of the device. At the lower bound of the frequency spectrum, the response to turbomolecular pump vibrations dominates.

These vibrations can be attributed to the turbomolecular pump switching off the pump and observing the frequency decay of the respective lines of the spectrum. The spectra in Fig. 4.13, 4.14 and 4.15 only differ in the operation of the turbomolecular pump, while the backing pump is running. In the case of the black spectra the turbomolecular pump operates at its maximum
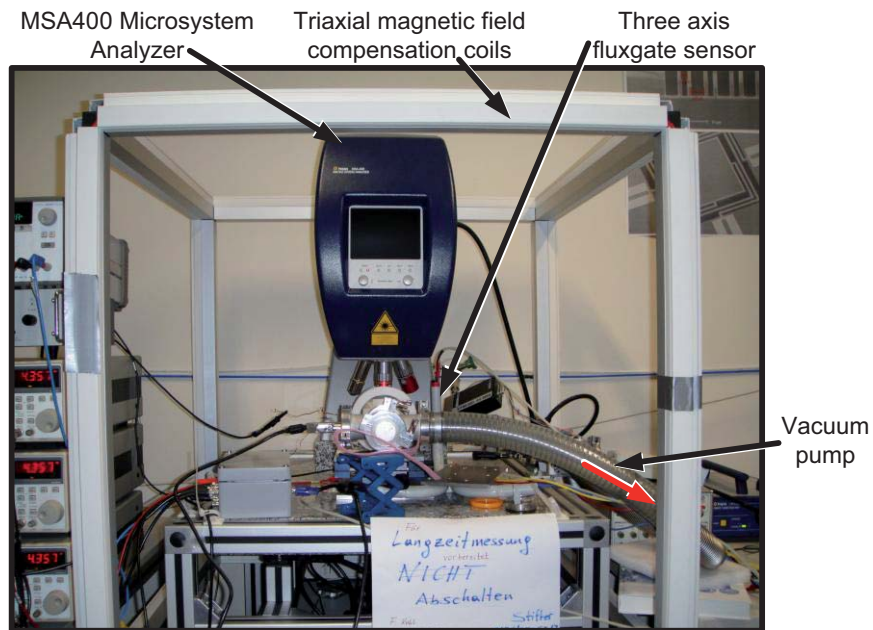
Figure 4.10: Schematic setup for the characterization of the influence of the noise due to external vibrations on the vibration of different mode shapes.
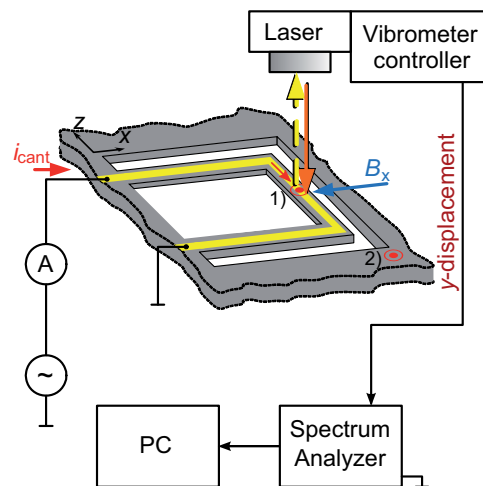

Figure 4.11: The optical measurement setup, where the red dots depicted in the figure denotes the measurement points of the incident laser beam on the cantilever (1) and the chip frame (2).
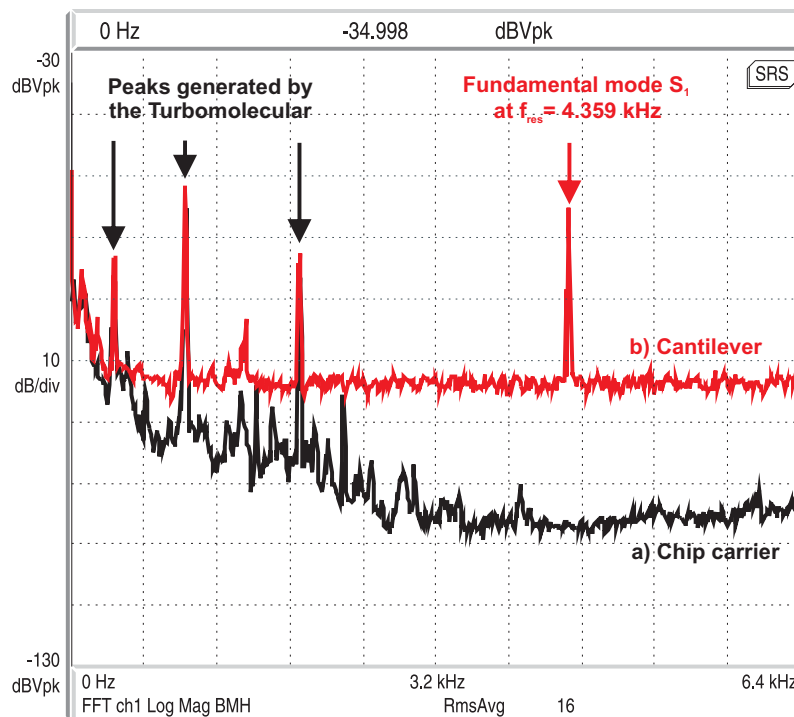
Figure 4.12: Measured vibration spectra (arbitrary units) of (a) the chip carrier (black line) and (b) the test structure (red line) at resonance. The cantilever current amounts 6.19 μA and the related ambient magnetic field component is 48 μT, without compensation of any magnetic disturbances.

rotational speed approximately 60,000 rpm, while the red data was taken with a running down pump (but with sufficiently low gas damping). By switching on and off the turbomolecular pump it is possible to determine the quality of the disturbances. If they are purely electrical they should disappear immediately after shutdown the pump. But in the experiment, the frequencies of the disturbances varied according to the rotational speed of the down-running turbomolecular pump. Furthermore, it was found experimentally that switching off the backing pump has no effect on the noise.

Fig. 4.13 and 4.14 indicate that the vibration noise of the pump dominates for resonance frequencies between 4 to 12 kHz, while Fig. 4.15 shows a moderate modulation effect of the pump on the second symmetric mode (S_2) of the cantilever. As a result, S_2, was taken for very sensitive magnetic field measurements.

Summing up, the acoustical interferences have a severe influence on the oscillations of the test device, wherein the performance and the detection limit of the sensor is determined by the interfering signals related to the turbomolecular pump. With Eq. (4.2) the calculated thermal noise for the device under test (DUT) with a Quality factor Q of $1 \cdot 10^4$ in vacuum would be around $0.1 \, \mu g_{earth}/\sqrt{Hz}$ [38]. Experimentally, the noise floor measurements were taken at specific resonant modes (S_1, AS_1 and S_2) by laser Doppler vibrometry over a time period of 280 seconds.
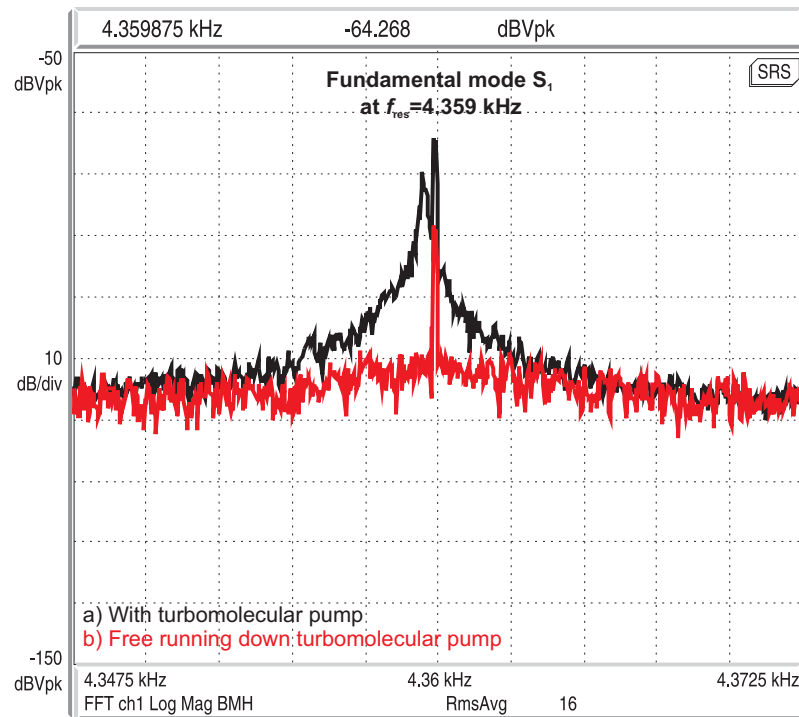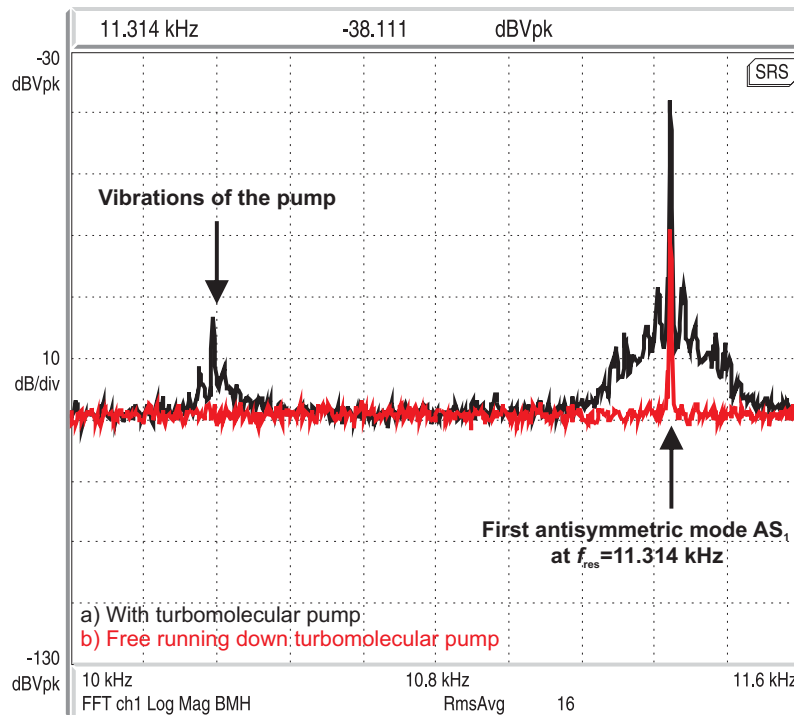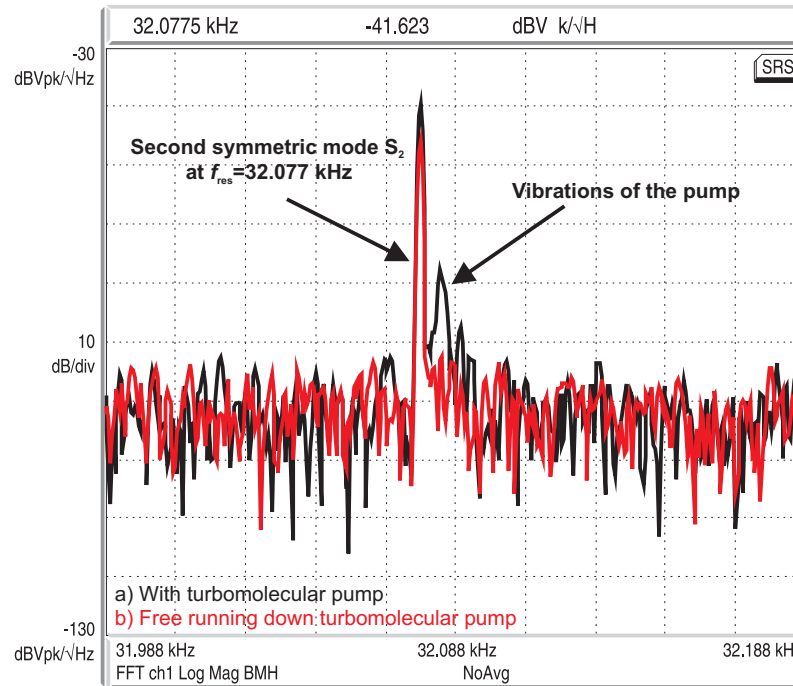
Figure 4.13: Frequency response of the test structure around the first symmetric mode S_1, with the turbomolecular pump switched a) on and b) off, but free running down with $i_{cant} = 6.19\,\mu A$ and 48 μT.

The measurement points were choosen by their maximum vibration deflection at an electric current in the lead of 6.19 μA. During the measurement, the custom automated magnetic field compensation system was switched on. With the help of Lock-in measurement technique, it was possible to determine the noise level for every vibration mode during vacuum operation of the turbomolecular pump (see Fig. 4.17). Multiplying these amplitude related data with the square of the specific angular resonance frequency, it was possible to obtain equivalent acceleration noise values. Hence, for the first symmetric (S_1) mode the measured values were typically in the range of 1 $mg_{earth}/\sqrt{Hz}$, whereas for the first antisymmetric mode (AS_1) it is approximately 0.25 $mg_{earth}/\sqrt{Hz}$ and for the second symmetric mode (S_2) around 50 $\mu g_{earth}/\sqrt{Hz}$. Therefrom it is obvious that the superposition of excess system noise deteriorates the resolution of this magnetic field measurement method significantly.

Figure 4.14: Frequency response of the test structure around the antisymmetric mode AS_1, with the turbomolecular pump switched a) on and b) off, but free running down with $i_{\text{cant}} = 561\,\mu A$ and $48\,\mu T$.

Thermal Influences on the Eigenfrequency of Cantilevers

Due to the sensor principle, where a current passes through the lead on the top surface of the cantilever, a certain amount of heat is generated. This can affect the operation of the sensor in various ways. First of all, a stress is developed inside the cantilever. Secondly, the material properties, like the resistivity, the specific heat, the thermal expansion coefficient, the thermal conductivity and especially the Young's modulus, will change with temperature, e.g. the temperature coefficient of the Young's modulus is $-60\,\text{ppm/K}$ [133]. A further source of resonant frequency shifts of MEMS structures results from the thermal expansions of the applied materials. Therefore, the change in the length has also to be considered. In Table 4.1 the most relevant materials are compiled.

Thin metallic films, employed for electrical leads, exhibit large coefficients of thermal expansion and thermal conductivity. Silicon has a comparable large thermal conductivity like metals as gold. Owing to the small cross-section the contribution of the thin metallic leads is negligible compared to the thermal conductance of the silicon beam. However, the silicon beam is able to transport a remarkable amount of heat per cycling period. Thermal influences of clamped-free plates are insignificant, due to the excellent heat conductivity of silicon through the large suspension area of the silicon beam. In order to achieve a high sensitivity to magnetic fields,

Figure 4.15: Frequency response of the test structure around the second symmetric mode S_2, with the turbomolecular pump switched a) on and b) off, but free running down and compensation of magnetic field disturbances with $i_{\mathrm{cant}} = 561\,\mu\mathrm{A}$ and $48\,\mu\mathrm{T}$.

Table 4.1: Typical materials applied in microfabrication and their thermal properties [14].

Material	Thermal conductivity λ in $\mathrm{Wm^{-1}K^{-1}}$	Therm. expansion coeff. α in $10^{-6}\mathrm{K^{-1}}$
Silicon(single-crystalline)	157	2.3
SiO_2	2.1	0.5
Cr	93.9	4.9
Ti	21.9	8.6
Si_3N_4	18	3.0
Au	318	14.2
Al	236	23

U-shaped cantilever with small cross section dimensions are desireable that operate in vacuum and therefore, the relative influence of the thermal conductance increases. In consequence of the increasing temperature the length along the elastic axes of both arms of the U-shaped cantilever get longer as well as the cantilever thickness. According to Eq. (2.32) the total change of the resonant frequency includes the temperature dependence of the density ϱ end the Young's modulus E.

The right hand side (rhs) of equation Eq. (2.32) can be converted into

$$\omega_i = \gamma_i^2 \frac{h}{l^2} \sqrt{\frac{E}{12\rho}} = \gamma_i^2 \sqrt{\frac{bE}{12m} \left(\frac{h}{l}\right)^3}, \tag{4.3}$$

where h is the height, l is the length, b is the width, E is the Young's modulus, m is the mass of the cantilever and γ_i are the eigenvalues. The expansion of Eq. (4.3) with respect to T yields

$$\omega_i (T + \Delta T) = \omega_i \sqrt{(1 + \alpha)(1 + TCE)} \Delta T, \tag{4.4}$$

with the temperature coefficient of Young's modulus $TCE = 1/E \cdot (\partial E/\partial T)$. According to Eq. (2.32) the relative change of the resonance frequency amounts

$$TC\omega_i = \frac{\omega_i (T + \Delta T) - \omega_i (T)}{\omega_i (T) \Delta T} = \sqrt{(1 + \alpha)(1 + TCE)} - 1. \tag{4.5}$$

In view of the small values of α and TCE, a first order Taylor expansion of the rhs of Eq. (4.5) is appropriate which results in

$$TC\omega_i \cong \frac{\alpha}{2} + \frac{TCE}{2}. \tag{4.6}$$

From Table 4.1 $\alpha/2 = +1.15 \, \text{ppm/K}$ is obtained, whereas a review of the literature data on the temperature coefficient of the Young's modulus of silicon at room temperature results in $TCE/2 = -30 \, \text{ppm/K}$. Hence the temperature coefficient of the resonance frequency is mainly determined by the softening of the silicon lattice with increasing temperature.

From experiment one can deduce a dependence of about -10 ppm/K with respect to the calculated temperature difference at the mid plane of the U-shaped cantilever. This is not in contradiction with Eq. (4.6) considering the non-uniform temperature distribution along the cantilever. The excess temperature of the cantilever follows from heat balance considerations. Starting from the symmetry plane of the U-shaped cantilever, the heat flux along the cantilever axis, $Q_H(x)$ grows toward the clamped end from zero according to

$$Q_H = P \frac{x}{l}, \tag{4.7}$$

where x denotes the distance along the cantilever axis and P the averaged dissipated power. Equation (4.7) assumes uniform heat generation along the cantilever of sidelength l and thus ignores the 90°corner effects. For a stable temperature distribution, $Q_H(x)$ must be balanced by heat conduction, i.e.

$$Q_H(x) = -A\lambda \frac{\partial T(x)}{\partial x} = -\frac{l}{R_{\text{th}}} \frac{\partial T(x)}{\partial x}, \tag{4.8}$$

where A is the cross-sectional area through which the heat is flowing and R_{th} is the thermal resistivity. Hence, $\partial T(x)/\partial x = -PxR_{\mathrm{th}}/l^2$ and

$$T\left(x\right) = -\frac{PR_{\mathrm{th}}}{2l^2}\, x^2 + const. \tag{4.9}$$

The boundary condition $T(x = l) = 0$ yields

$$const. = \frac{1}{2}PR_{\mathrm{th}}\,, \tag{4.10}$$

and the average excess temperature along the cantilever is computed from

$$T_{\mathrm{mean}} = \frac{1}{L}\int_0^l T\left(x\right)dx = \frac{1}{3}PR_{\mathrm{th}}\,. \tag{4.11}$$
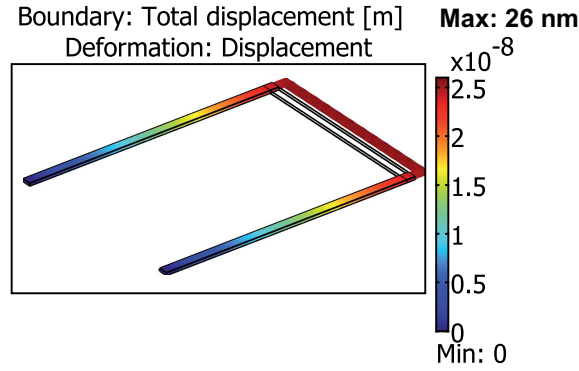
Figure 4.16: The change in length due to an increase of temperature by ΔT=5 K.

In an actual publication, the dependence of the resonance frequency due to the temperature coefficient of the Young's modulus was analyzed [134]. The prediction of the temperature characteristics in this paper for a single-crystal silicon resonator is $-28.7\,\mathrm{ppm/K}$, while their measurements indicate $-20\,\mathrm{ppm/K}$. From Fig. 4.18 the temperature coefficient yields $-27\,\mathrm{ppm/K}$. The uncertainty of the data in Fig. 4.18 especially for small changes in the current has its origin in the experimental method. The mechanical resonance of the cantilever was detected by Laser-Doppler vibrometry, while the frequency was swept with a waveform generator (Fig. 4.17). With each current level the actual resonance frequency was found by decreasing the generator frequency manually. One reason of the deviations from the i_{cant}-parabolic dependence in the small-current regime is due to the small Lorentz-force in the earth magnetic field. One possibility to avoid small deflections is to analyze the frequency response of the cantilever with reduced AC voltage (current) but in a higher ambient magnetic field, like that of a Helmholtz-coil.

Another thermal influence on the length of the cantilever originates from the gold layer of the lead, where a temperature change can induce a mechanical displacement. If the values of
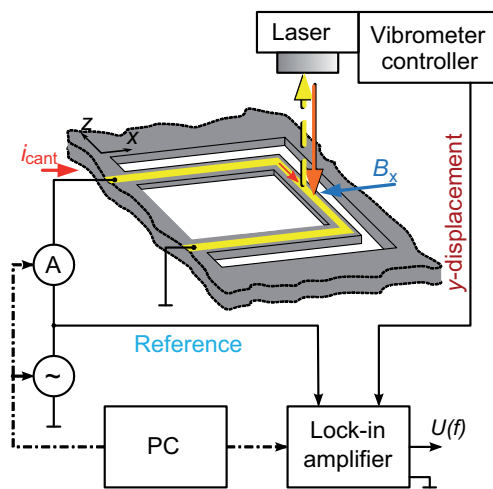
Figure 4.17: Schematic setup for the characterization of the test structure.
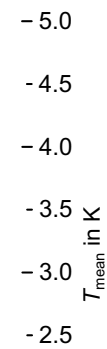
Figure 4.18: Temperature dependence of the natural frequency due to electric heating of a U-shaped Cantilever geometry with a length of 2 mm, a width of one arm of 120 µm and a heigth of 20 µm, $B_{ext} = B_{earth}$.

Poisson's ratio ν differ for the two materials, there will be a change in length [45]. But the curvature of a bimetallic beam depends on the height of both materials. Due to $h_{Au} \ll h_{Si}$ this effect is negligible. Summing up, the temperature-dependent frequency shift for cantilever of this size can be neglected up to excitation currents of 3 mA.

Magnetic Field Instabilities

Besides mechanical vibrations, acoustic disturbances and thermal influences, there are mainly electromagnetic interferences that deteriorate the performance of the resonant magnetic field sensor. The characterization of the sensor depends on the place of the measurement setup. With an appropriate magnetic field compensation system this spatially dependent disturbances can be reduced for a MEMS environment. For the design of the compensation coil system, several magnetic field measurements in the laboratory using a fluxgate sensor from Stefan Mayer Instruments[1] were performed. The triaxial fluxgate sensor FLC3-70 offers a measurement range of $\pm 200\,\mu T$, from DC to 1 kHz with an accuracy down to the nanotesla level (see Fig. 4.19). This sensor has always been applied, whenn the sensitivity and stability of, e.g. Hall sensors was too low or for measurements of disturbances in the range of a few nT close to the test device.

(a)   (b)
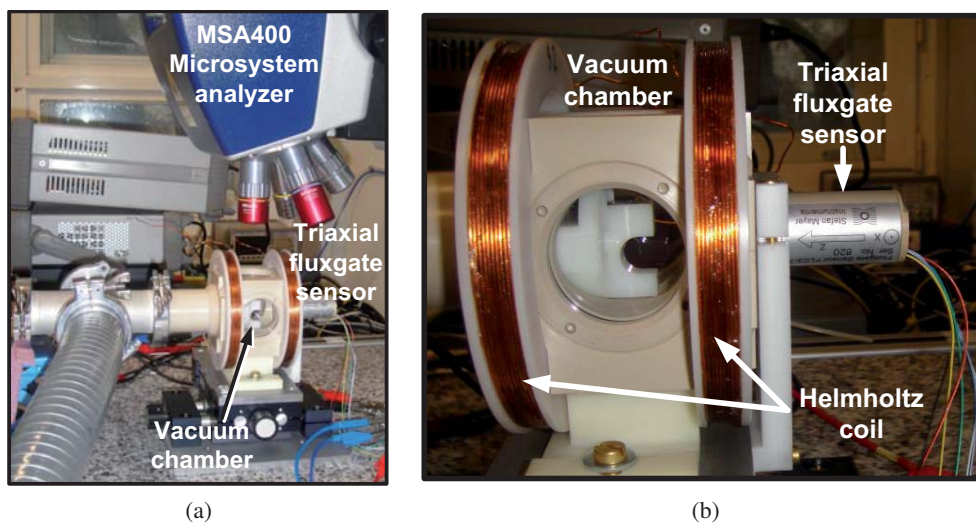
Figure 4.19: Long-term measurement setup for ambient magnetic fields with a triaxial fluxgate sensor close to the test structure.

Fig. 4.20 shows the scatter of the magnitude of the magnetic flux density in all three directions in space, where the sensor was oriented parallel to the maximum value of $\vec{B}_{earth}$. Firstly, the absolute value for each measured data was computed and secondly these values were averaged over a period of half a minute. Similarly, the standard deviation of the magnitude is depicted in Fig. 4.21, which is representative of the average disturbance close to the test device.

The 30 second-averaged magnitudes scatter over a time period of more than 16 hours in the range from 70 nT up to 700 nT. In a sharply defined time interval from 00:36 until 05:20 AM the scatter decreases down to 20 nT to 40 nT, where the time period corresponds with the nighttime break of subway operation during working week.

Due to the measurement result depicted in Fig. 4.21, the assumption that most of the magnetic disturbances originate from the subway seems reasonable. In a rough estimation the mag-

---

[1]www.stefan-mayer.com
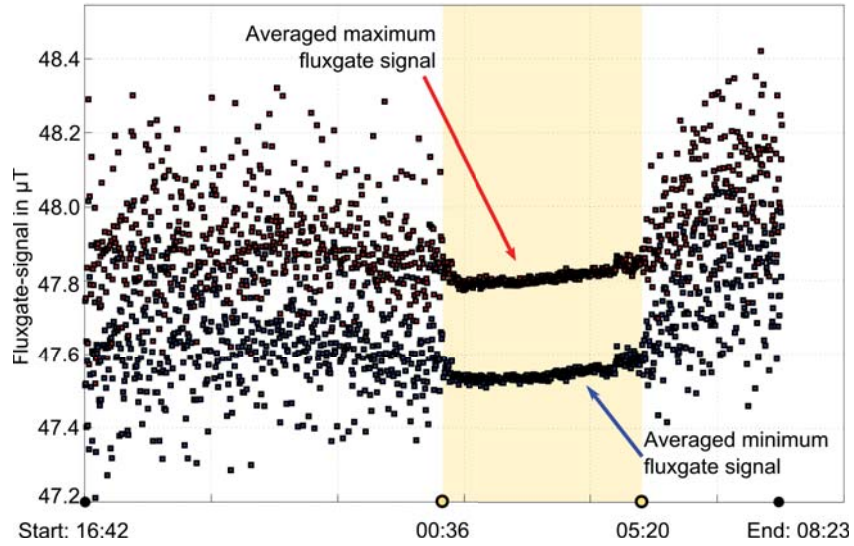
Figure 4.20: The shaded area indicates the period without subway traffic.
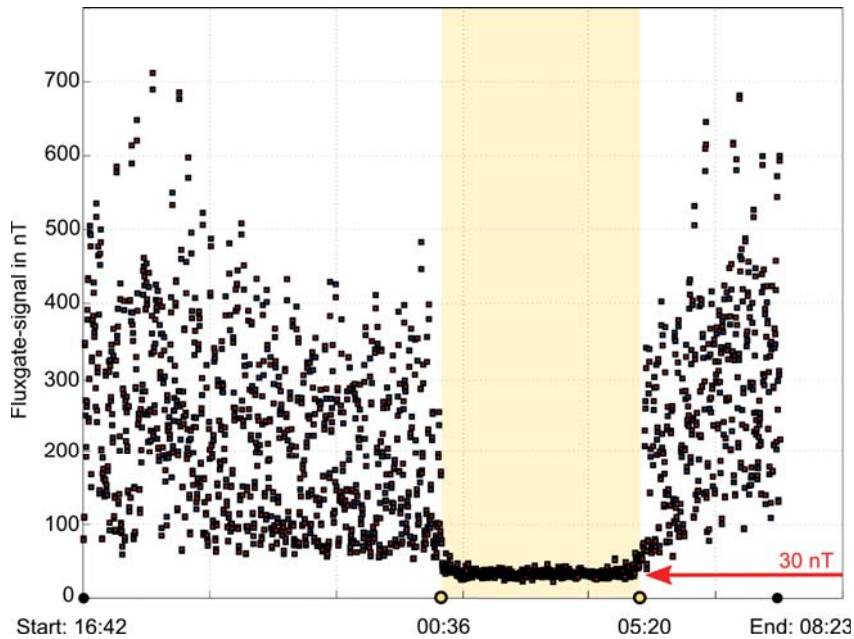
Figure 4.21: Standard deviation of the averaged fluxgate-signal (absolute value) over a time period of more than 16 hours. The averaged maximum values comprises 700 nT.

netic field can be calculated by the relationship $H = I/l$ of a long straight current-carrying conductor. The subway is located approximately 100 m near the laboratory, where typical electrical parameters of the subway are a 750 V supply voltage at a maximum power of 1 MW. This leads to a current of around 1 kA with a magnetic flux density of approximately 2 μT at the specified distance.
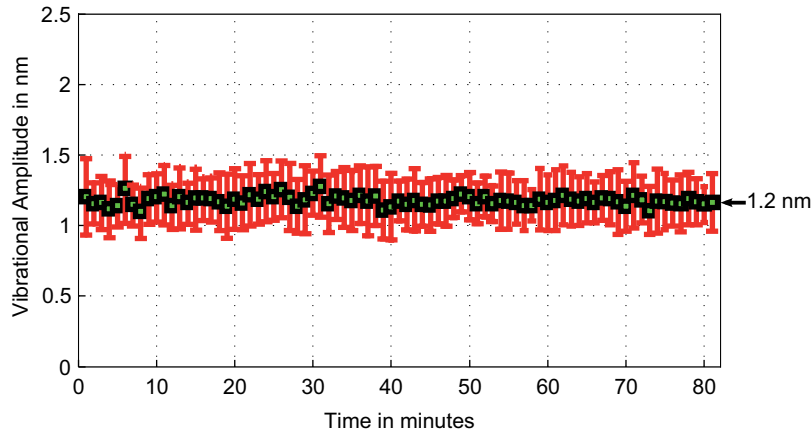
Figure 4.22: Stabilization of the vibration's amplitude of the U-shaped cantilever during a period over 80 minutes in the afternoon. The vibration amplitude of the cantilever without the three-axis compensation system is 298 nm at resonance of S_1.

For the cancellation of unwanted external magnetic fields a cube-shaped frame was built around the measurement setup, with an edge length of about 0.8 m (Fig. 4.23). Three pairs of coils are attached at the frame, where the inductivity of one pair is around 5.5 mH, measured at 1 kHz. Opposite coils of the cube are connected in series and controlled by a custom electronic circuit. Each pair is driven by a power supply, which zeros the field measured by a corresponding commercial fluxgate sensor [135]. The correction signal is generated outside the Helmholtz coil, but near to the measurement probe, which is located in a spatially well-defined vacuum chamber. Each pair of coils is part of a control system, consisting of a PI-feedback circuit and a digital interface. The parameters of each system were specified by empirical trials.

This magnetic field compensation system has been designed to suppress external field disturbances and to permit a characterization of the sensor at small interfering magnetic fields at DC and low frequencies. Because of the large intrinsic mechanical quality factors ($Q \approx 10^4$) of the test structures the response time of the MEMS oscillator increases to several seconds. In this regime, the transducer cannot resolve transient magnetic field disturbances (≈ 10 s) during subway acceleration. Therefore, only steady-state and low-frequency magnetic field disturbances can be compensated or stabilized using the custom magnetic field compensation system. The magnetic field compensation unit from Fig. 4.23 can reduce and stabilize the vibration amplitude from an initial value of 298 nm±4 nm down to 1.2 nm±0.5 nm (Fig. 4.22). Assuming that 298 nm corresponds to approximately 48 μT (and neglecting influences due to vibration noise), the vibration amplitude of 1.2 nm represents 193 nT. The remaining noise at S_1 are primarily
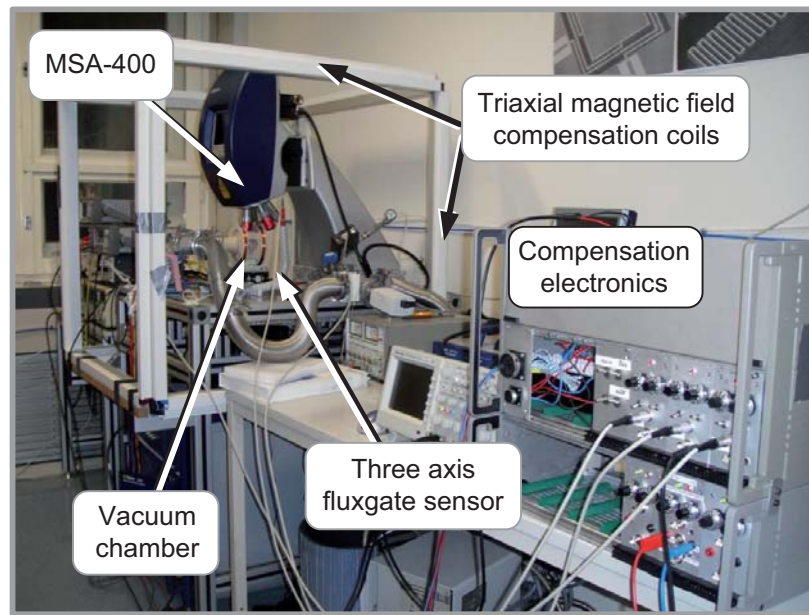
Figure 4.23: Triaxial magnetic field compensation unit surrounding the test structure.

caused by the turbomolecular pump. Experimentally, these disturbances have been minimized by measuring at the higher symmetric resonance S_2.

4.4 Sensing Circuit

This chapter deals with the basic properties of the sensing ciruit, sketched in Fig. 4.24. However, the standard sensing circuit to convert capacitive currents, is a current to voltage converter or transimpedance amplifier. Ideally, the input of the inverting amplifier in Fig. 4.25(a) has negligible impedance, where the input signal is, e.g. a capacitive current. In a first step the kind of circuit was equipped with $R_{in} = 10\,k\Omega$, which is schematically shown in Fig. 4.25(a). Because of the static capacitance in the range of a few pF and mechanical eigenfrequencies in the range of 10 kHz, the impedance of the sensing capacitor is in the range of 10 to 100 MΩ. The inverting amplifier of Fig. 4.25(a) acts practically like a short circuit, as a current to voltage converter will do. Hence, large reaction forces were generated by the circuit that act on the resonator in case of a DC-voltage at the sensing capacitor. It wasn't possible to get rid of nonlinear effects like Duffing behavior, even at mV bias and with R_{in} of 100 kΩ.
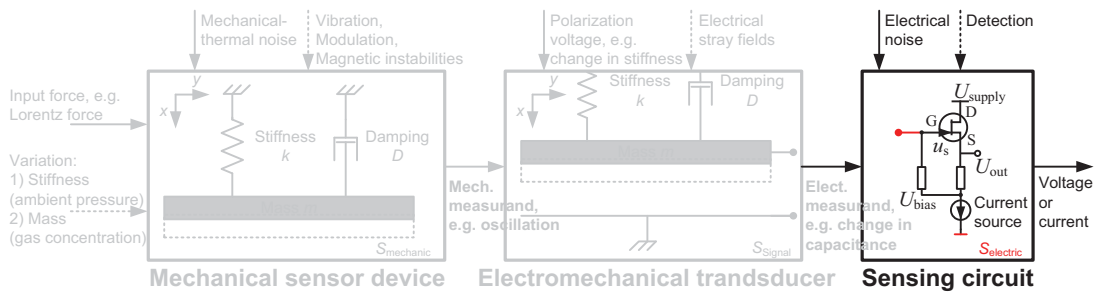
Figure 4.24: Classification of a microelectromechanical system, where the emphasis is laid on the sensing circuit.

Therefore it was clear that other established methods, such as a charge amplifier cannot be considered. If the influence of the reaction forces have to be minimized, the ratio of the voltage U_s at the sense electrode and the average distance d between the cantilever and the sense electrode must be kept constant ($F_e \propto U_s/d = \text{const.}$). From the fundamental relationship $C = Q/U_s$ directly follows that $Q \propto U_s/d = \text{const.}$, which leads to a high-impedance solution. Assuming zero bias current and a finite input resistance of the amplifier, the feedback circuit of Fig. 4.25(b) ensures that the bias voltage of U_{ext} applies directly to the variable capacitor.

Another possibility to sense the cantilever vibrations and to detect the very small capacitance variations at low frequencies in the range of a few fF is by modulating a high frequency carrier signal. This method would be a viable alternative to currently used techniques, but this option was not implemented so far. Especially with an improved design of the resonator and the sensing electrodes, this option seems to have great potential for the future. This kind of circuits has a high resolution and allows the filtering of superimposed low-frequency signals from the electrostatic excitation signal. By using different carrier frequencies, the signal of several electrodes can be detected. The evaluation is then carried out by using a bandpass filter for each electrode, where only signals close to the carrier frequency will pass. At the output of the preamplifier the carrier signal will appear, where the amplitude is modulated by the low-frequency signal. The
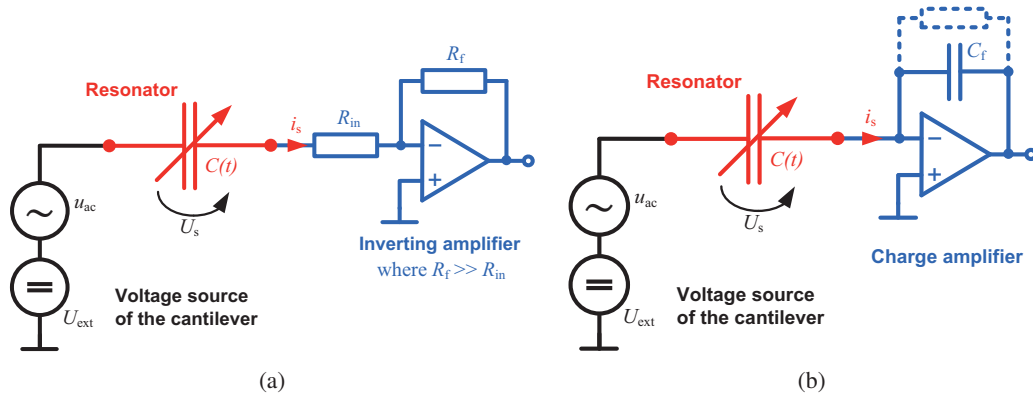
Figure 4.25: (a) Configuration as inverting amplifier that becomes a transimpedance amplifier when $R_{\text{in}} \to 0$. (b) Possible, but not suitable configuration of a charge amplifier because in this case $C_{\text{f}} \gg C(t)$.

amplitude of the modulated signal is proportional to the deflection of the resonator, whereas an additional demodulation unit is required to eliminate the carrier frequency.

This work, as explained in Chapter 3.1, focuses on a sophisticated kind of source follower (see Fig. 3.2). Because of the troubles with reaction forces of circuits with small input impedance, a high-impedance solution was considered. The input impedance should be significantly higher than the impedance of the measuring capacitor (=resonator), which is in the range of $100\,\text{M}\Omega$. Hence, the measurements can be done with negligible nonlinearity due to the operating DC-voltage of the sensing circuit. To explain the functionality of the circuit, the essential components and their operation will be discussed separately. The custom circuit has two special features: firstly, the input impedance is massively increased by bootstrapping. Due to almost identical ac-signals at the two (red) nodes shown in Fig. 4.26(a), the current through the feedback resistor R_{f} is almost zero, and the impedance tends to infinity. But non-negligible input capacities C_{in}, especially between the gate and drain, reduce this magnitude. From the low cutoff frequency of this sensing circuit a value of $5 \cdot 10^{10}\,\Omega$ could be determined.

Secondly, the bandwidth was improved by a sophisticated kind of bootstrap circuit with a positive feedback. Through this trick, the input transistor's drain-gate voltage is kept nearly constant during operation. This technique minimizes the capacitive currents and makes the circuit capable to measure changes in the capacitance up to the high cutoff frequency of $1\,\text{MHz}$, whereas the limit at the lower bound is about $10\,\text{Hz}$. The raise at the lower bound is approximately $+20\,\text{dB/decade}$, whereas the roll-off is around $-40\,\text{dB/decade}$.

With the help of Fig. 4.27, 4.28 and a dummy capacitance of $0.25\,\text{pF}$ it is possible to determine the electrical parameters R_{sub} and C_{sub} of the sensing circuit. Due to the offset of $-13.6\,\text{dB}$ between input and output voltage, an equivalent ratio
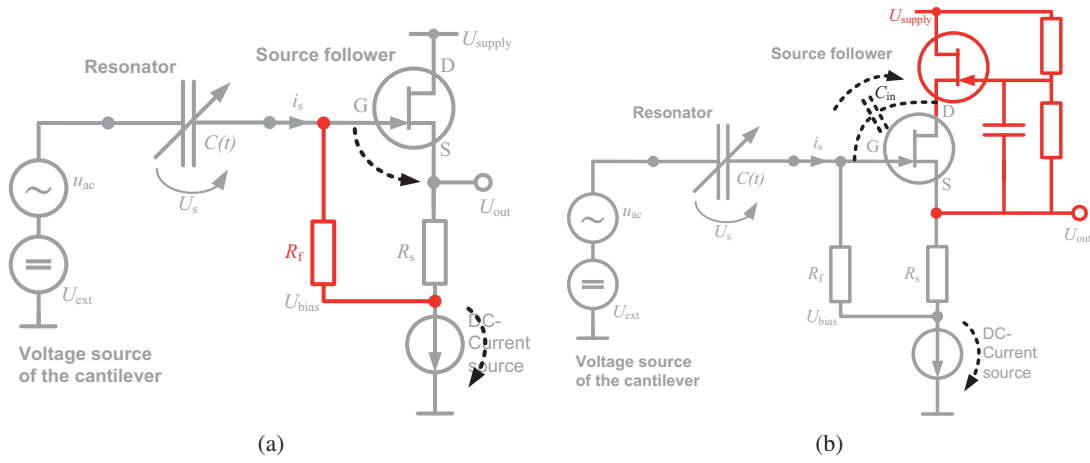
(a)   (b)

Figure 4.26: (a) Bootstrap technique to improve the input impdedance. (b) Shows a similar bootstrap technique configured as positive feedback.
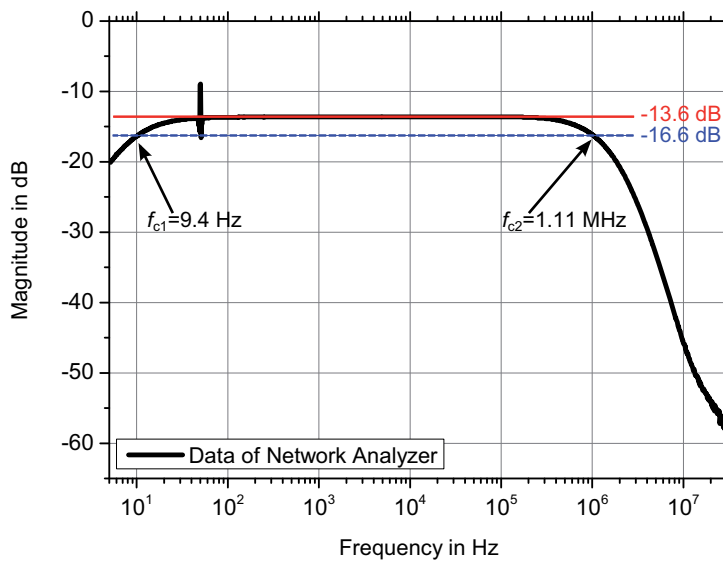

Figure 4.27: Determination of the lower f_{c1} and upper f_{c2} cut-off frequency for the calculation of the input impedance of the sensing circuit.
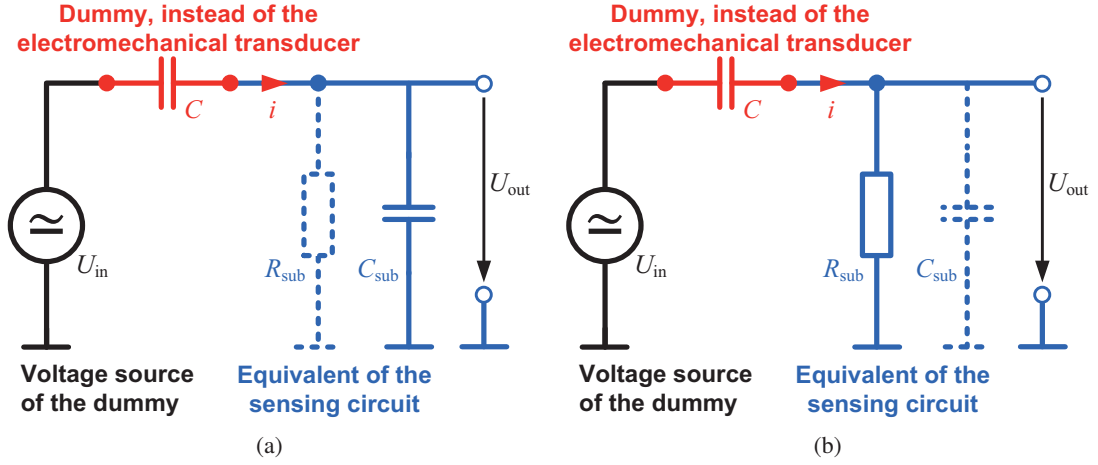
Figure 4.28: (a) Simplified test circuit, for determining the input capacitance C_{sub} ($R_{\mathrm{sub}} \to \infty$). In the case of low frequencies the circuit acts as high pass, where Fig. 4.28(b) shows an equivalent circuit to determine the input impedancede R_{sub}.

$$-13\,\mathrm{dB} = 20\,\log\frac{U_{\mathrm{out}}}{U_{\mathrm{in}}}$$

$$\text{where } \frac{U_{\mathrm{out}}}{U_{\mathrm{in}}} = 0.22 \tag{4.12}$$

could be determined for the voltage ratio. This is very useful in case of the capacitive voltage divider

$$\frac{U_{\mathrm{out}}}{U_{\mathrm{in}}} = \frac{X_{\mathrm{sub}}}{X_{\mathrm{sub}} + X_{\mathrm{C}}} = \frac{1/C_{\mathrm{sub}}}{1/C_{\mathrm{sub}} + 1/250\,\mathrm{fF}} = 0.22 \tag{4.13}$$

that is observed in the flat region of the transfer characteristics, shown in Fig. 4.28(a), where X represents the impedance of the specific electric component. Equation (4.13) implies that the input capacitor of the sensing circuit $C_{\mathrm{sub}} = 0.886\,\mathrm{pF}$, which is in the range of the static capacitance C_0 of the device, as explained in Chapter 3.1. In the case of low frequencies, it is possible to determine R_{sub} with the equivalent circuit of Fig. 4.28(b). The lower cut-off frequency f_{c1} is 9.4 Hz, where

$$2\,\pi\,f_{\mathrm{c1}} = \frac{1}{R_{\mathrm{sub}}C} \tag{4.14}$$

is valid, due to the bandwidth convention $\omega\tau = 1$. The time constant τ of the low pass is determined by the product $R_{\mathrm{sub}}C$. From Eq. (4.14) follows the input resistance with $R_{\mathrm{sub}}{=}67.7\,\mathrm{G\Omega}$, showing that the custom sensing circuit greatly increases the real part of the input impedance. But on the other hand, the imaginary part C_{sub} is only slightly reduced.

4.5 Electrical DC Measurements

The measurement setup depicted in Fig. 4.17, was used to characterize the resonant magnetic field sensor. A sinusoidal current $i = i_0 \cdot \sin(2\pi f_0 t)$ is supplied to the lead on the top of the MEMS structure. A programmable waveform generator produces the current, allowing spectroscopy of the mechanical oscillations. The vibrometer's digital signal processor (DSP) and the Lock-in amplifier are synchronized at the fundamental frequency to measure the vibrometer's output signal. Because of the high intrinsic quality factor in the range of 10^4 at an ambient pressure of 0.2 Pa, the cantilever vibration may take several seconds to settle. In the case of a static magnetic field the frequency f_0 is equal to its mechanical resonance frequency f_r. At low ambient pressure, extrinsic damping mechanisms like gas damping are weak and f_r is very close to the cantilever's fundamental frequency, i.e. in the S1 mode [39]. In the presence of a static magnetic field component B_x perpendicular to the direction of the driving current at the tip of the cantilever, the Lorentz force causes a flexural vibration at its fundamental frequency. If the related deflections are small compared to the length of the cantilever, they are linearly proportional to the drive current and to the applied external magnetic field. As explained in Chapter 3.1, the device requires a dc polarization voltage and a small sinusoidal voltage to excite a sinusoidal resonance electrostatically. The polarization voltage can result in the possibility of a mechanical instability (see Eq. (2.68)) and a lowering of the quality factor (see Eq. (3.7) and Eq. (3.9)). Additionally, parasitics capacities of the electrostatically driven cantilever can also lead to problems in the performance of the electromechanical system. The measurements in Fig. 4.29 of the quality factor at resonant frequency as functions of the polarization voltage U_p were performed with a cantilever featuring a length of 2 mm, a width of 1.5 mm, and a thickness of 20 μm. Each data point in this section was taken at resonance with changing polarization voltage at an ambient pressure around 0.3 Pa and an effective alternating current of 16.9 μA.

From Fig. 4.29 it is obvious that the resonant frequency and the quality factor Q decrease as the applied dc voltage U_{ext} changes around the minimum of the mixing potential (see Eq. (3.13)). According to this figure, the drop of the quality factor Q due to the dc polarization voltage is significant. As a result the minimum of the mixing potential must be found experimentally to operate with low dc polarization voltages U_p in order to obtain a low power dissipation in the beam resonator. Fig. 4.30 is a clear reference of the mixing potentials minimum. The electrical signal at this sensing port shows two minima in its response: one around 3 V and the second around 7 V, whereas the vibrometer signal depicts only one minima at 7 V. This is a result of rather different electrical bias potentials of the independent sensing electronic assemblies connected to the two sensing electrodes (see Fig. 3.5). In this figure, the DC-offset voltage of this port coincides with the value of around 3 V. Therefrom, the DC-offset voltage of the other port must be well above 7 V (around 10 to 11 V). Consequently the oscillations must take a minimum, which is clearly depicted in the vibrometer signal of Fig. 4.30.

A nice hint of the validation of Chapter 3.1 show Fig. 4.31 and 4.32. Due to Eq. (3.9) a linear relationship between the reciprocal value of the quality factor Q

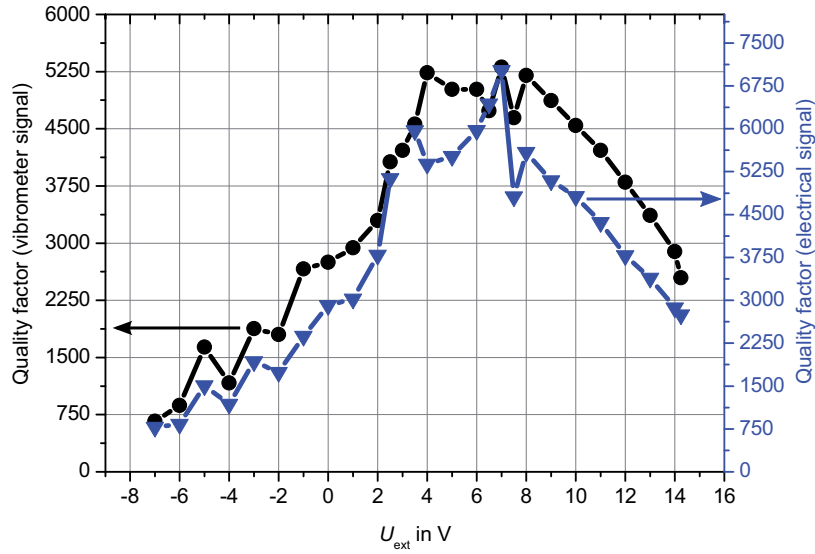$$1/Q = D_e \propto \left(\frac{\varepsilon A}{d^2} U_p\right)^2 \tag{4.15}$$

Figure 4.29: Quality factor of the structure, measured with the vibrometer signal and the electrical signal (always at resonance) in dependence of the polarization voltage.
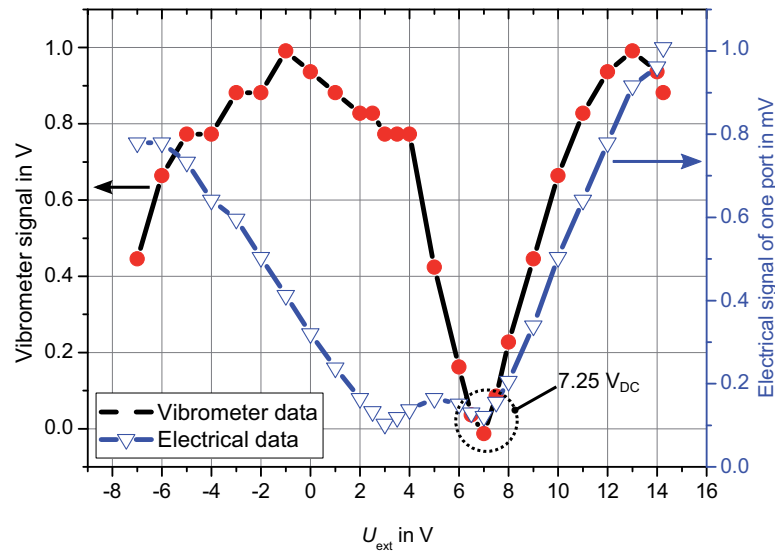

Figure 4.30: The electrical signal comprises two minima: one due to the bias voltage at approximately 3 V. The other minimum is located at approximately 7 V, which coincides with the maximum of the resonance frequency of the system (see Fig. 4.34). This minimum is a result of the mixed potential U_{ext} described in Eq. (3.13). The vibrometer signal only depicts one minimum.

and the squared polarization voltage U_{p} is expected. Fig. 4.31 clearly shows this linear relationship. According to Eq. (2.67), there must be a linear relationship between the squared resonance frequency

$$\omega_r^2 \propto k = k_{\mathrm{m}} - \frac{\varepsilon A}{(d_0 - x_0)^3} U_{\mathrm{p}}^2 , \qquad (4.16)$$

and the squared polarization voltage U_{p} because of $\omega_r^2 = k/m$. Related measurement results are depicted in Fig. 4.32. As expected from the negative electrostatic spring effect of Eq. (2.67), the resonance frequency shift decreases with increasing polarization voltages U_{p}. Fig. 4.33 depicts the limit of the linear behavior of the oscillator in an electrostatic field, due to snap-in behavior shown in Fig. 2.16.
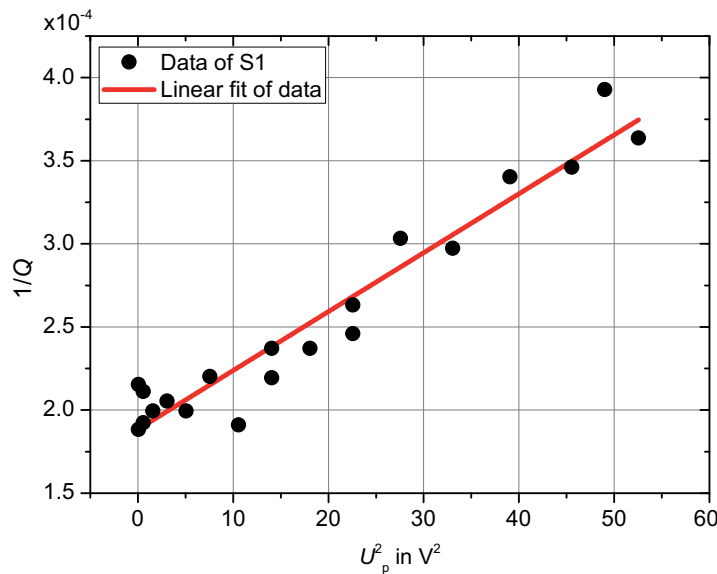
Figure 4.31: The reciprocal value of the quality factor Q of the vibrometer signal in dependence of the squared polarization voltage, where the minimum of the mixing potential is estimated with 7.25 V.

According to Eq. (2.67) and beside the fact of a mixing potential, a quadratic dependence due to the polarization voltage U_{ext} is expected. This relationship is shown in Fig. 4.34. It must be noted that the maximum resonant frequency of the system coinces with the minimum of the mixed potential. Experimentally, this minimum was found by measuring the phase response of the vibrometer signal at the respective resonance. As Fig. 4.35 indicates, there is a rapid change of phase around the mixing potential. Perhaps this is an indication of a change regarding the capacitive behavior of the RLC-serial resonant circuit into an inductive behavior. Up to now, there is no equivalent circuit model regarding the phase-behavior. But on the basis of the comprehensive introduction of the electromechanical modelling in Chapter 3.1 it is possible to predict on the one hand the quadratic behavior of the resonance frequency in dependence
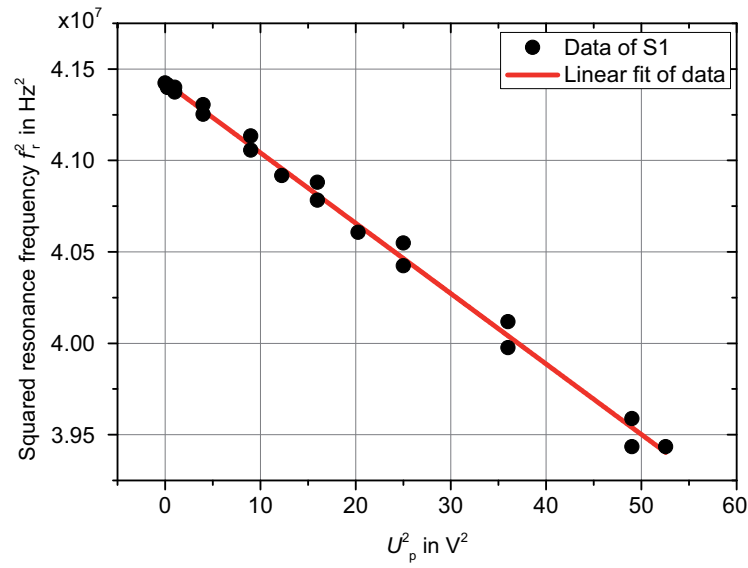
Figure 4.32: The squared resonance frequency of the vibrometer signal in dependence of the squared polarization voltage, where the minimum of the mixing potential is estimated with 7.25 V.
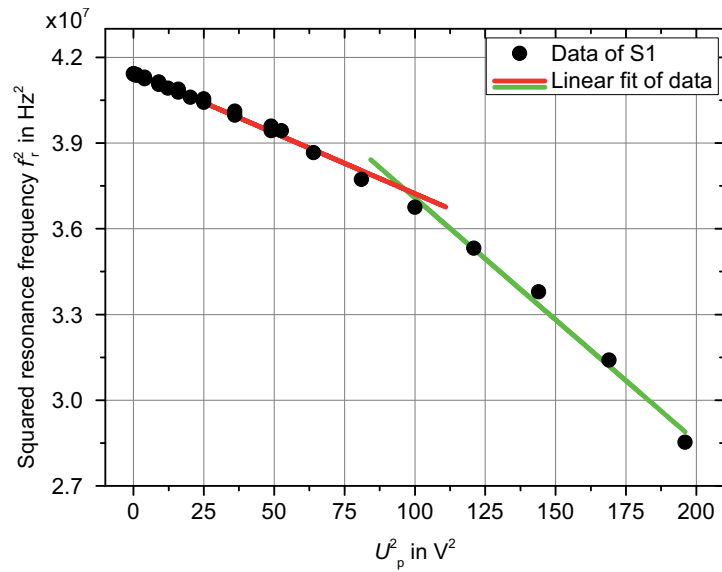

Figure 4.33: The squared resonance frequency of the vibrometer signal in dependence of the squared polarization voltage, where the nonlinearities due to a increasing equilibrium static deflection of the resonator become more important.

of the polarization voltage (see Fig. 4.36) and on the other hand the tendency of the vibration amplitudes in dependence of the resonance frequency (see Fig. 4.37). Fig. 4.36 denotes that the fit perfectly matches the data. Only at the lower bound of the polarization voltage U_{ext} a deviation is peculiar. One reason can be the growth of significant nonlinearity due to increasing static deflections. At the upper bound there is a bias limit, which typically coincides with the supply voltage of the sensing electronics. In order to exclude possible dependencies concerning the polarity of the Helmholtz coil, the measurement regarding the resonance frequency for both polarities was performed (see Fig. 4.38).
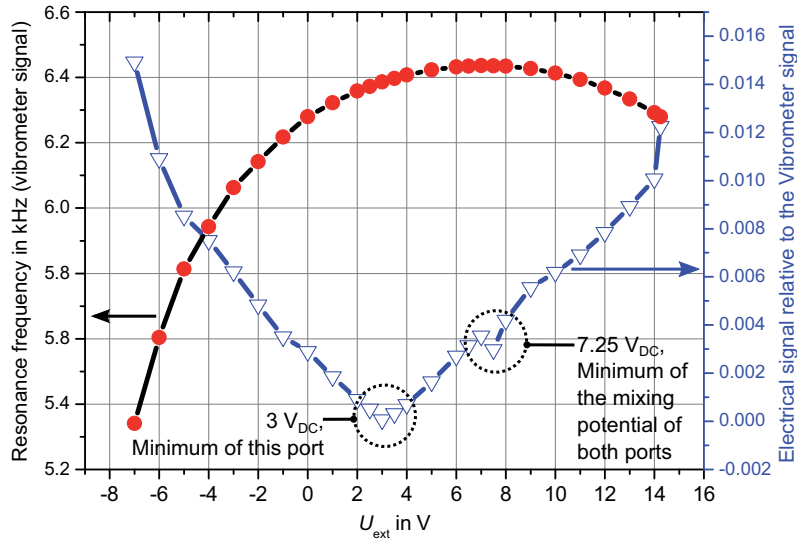
Figure 4.34: Dependence of the resonance frequency on the external polarization voltage U_{ext}. Beside the dependence the signal of the electromechancial system comprise two minima: one minimum due to the DC-offset of port at approximately 3 V. The other minima is located at 7.25 V, which coincides with the maximum of the resonance frequency of the system. This minimum is a result of the combined potential U_{ext} described in Eq. (3.13).

The measurements related to Fig. 4.39 and 4.40 were performed with a U-shaped cantilever featuring a length of 2 mm, a base width of 90 μm, and a thickness of 20 μm, whereat the two 2 mm cantilevers are hold together by a 1.5 mm long bar at the free moving ends. As one can see in Fig. 4.39 and 4.40, there is a linear relationship (100 μT to 6 mT) between the signal output, of both the vibrometer signal and the electrical signal, but below 100 μT a kind of saturation of the signal occurs. Due to Chapter 4.3 the influence of the turbomolecular pump on the vibration masks efficiently the Lorentz force driven oscillations. At the fundamental mode (S1), the measurement limit is approx 300 pm, whereas at the first antisymmetric mode (AS1), this quantity is approximately 100 pm.

Only precision measurements at the second symmetric mode (S2) gave suffient results below typical values of the earth magnetic field (with the help of the compensation unit and during night). Both the vibrometer signal and the electrical signal in Fig. 4.41 and 4.42 indicate linearity down to the sub-μT regime, even for both possibilities in polarity of the Helmholtz coil.
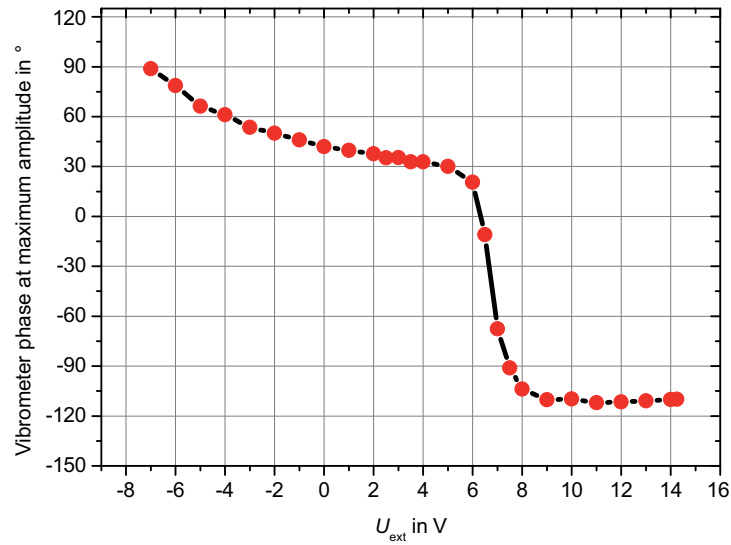
Figure 4.35: Phase response of the vibrometer's signal in dependence of the polarization voltage, where every data point is measured at resonance.

Figure 4.36: The quadratic dependence of the resonance frequency due to the polarization voltage with a data fit according to Eq. (2.68) of. The model of the resonator is based on a cantilever with a length of 2 mm, a width of 1.5 mm and a height of 20 μm. The effective mass m_{eff} is 32 ng, a computed static capacitance C_0 with 0.54 pF and a damping coefficient D of $1.3 \cdot 10^{-6}$.
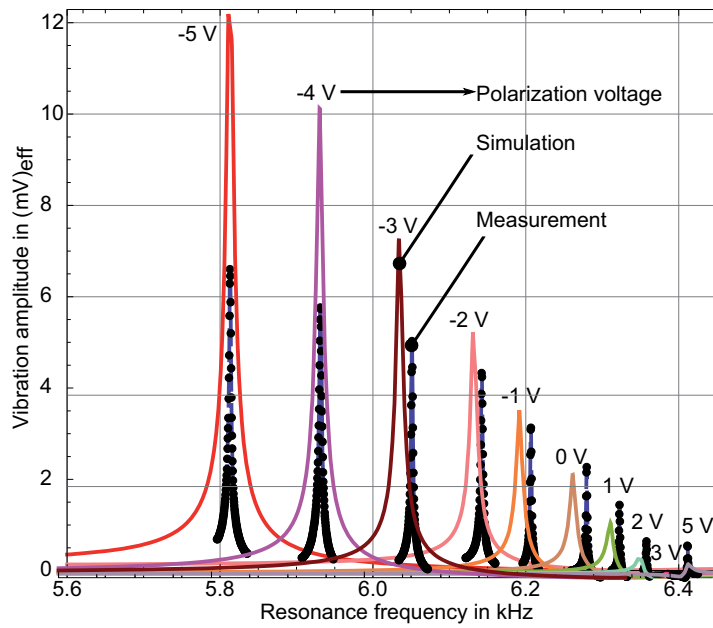
Figure 4.37: Vibration amplitude of the analytical, electromechanical model and the data of a c−f plate with a width of 1.5 mm, a length of 2 mm and a height of 20 µm. The current i_{cant}=16.9 µA and the external magnetic flux is 280 µT.
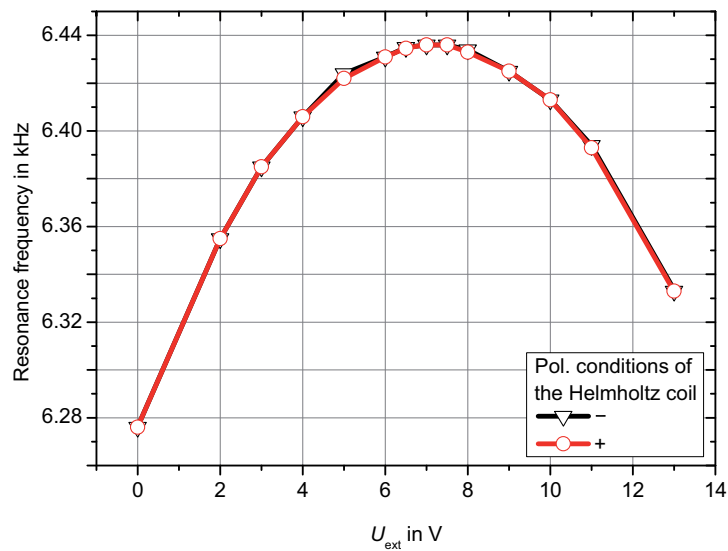
Figure 4.38: Resonance frequency measured by the vibrometer, in dependence of the polarization voltage, on both polarities of the Helmholtz coil configuration.
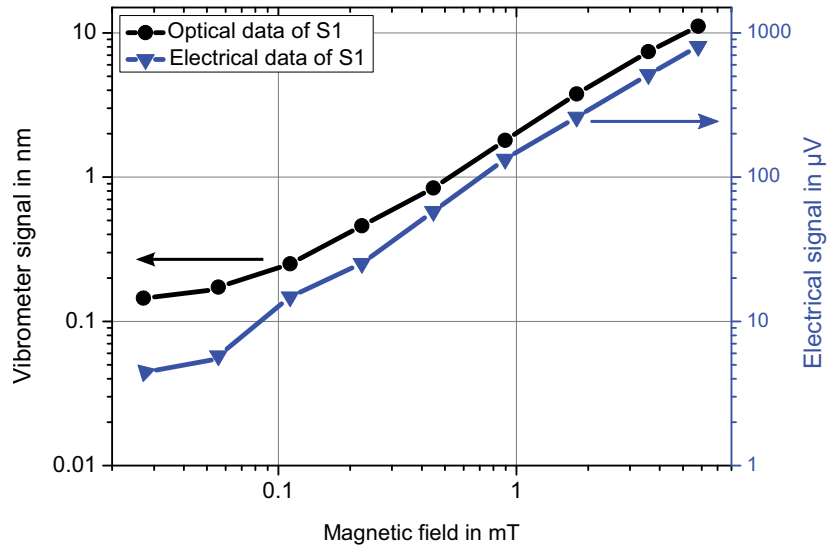
Figure 4.39: Dependence of the vibration amplitude of the first symmetric mode (S1) on the magnetic flux density down to the influence of the vibration of the turbomolecular pump. The resonance is at frequency 4.360 kHz and the driving current is 6.19 μA.
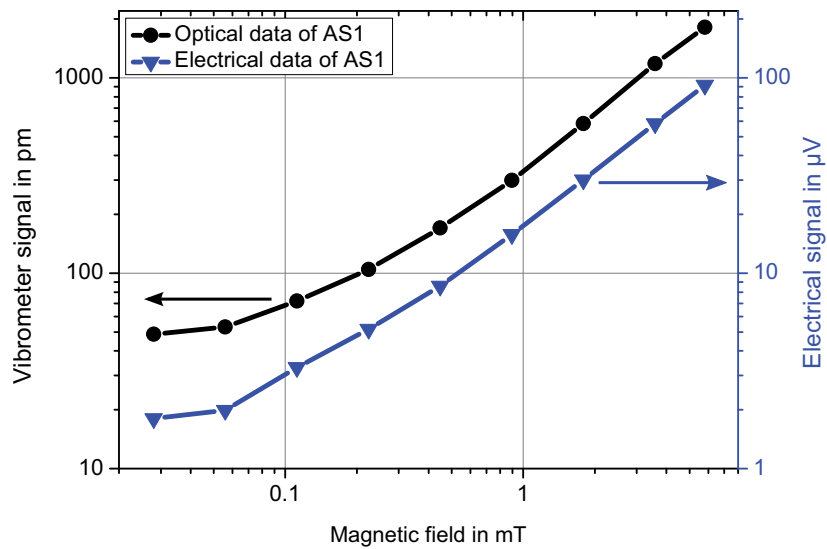

Figure 4.40: Dependence of the vibration's amplitude of the first antisymmetric mode (AS1) on the magnetic flux density with a resonance frequency of 11.313 kHz and the driving current is 561 μA.

Both linear fits show a similar offset of 8.7 µT (optical) and 8.6 µT (electrical), which is a result of the behavior of the electrostatic force (quadratic dependence on the operating voltage) that exceeds the small Lorentz force (linear dependence on the magnetic field). Hence, for sufficiently small fields the electrostatic force dominates at the lower bound. Another limit arises due to the decreasing vibration amplitude in the range of 20 pm at 32 kHz, which declines in the acoustic noise of the turbomolecular pump at S2. The reliable minimum value of the flux density measured with the second symmetric mode was 5 µT.
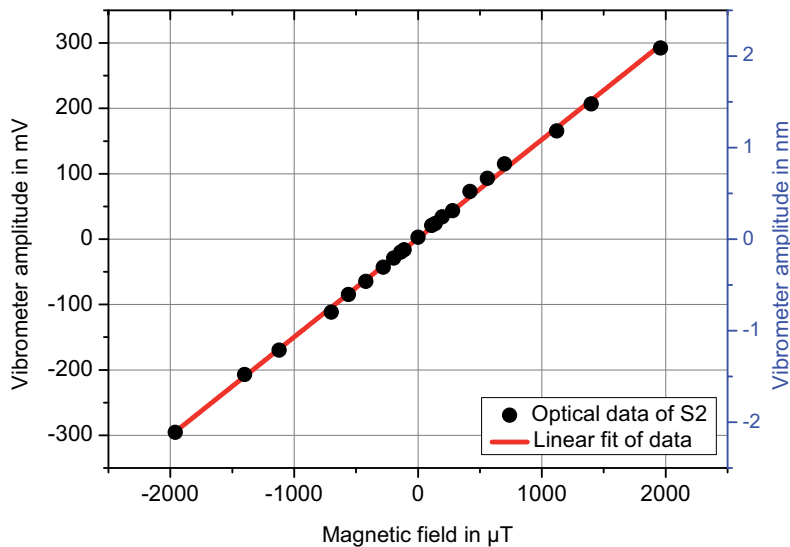

Figure 4.41: Measurement of the dependency of the vibrometer output on the magnetic field distribution to reveal any unsymmetries of the system. The resonance frequency is 32.079 kHz and the driving current is 561 µA.

As long as the behavior between the cantilever deflection and the magnetic field is linear (linear regime), the uncertainty of the measured signal was estimated by averaging the fitted amplitudes of five maxima and five minima data spectra. The resulting standard deviation has a confidence interval of one sigma. Therefrom, the estimated uncertainty in the linear regime at the lower bound of ambient magnetic fields is $\pm 7\%$ of the optical signal and $\pm 6\%$ of the electrical signal. The calibration uncertainties of the measurement instruments, e.g. the uncertainty regarding the measured amplitude of the

- microsystem analyzer is $\pm 3\%$ and

- $\pm 1\%$ for the Lock-in amplifier.

Compared to these nominal values the uncertainties of the applied waveform generator and the multimeter are negligible. Hence, the dominant uncertainty in the linear regime arise from the interfering signals, like the mechanical vibrations of the turbomolecular pump of the vacuum system.
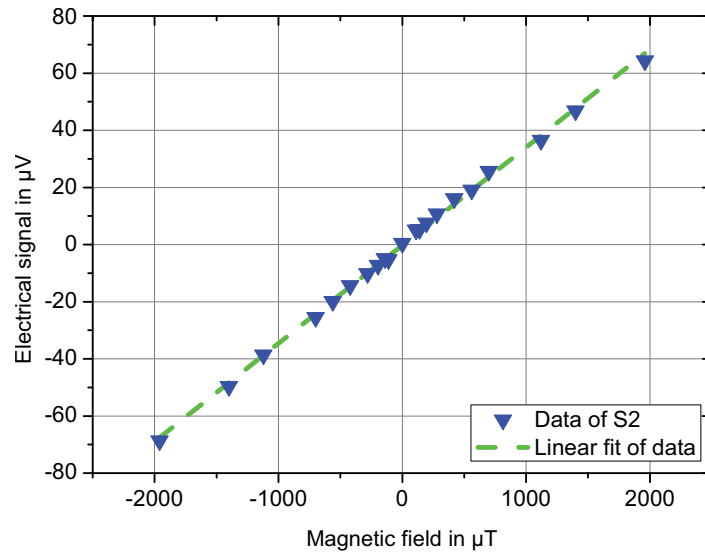
Figure 4.42: Measurement of the dependency of the electrical signal on the magnetic field distribution to reveal any unsymmetries of the system. The resonance frequency is 32.079 kHz and the driving current is 561 µA.
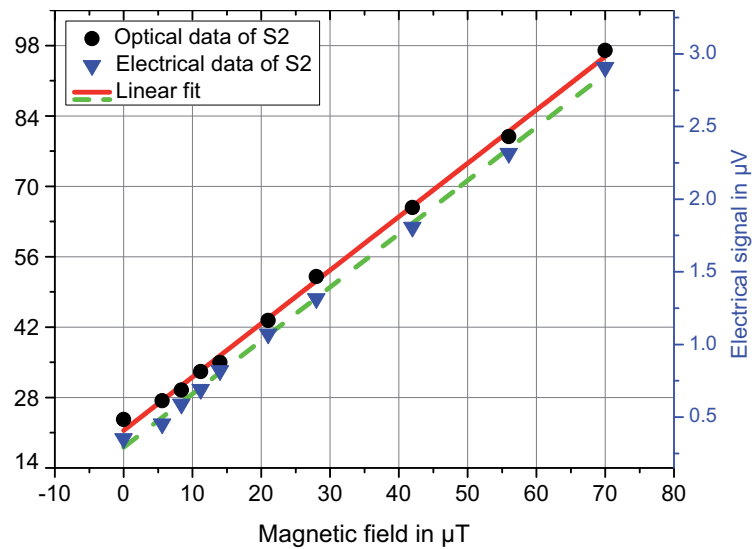

Figure 4.43: Dependence of the vibrometer signal of the second symmetric mode (S2) on the magnetic flux density down to 5 µT.

Due to the much larger deflections at higher magnetic fields, this measurement principle should be applicable up to much larger magnetic flux densities beyond the capability of the Helmholtz coil configuration (limited to approximately 10 mT). One possibility to test the functionality of the sensor at higher flux densities is to use permanent magnets. This permanent magnets must be placed next to the sensor to keep the magnetic flux density constant, since magnetic fields of permanent magnets decrease with $\sim 1/r^3$ and to guarantee a sufficient homogeneity of the magnetic field along the lead at the tip of the cantilever. The strength of the permanent magnet was choosen by the attraction force, which is specified by the distributor[2]. They are based on neodymium iron boron (NdFeB), with a Ni-Cu-Ni-Au coating. The attraction force in descending order is 5.8 N, 8.0 N, 13 N and 17 N. All of them have the same length of 10 mm, but different width's with 4, 5 and 6 mm. According to the normalization of the attraction forces, linearity of the deflections is expected, which is depicted in Fig. 4.45.
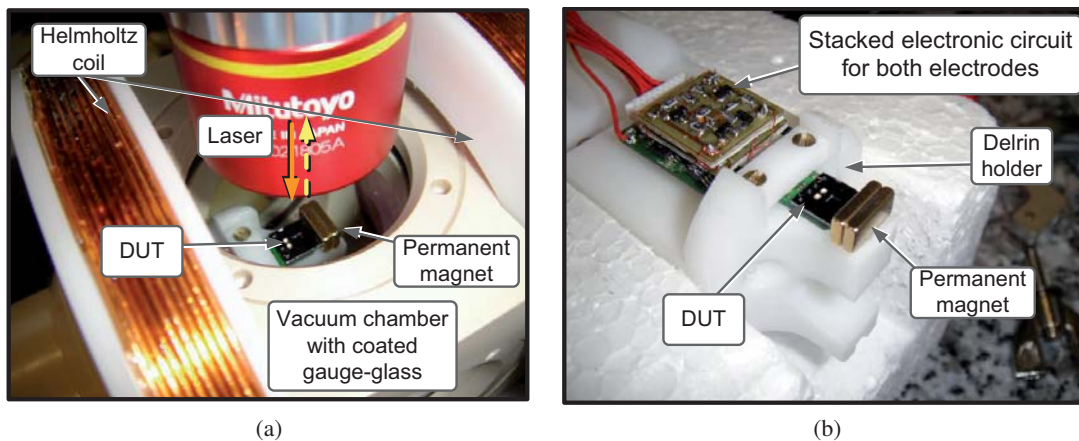

Figure 4.44: Setup for the characterization of the device under test (DUT) for magnetic flux densities in the range of 100 mT to 300 mT.
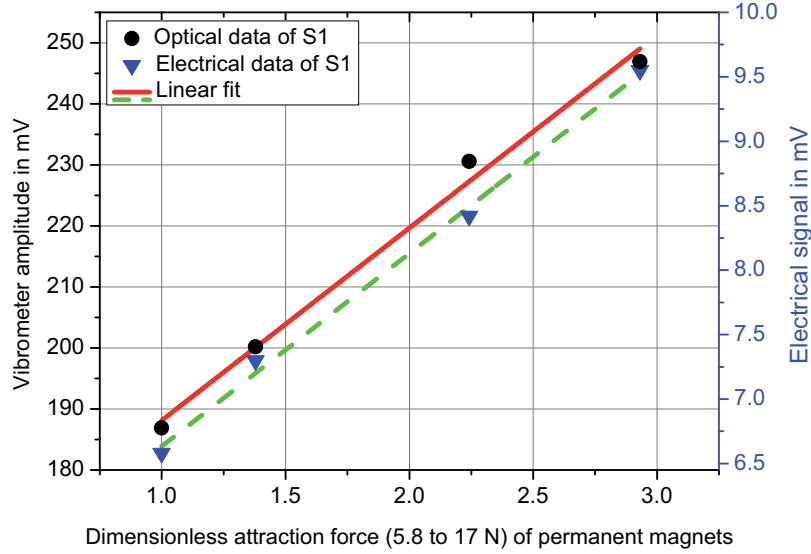
---

[2]www.supermagnete.de (2012)

Figure 4.45: Dependence of the vibration amplitude of the first symmetric mode (S1) on the magnetic flux density in the range of 100 mT to 300 mT. The resonance is at frequency 4.360 kHz and the driving current is 6.19 μA

4.6 Alternating field Measurements

Alternating magnetic fields can be detected in a very similar way to DC-fields. In the case of an additional harmonic magnetic field component, $B_0 + B_1 \cdot \sin(2\pi f_1 t)$, the Lorentz force F_L becomes

$$F_L = [B_0 + B_1\sin(2\pi f_1 t)] \cdot i_0\sin(2\pi f_0 t), \tag{4.17}$$

which can be rewritten as

$$\begin{aligned} F_L = B_0 i_0 \cdot \sin(2\pi f_0 t) \\ + B_1\frac{i_0}{2} \cdot [\cos(2\pi(f_1 - f_0)t) - \cos(2\pi(f_1 + f_0)t)]. \end{aligned} \tag{4.18}$$

The product of two sinusoidal terms produces harmonic Lorentz forces at the sum and difference frequencies [136]. Therefore, the vibrating structure will be, e.g in fundamental resonance if one of the three resulting frequencies f_0 and $f_1 \pm f_0$ is close to the fundamental resonance f_{r1}.

The designed sensor has a measured resonance frequency of 4.359 kHz for the first symmetric and 11.313 kHz for the first antisymmetric mode. Fig. 4.47 emphasizes impressively the linear relationship between the deflections of the structure vibrating at the fundamental mode and the alternating magnetic field B_1 was supplied by the Helmholtz coil.

This linear relationship is valid over several orders of magnitude for an effective current through the lead of the cantilever of 56.3 μA. The fit is nearly zero-centered, if a linear plot of
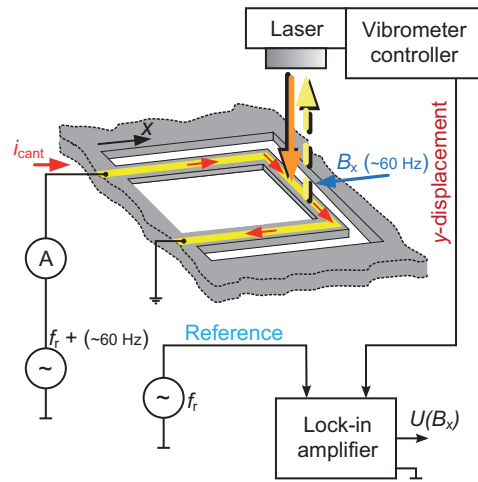
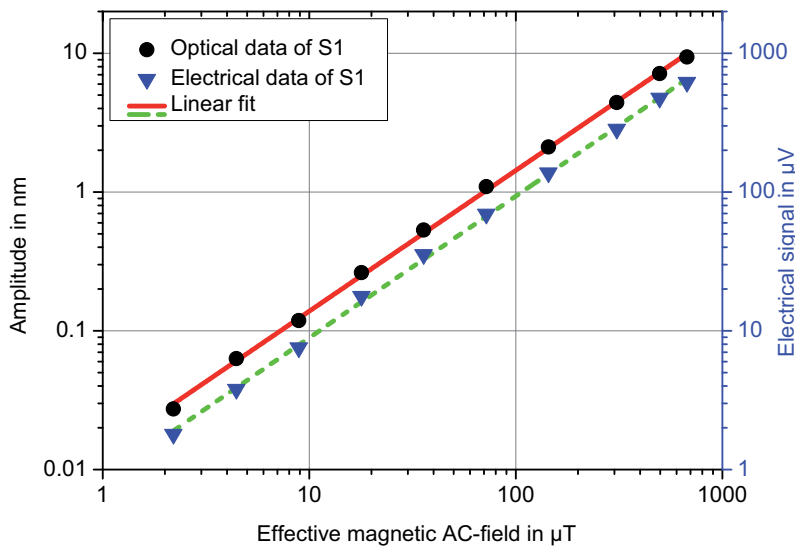Figure 4.46: Schematic setup of the characterization of the test structures.

Figure 4.47: Dependence of the vibration amplitude of the fundamental mode (S1) on the magnetic flux density with a frequency of $60\,\text{Hz}$ and the driving current is $56.29\,\mu\text{A}$.

the results is performed. Suggesting proportionality down to a few nT, despite of the significant acoustical vibrations caused by the turbomolecular pump of the vacuum system. In principle these vibrations limit the detection of the amplitude of the first symmetric vibration mode (see Fig. 4.47).

The minimum detected amplitude of the capacitive readout signal corresponds to a vibration amplitude of 27 pm, the maximum amplitude was 9.4 nm. By contrast, the capacitive signal for the first antisymmetric mode (Fig. 4.48) is less sensitive than for the first symmetric mode. This is a consequence of smaller displacements of the cantilever, where the minimum detected amplitude of 5 pm is significantly smaller than in the case of the fundamental mode. Nevertheless, the sensitivity is once again linear over a wide dynamic range [137, 138].
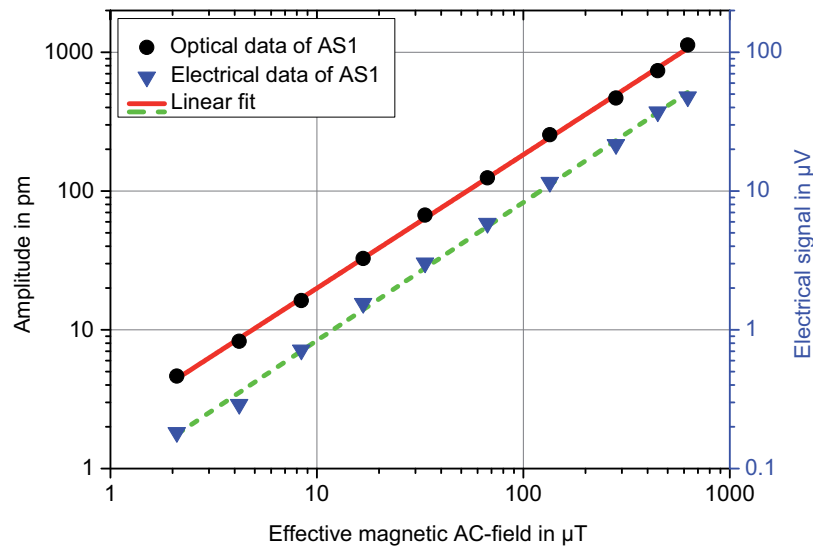

Figure 4.48: Dependence of the vibration amplitude of the first antisymmetric mode (AS1) on the magnetic flux density with a frequency of 60 Hz and the driving current is 56.29 μA.

4.7   Exclusively Optical DC Measurements

Because of the influence of the electrostatic force, which is one of the responsibilities for the limitations regarding the resolution of the sensor, exclusively optical measurements were performed, too. This enables a much simpler construction of device, which is shown in Fig. 4.49.

For the cancellation of unwanted external magnetic fields the custom built compensation unit was used (see Fig. 4.23). To get rid of the frequency band of acoustical noise emitted by the turbo molecular pump of the vacuum system nearby to the fundamental mode (f_{S1}=4.443 kHz), a higher harmonic vibrational mode of the test structure was used. The designed sensor has a measured resonance frequency of 32.705 kHz for the second symmetric mode (S2). From Fig. 4.50 it is obvious that the deflections of the structure vibrating at the second symmetric
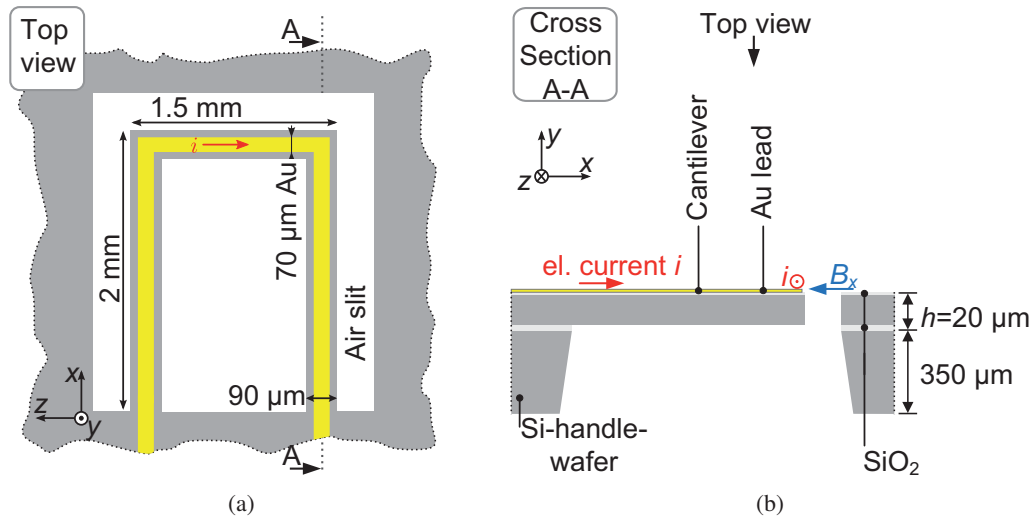
Figure 4.49: 4.49(a) Enlarged schematic top view of the U-shaped cantilever and 4.49(b) schematic cross section of the test device used for optical measurements.

mode show a linear increase with the magnetic field generated by the surrounding Helmholtz coil. This linear relationship is valid over a wide range, but the shown fit is not exactly zero centered. The calculated remaining magnetic field offset is in the range of 266 nT. The reasons of this offset can be the limited resolution of the 12-bit ADC and the offset of the ADC itself that was a part of the control loop used for external field compensation [139].
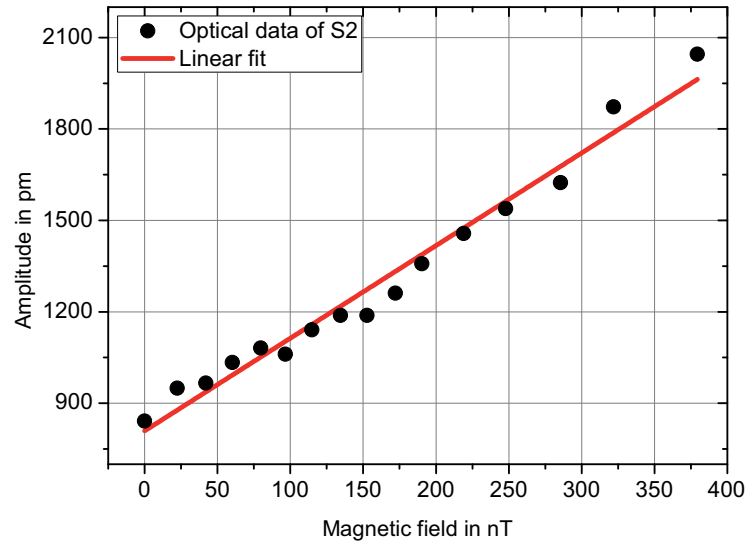
Figure 4.50: Dependence of the vibration's amplitude of the second symmetric mode on the magnetic flux density. The electrical current in the lead on the top of the structure was 22.75 mA and the resonance frequency is 32.705 kHz.

4.8   Pressure Dependence of the Quality Factor in Rarefied Gases

As explained in Chapter 2.3 and 2.3, two damping mechanisms, namely kinetic and squeeze-film damping, dominate in the pressure-dependent transition regime with low Knudsen numbers. In order to obtain data with significant as well as negligible squeeze-film damping several identical structures like the micrograph depicted in Fig. 4.51 are produced. In the case of testing exclusively kinetic damping the PCB underneath the vibrating structure is partially removed (see Fig. 4.52).

Otherwise a fixed wall is placed 350 μm (which conforms to the thickness of the handle wafer) below the test-structure. Usually the lateral air slit is 100 μm, whereat the influence of different slit widths on the quality factor is tested in the transition regime. The used measurement setup is identical with Fig. 4.17, where the micromachined cantilevers featuring a length of 2 mm, a width of 1.5 mm and a thickness of 20 μm. The experimental data shown in Fig. 4.53 are compared with analytical solutions of the Eq. (2.113) and 2.108 on the one hand and with the most recent stochastic model by Okada et al. on the other hand [140].

From Fig. 4.53 it is obvious that the assumptions of the free molecular flow are no longer valid for Knudsen numbers in the range of 0.1 or smaller. The intermolecular collision frequency increases with decreasing Knudsen numbers, where in Fig. 4.53(a) the Knudsen flow evolves into the pressure-independent viscous flow [47]. Compared to that, there is a stronger structure-molecular dependence observable in the results in Fig. 4.53(b) due to the smaller air slit.

This structure-molecular dependence increases with a fixed wall below the vibrating structure. The experimental data shown in Fig. 4.54 are similarly compared with analytical solutions of the Eq. (2.113) and 2.108, but additionally with Eq. (2.111) and 2.114 because of the fixed
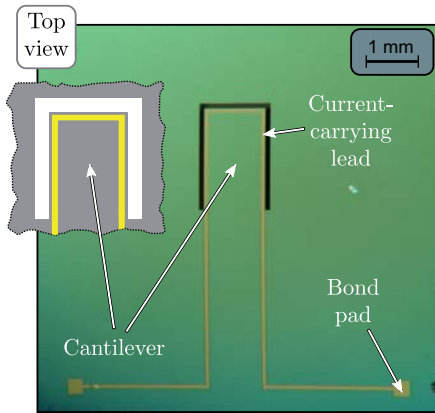
Figure 4.51: Micrograph of the top view of a cantilever with a typical air slit width of 100 µm.
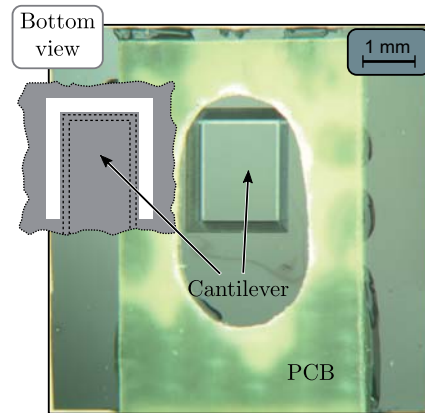
Figure 4.52: Micrograph of a bottom view with removed fixed wall below the test structure.

(a) Air slit width of 100 µm.
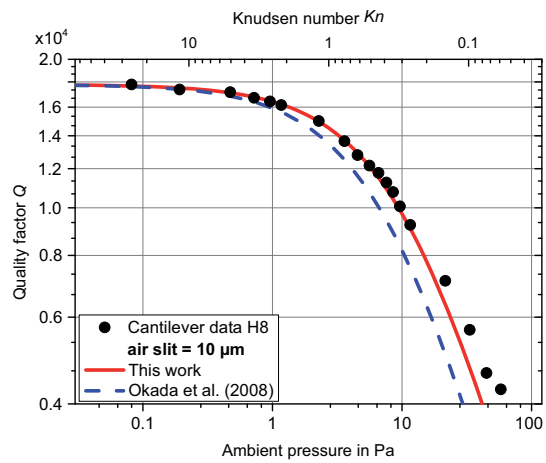
(b) Air slit width of 10 µm.

Figure 4.53: Experimental and theoretical results of the pressure dependence of the quality factor due to intrinsic and kinetic damping mechanisms of a cantilever with a length of 2 mm and a width of 1.5 mm, and with two different widths of the air slit.
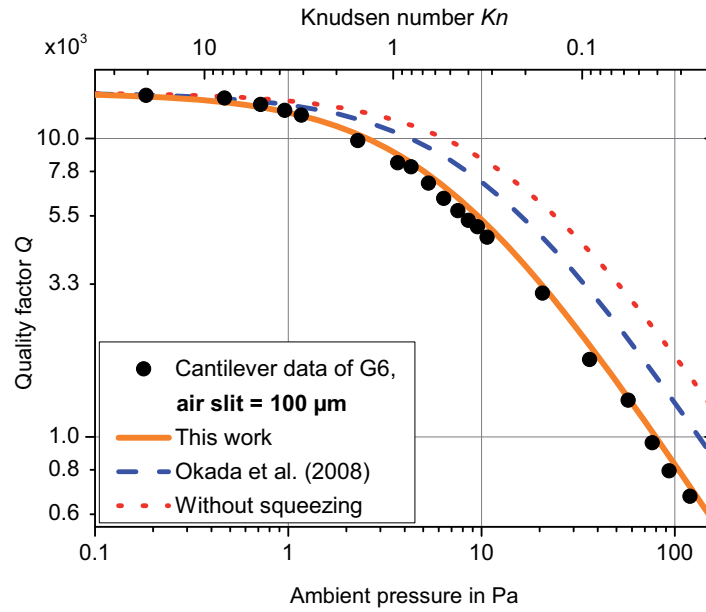
Figure 4.54: Comparison of analytical models with measurement results for a cantilever featuring a length of 2 mm, a width of 1.5 mm, an air slit of 100 μm, and a fixed wall about 350 μm below the cantilever.

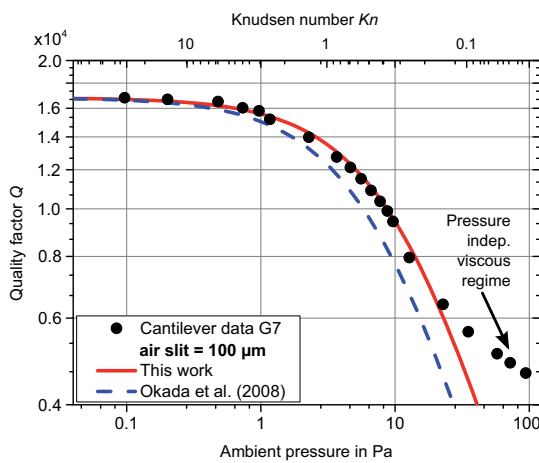wall below the cantilever. In Fig. 4.54 the uncertainty is mainly determined by the lack of knowledge of the equilibrium distance d between the vibrating structure and the fixed wall. It is assumed that this distance corresponds to the thickness of the handle wafer, which is 350 μm with an estimated uncertainty of 10 %. The red dotted curve depticted in Fig. 4.54 represents exclusively kinetic damping. Evidently, squeeze-film damping according to Eq. (2.111) is the second dominant damping mechanism in the transition regime, where the modeled quality factor Q perfectly matches the experimental data [122].

CHAPTER 5

Conclusion

The experimental focus of this thesis was the development of a resonant MEMS magnetic field sensor featuring a capacitive readout. A Lorentz-force actuated cantilever used as a magnetometer detecting both static and alternating magnetic fields has been designed, built, and characterized. Therefore, a microsystem has been created, laying emphasis on both the optimization of the sensitivity of the mechanical resonator and the characterization of the sensor over many orders of magnitude. This sensor is a result of a novel hybrid design, realized with two independent wafer (silicon and Pyrex), which are mounted on top of each other with a custom SU-8 bonding process. All processes steps are on wafer level, except the contacting with the silver conductive paste.

The frequency-selective measurement method of mechanical oscillations provides an alternative to the common broadband measurement techniques. The transducer measures at resonance, where it efficiently filters a certain spectral range of the excitation signal because of the considerable resonant enhancement. A main advantage of this technique is the improvement of the signal-to-noise ratio (SNR) due to the resonance enhancement. If the interfering frequency components do not match the resonance frequency, they are effectively suppressed by the transducer. With a careful design, resonators made of monocrystalline silicon can reach remarkable high quality factors of the order 10^2 to 10^4. Thereby, possible loss mechanisms must be identified, analyzed and interpreted. To observe them apart from each other is one of the challenges of this work, where emphasis was laid on the damping behavior in rarefied gases. A comprehensive study of the damping of monocrystalline silicon cantilevers in different rarefied gas regimes is presented and experimentally verified with the use of a micromotion analyzer. It was demonstrated that two damping mechanisms, namely kinetic and squeeze-film damping, dominate in the pressure-dependent transition regime with low Knudsen numbers in the range of 0.02 to 10. Both damping mechanisms are derived from the assumptions of a free molecular flow, avoiding a priori phenomenological presumptions.

The oscillation signal is measured optical as well as capacitive. The electrostatic force imposed by the sensing electrodes and acting on the effective mass of the oscillating cantilever decreases the resonance frequency, where the stability of such structures is deteriorated by the

occurrence of strong electrostatic softening mechanism. Besides fundamental properties such as the resonance frequency or the band width of the resonance peaks, nonlinearities were analyzed, to develop guidlines for the improvement of the transducer's sensitivity. Ideally, the resonance frequency is independent of the vibration's amplitude, but in a nonlinear systems like the cantilever with an amplitude-dependent electrostatic force, the resonant frequency depends on the operating conditions and the amplitude response can exhibit hysteresis phenomena. Additionally to the excitation of the mechanical structure at its natural resonance, higher modes are also possible, allowing to suppress acoustic interferences. For the development of the whole microelectromechanical system a comprehensive characterization of the structures is necessary. The analog signal acquisition is based on the evaluation of the readout capacitor with a high impedance source follower enabling low system nonlinearity. The operating range regarding the magnetic flux density can be varied over several orders of magnitude.

Moreover, a magnetic field compensation system has been designed to suppress spurious external fields and to permit a characterization of the sensor at small disturbances of the magnetic field at DC and low frequencies. The automatic triaxial compensation system enables a characterization of the newly designed MEMS resonant magnetic field sensor at field comparable with the lower bound of ambient magnetic fields. Finally, the sensor was characterized over a range of seven orders of magnitude both by optical and by capacitive oscillation transduction. Thereby, the sensitivity remains constant with an uncertainty of less than a few percent and keeps its validity for both the fundamental and higher modes.

Table 5.1: Specifications of the Lorentz force actuated resonant MEMS-magnetic field sensor ($f_{r/S2}$=32.077 kHz, driving current: 561 µA, ambient pressure: 0.2 Pa and T_A=25 °C).

Parameter		capacitive	optical
Measurement range	5 µT to $\sim$ 300 mT		
Resolution	300 nT		
Linearity	better than resolution		
Temperature characteristics	-27 ppm/K		
Sensitivity		34 mV/T	1 µm/T

The test results are in good agreement with the thereby obtained theoretical knowledge. Deviations are within the theoretically assessable uncertainties, where the most important reasons are manufacturing tolerances and reasonable model simplifications. This thesis shows that the capacitive read-out limits the achievable sensitivity of the system. The hypothesis was that if the magnitude of external magnetic field densities is too small to detect, an increase of the current on the lead will improve the deflection of the cantilever due to the Lorentz force. However, this measurement strategy leads to an increase of the electric voltage drop, which finally causes nonlinearities of the transducer, depending on the actual arrangement of the capacitive read-out electrodes. These nonlinearities can reach any complexity, which restricts the sensitivity of the sensor significantly. Another limitation arises through the dependence of the sensitivity of the resonator on the mechanical quality factor. To minimize extrinisic damping mechanisms, like gas damping, the device under test is typically placed in a vacuum chamber. Acoustic coupling

to the environment and vibrations of pumping system introduced are the main sources of noise for the device. Further work should aim to improve the sensitivity without operating in rarefied gas regimes and to minimize the complexity of the transducer, with the goal of a full integration of the mechanics and the electronics.

One significant advantage of a single Lorentz force actuated resonant sensor compared to a Hall sensor or a fluxgate sensor is the large dynamic range (see Table 5.1). This is a consequence of the transducer principle, by adaptation of the current according to the external magnetic flux density. However, the complexity of this capacitive detection method due to the electrostatic reaction forces limits the applicability of this sensor in an industrial environment.

APPENDIX A

Acknowledgment

Although a thesis should have only one author, various people have been involved over the years. Against this background, I would like to take the opportunity to acknowledge those people who have helped me realize this work, and more importantly, who have made an indelible impression on my private life and my career during this process.

First and foremost, I would like to express my deep appreciation to my advisor Prof. Franz Keplinger of the Institute of Sensor and Actuator Systems (ISAS). Without his support, exemplary guidance and advice, this thesis would not have been possible. I would also like to thank Dr. Franz Kohl of the Institute for Integrated Sensor Systems (IISS) for his extensive support and help with an almost infinite amount of both technical and scientific details. I also extend my gratitude to Artur Jachimowicz, Johannes Schalko, Peter and Edeltraud Svasek of the ISAS for all they have done during microfabrication process development. In addition, I am grateful to Dr. Thilo Sauter and Roman Beigelbeck of the IISS, for their continual support of my professional goals. Special thanks to Ewald Pirker, who has been in charge of manufacturing of the mechanical parts of my measurement setup. Sincere thanks also go to DDDr. Johannes Steurer of the ISAS and Dr. Karl Edelmoser of the Institute of Energy Systems and Electrical Drives (ESEA), who have been substantially involved in developing the circuitry used in the experiment.

I would also like to thank Prof. Roland Grössinger of the Institute of Solid State Physics (IFP) for kindly agreeing to be the examiner of my PhD-defense. Many thanks to my colleagues at IISS, especially to Wilfried Hortschitz, Harald Steiner and Matthias Sachse, who had to laugh more often than I liked in spite of, maybe because of, my great lack of technical understanding. The time we shared was not only filled with work, but also with fun and friendship. Particular thanks also go to Prof. Ulrich Schmid (ISAS) and Prof. Michiel Vellekoop of the Institute for Microsensors, Actuators and Systems (IMSAS) of the University of Bremen for their support during the work at ISAS. Many thanks also to the administrative staff of IISS and ISAS for their support. The research presented in this thesis was funded by the Austrian Science Fund (FWF): L477-N14. And finally, my gratitude goes to my wife, my children and my extended family. Especially my own family is the rock I stand on.

Bibliography

[1] R. Eisler. Philosophen-Lexikon, Belin 1912, S. 745-746.

[2] http://www.chinaculture.org, January 2011.

[3] Selin Helaine. Model Si Nan of Han Dynasty, February 4 2006.

[4] J.P. Kirsch. Alexander of Neckam (Necham), New York 1911.

[5] H. Rupprich. *Geschichte der deutschen Literatur. Vom späten Mittelalter bis zum Barock.* C.H. Beck, 1994.

[6] S. A. Macintyre. *Magnetic Field Measurement.* CRC Press LLC, 2000.

[7] J. M. Janicke. *The Magnetic Measurements Handbook.* Magnetic Research Press, 1997.

[8] P. Ripka. *Magnetic Sensors and Magnetometers.* Artech House Publishers, 2001.

[9] F. Primdahl. The fluxgate magnetometer. *J. Phys. E: Sci. Instrum.*, 12:241–253, 1979.

[10] B. Ando, S. Baglio, V. Sacco, A. R. Bulsara, and V. In. PCB Fluxgate Magnetometers With a Residence Times Difference Readout Strategy: The Effects of Noise. *IEEE Trans. on Instrumentation. and Measurement*, 57, no. 1:19–24, 2008.

[11] R. Lucklum. *Resonante Sensoren.* PhD thesis, Fakultät für Elektrotechnik und Informationstechnik, Otto-von-Guericke-Universität Magdeburg, 2002.

[12] J.R. Vig, Y. Kim. Noise in microelectromechanical system resonators. *IEEE Trans. Ultrason.,Ferroel. and Frequ. Contr.*, 46:1558–1565, 1999.

[13] M. Bao. *Micro Mechanical Transducers.* Handbook of Sensors and Actuators, 2000.

[14] G. Gerlach, W. Dötzel. *Einführung in die Mikrosystemtechnik.* Hanser Verlag, 2006.

[15] E. Donzier, O. Lefort, S. Spirkovitch and F. Baillieu. Integrated magnetic field sensor. *Sensors and Actuators A*, 26:357–361, 1991.

[16] B. Eyre and K. S. J. Pister. Micromechanical Resonant Magnetic Sensor in Standard CMOS. *International Conference on Solid-state Sensors and Actuators*, pages 405–408, 1997.

[17] Z. Kádár, A. Bossche and J. Mollinger. Integrated resonant magnetic-field sensor. *Sensors and Actuators A*, 41:66–69, 1994.

[18] H. Emmerich, M. Schofthaler. Magnetic field measurements with a novel surface micro-machined magnetic-field sensor. *IEEE Trans. on Electron Dev.*, 47:972–977, 2000.

[19] V. Beroulle, Y. Bertrand, L. Latorre and P. Nouet. Monolithic piezoresistive CMOS magnetic field sensors. *Sensors and Actuators A*, 103:23–32, 2003.

[20] F. Keplinger, S. Kvasnica, A. Jachimowicz, F. Kohl, J. Steurer, H. Hauser. Lorentz force based magnetic field sensor with optical readout. *Sensors and Actuators A*, 110:12–118, 2004.

[21] R. Sunier, T. Vancura, Li Yue, K.-U. Kirstein, H. Baltes, O. Brand. Resonant Magnetic Field Sensor With Frequency Output. *Journal of Microelectromechanical Systems*, 15:1098 – 1107, 2006.

[22] B. Bahreyni, and C. Shafai. A Resonant Micromachined Magnetic Field Sensor. *IEEE Sensors Journal*, 7:1326–1334, 2007.

[23] A.L. Herrera-May, P.J. García-Ramírez, L.A. Aguilera-Cortés, J. Martínez-Castillo, A. Sauceda-Carvajal, L. García-González, and E. Figueras-Costa. A resonant magnetic field microsensor with high quality factor at atmospheric pressure. *J. Micromech. Microeng.*, 19:015016, 2009.

[24] S. Choi, Y.-K. Yoon, S.-H. Kim and M. G. Allen. Nonlinear sensitivity enhancement of resonant microsensors and its application to low power magnetic sensing. *Journal of Micromechanics and Microengineering*, 21:1–12, 2011.

[25] A.L. Herrera-May, P.J. García-Ramírez, L.A. Aguilera-Cortés, E. Figueras, J. Martinez-Castillo, E. Manjarrez, A. Sauceda, L. García-González, R. Juárez-Aguirre. Mechanical design and characterization of a resonant magnetic field microsensor with linear response and high resolution. *Sensors and Actuators A*, 165:399–409, 2011.

[26] Z. Kádár, A. Bossche, P.M. Sarro and J. Mollinger. Magnetic-field measurements using an integrated resonant magnetic-field sensor. *Sensors and Actuators A*, 70:225–232, 1998.

[27] T. C. Leichle, M. v. Arx, and M. G. Allen. A Micromachined Resonant Magnetic Field Sensor. *IEEE*, pages 274–277, 2001.

[28] G. Klaasse, R. Puers and H.A.C. Tilmans. Piezoelectric versus electrostatic actuation for a capacitive RF-MEMS switch. *Proceedings 3rd Workshop on Semiconductor Sensor and Actuator*, pages 631–634, 2002.

[29] N. J. Conway, Z. J. Traina and S.-G. Kim. A strain amplifying piezoelectric MEMS actuator. *Journal of Micromechanics and Microengineering*, 17, no. 4, 2007.

[30] H. Zhang and E. S. Kim. Micromachined acoustic resonant mass sensor. *Journal of M*, 14, no. 4:699–706, 2005.

[31] R. Abdolvand, Z. Hao and F. Ayazi. Temperature-compensated ZnO-on-Diamond resonant mass sensor. *IEEE Sensors Conference*, pages 1297–1300, 2006.

[32] Y.-S. Yang, Y.-H. Lin, Y.-C. Hu and C.-H. Liu. A large-displacement thermal actuator designed for MEMS pitch-tunable grating. *Journal of Micromechanics and Microengineering*, 19, no. 1, 2009.

[33] S. W. Stahl, E. M. Puchner, H. E. Gaub. Photothermal cantilever actuation for fast single-molecule force spectroscopy. *Review of Scientific Instruments*, 80, no. 7, 2009.

[34] F. Keplinger, S. Kvasnica, H. Hauser, R. Grössinger. Optical Readouts of Cantilever Bending Designed for High Magnetic Field Application. *IEEE Transactions on Magnetics*, 39, no. 5:3304–3306, September 2003.

[35] A.L. Herrera-May, L.A. Aguilera-Cortés, L. García-González, E. Figueras-Costa. Mechanical behavior of a novel resonant microstructure for magnetic applications considering the squeezefilm damping. *Microsystem Technologies*, 15:259–268, 2009.

[36] D.-h. Choi, W. D. Nix. Anelastic behavior of copper thin films on silicon substrates: Damping associated with dislocations. *Acta materialia*, 54:679–687, 2006.

[37] N. H. Fletcher, and T. D. Rossing. *The Physics of Musical Instruments*. Springer-Verlag, 1998.

[38] V. Kaajakari. *Practical MEMS: Analysis and design of microsystems, MEMS sensors, electronics, actuators, rf mems, optical mems, and microfluidic systems*. Small Gear Publishing, 2009.

[39] C. M. Harris and Allan G. Piersol, editor. *Harri's Shock and Vibration Handbook*. McGraw-Hill, 2002.

[40] S. Timoshenko. *History of strength of materials*. McGraw-Hill, 1983.

[41] Th. Beck. Leonardo da Vinci (1452 bis 1519). Vierte Abhandlung: Codice atlantico. *Zeitschrift des Vereines deutscher Ingenieure*, 50:524–531, 1906.

[42] C. Zammattio. *The Mechanics of Water and Stone, in L. Reti (ed.), The Unknown Leonardo*. McGraw-Hill, 1974.

[43] H. Parkus. *Mechanik der festen Körper*. Springer Verlag, Vienna, 2nd ed., 1966.

[44] L. D. Landau and E. M. Lifshitz. *Theory of Elasticity*. Pergamon, Oxford, 1986.

[45] W. C. Young, R. G. Budynas. *Roark's Formulas for Stress and Strain*. McGraw-Hill, 7th ed., 2002.

[46] L.D. Landau, E.M. Lifshitz. *Fluid Mechanics*. Pergamon, Oxford, 1987.

[47] F. R. Blom, S. Bouwstra, M. Elwenspoek, J. H. J. Fluitman. Dependence of the quality factor of micromachined silicon beam resonantors on pressure and geometry. *J. Vac. Sci. Technol. B*, 10:19–26, 1992.

[48] R. Lifshitz, M. C. Cross. *Nonlinear Dynamics of Nanosystems*. Wiley-VCH Verlag GmbH, 2010.

[49] J. I. Seeger, S. B. Crary. Stabilization of eletrostatically actuated mechnical devices. In *Int. Conf. on Solid-State Sensors and Actuators (Transducers '97)*, pages 1133–1136, 1997.

[50] A.H. Nayfeh, D.T, Mook. *Nonlinear Oscillations*. John Wiley & Sons, 1979.

[51] G. Schmidt, A. Tondl. *Non-Linear Vibrations*. Cambridge University Press, 2009.

[52] F. Pfeiffer. *Einführung in die Dynamik*. Teubner Studienbücher, 1989.

[53] K. L. Turner, S. A. Miller, P. G. Hartwell, N. C. MacDonald, S. H. Strogatz and S. G. Adams. Five parametric resonances in a microelectromechanical system. *Nature*, 396:149–152, 1998.

[54] M. Zalalutdinov, A. Olkhovets, A. Zehnder, B. Ilic, D. Czaplewski, H. G. Craighead, and J. M. Parpia. Optically pumped parametric amplification for micromechanical oscillators. *Appl. Phys. Lett.*, 78:3142–3144, 2001.

[55] M.-F. Yu, G. J. Wagner, R. S. Ruoff, and M. J. Dyer. Realization of parametric resonances in a nanowire mechanical system with nanomanipulation inside a scanning electron microscope. *Phys. Rev. B*, 66, 2002.

[56] K. Aubin, M. Zalalutdinov, T. Alan, R. B. Reichenbach, R. Rand, A. Zehnder, J. Parpia and H. Craighead. Limit Cycle Oscillations in CW Laser-Driven NEMS. *Journal of Microelectromechanical Systems*, 13:1018–1026, 2004.

[57] A. H. Nayfeh, M. I. Younis. Dynamics of MEMS resonators under superharmonic and subharmonic excitations. *J. Micromech. Microeng.*, 15:1840–1847, 2005.

[58] J. P. Raskin, A. R. Brown, B. T. Khuri-Yakub and G. M. Rebeiz. A Novel Parametric-Effect MEMS Amplifier. *Journal of Microelectromechanical Systems*, 9, NO.4:528–537, 2000.

[59] W. Zhang, R. Baskaran, K. L. Turner. Effect of cubic nonlinearity on auto-parametrically amplified resonant MEMS mass sensor. *Sensors and Actuators A*, 102:139–150, 2002.

[60] B. Ilic, H. G. Craighead, S. Krylov, W. Senaratne, C. Ober, and P. Neuzil. Attogram detection using nanoelectromechanical oscillators. *Journal of Applied Physics*, 95:2694–3703, 2003.

[61] A. Husain, J. Hone, Henk W. Ch. Postma, X. M. H. Huang, T. Drake, M. Barbic, A. Scherer, and M. L. Roukes. Nanowire-based very-high-frequency electromechanical resonator. *Appl. Phys. Lett.*, 83, no. 6:1240–1242, 2003.

[62] A. A. Trusov, A. M. Shkel, editor. *The effect of high order non-linearities on sub-harmonic excitation with parallel plate capacitive actuators*. Proceedings of the ASME 2007 International Design Engineering Technical Conferences & Computers and Information in Engineering Conference, 2007.

[63] R. B. Karabalin, X. L. Feng, and M. L. Roukes. Parametric Nanomechanical Amplification at Very High Frequency. *Nano Letters*, 9, no.9:3113–3123, 2009.

[64] R. M.C. Mestrom, R. H. B. Fey, K. L. Phan, H. Nijmeijer. Simulations and experiments of hardening and softening resonances in a clamped-clamped beam MEMS resonator. *Sensors and Actuators A: Physical*, A162-2:225–234, 2010.

[65] B. E. DeMartini, H. E. Butterfield, J. Moehlis, and K. L. Turner. Chaos for a Micro-electromechanical Oscillator Governed by the Nonlinear Mathieu Equation. *Journal of Microelectromechanical Systems*, 16:1314–1323, 2007.

[66] J. F. Rhoads, S. W. Shaw, K. L. Turner. Nonlinear Dynamics and Its Applications in Micro- and Nanoresonators. *Journal of Dynamic Systems*, 132, 2010.

[67] M. Faraday. On a peculiar class of acoustical figures; and on certain forms assumed by groups of particles upon vibrating elastic surfaces. *Phil. Trans. R. Soc.*, 121:299–340, 1831.

[68] E. Mathieu. Mémoire sur le mouvement vibratoire d'une membrane de forme elliptique. *Journal de mathématiques pures et appliquées 2e série*, 13:137–203, 1868.

[69] F. van der Pol, M. Strutt. On the stability of the solutions of Mathieu' s equation. *Phil. Mag. J. Sci.*, 5:18–38, 1928.

[70] E. I. Butikov. Parametric Resonance in a Linear Oscillator at Square wave modulation. *European Journal of Physics*, 26:157–174, 2005.

[71] J. Guckenheimer, and P. Holmes. *Nonlinear Oscillations, Dynamical Systems, and Bifurcations of Vector Fields*. Springer-Verlag, New York, 1983.

[72] M. I.Younis. *MEMS Linear and Nonlinear Statics and Dynamics*. Springer New York, 2011.

[73] A. Eichler, J. Moser, J. Chaste, M. Zdrojek, I. Wilson-Rae and A. Bachtold. Nonlinear damping in mechanical resonators made from carbon nanotubes and graphene. *Nature Nanotechnology*, 6:339–342, 2011.

[74] J. Wang. Intrinsic Damping: Modeling Techniques for Engineering Systems. *Journal of Structural Engineering*, 135:282–291, 2009.

[75] K. Kreher. *Struktur der Materie*. Teubner Verlagsgesellschaft, 1990.

[76] T.S. Kê. Internal Friction in the Interstitial Solid Solutions of C and O in Tantalum. *Phys. Rev.* , 74, Issue 1:9–15, 1948.

[77] T.S. Kê. Stress Relaxation by Interstitial Atomic Diffusion in Tantalum. *Phys. Rev.* , 74, Issue 1:16–20, 1948.

[78] C. Zener. Internal friction in solids: I. Theory of internal friction in reeds. *Phys. Rev.*, 52:230–235, 1937.

[79] S. W. Yuan and H. N. Bertram. Eddy Current Damping of Thin Film Domain Walls. *IEEE Transactions on Magnetics*, 29, no. 6:2515–2517, 1993.

[80] R. Lifshitz, M. L. Roukes. Thermoelastic damping in micro- and nanomechanical systems. *Phys. Rev. B*, 61:5600–5609, 2000.

[81] S. Prabhakar, S. Vengallatore. Theory of Thermoelastic Damping in Micromechanical Resonators With Two-Dimensional Heat Conduction. *Journal of Microelectromechanical Systems*, 17, no. 2:494–502, 2008.

[82] J. L. Nowinski. *Theory of Thermoelasticity With Applications*. Sijthoff & Noordhoff International Publishers, 1978.

[83] J. E. Bishop and V. K. Kinra. Elastothermodynamic Damping in Laminated Composites. *Int. J. Solids Structures*, 34, no. 9:1075–1092, 1997.

[84] R. Sandberg, K. Molhave, A. Boisen, and W. Svendsen. Effect of gold coating on the Q-factor of a resonant cantilever. *Journal of Micromechanics and Microengineering*, 15:2249–2253, 2005.

[85] R. N. Candler, A. Duwel, M. Varghese, S. A. Chandorkar, M. A. Hopcroft, W.-T. Park, B. Kim, G. Yama, A. Partridge. M. Lutz and T. W. Kenny. Impact of Geometry on Thermoelastic Dissipation in Micromechanical Resonant Beams. *Journal of M*, 15, no. 4:927–934, 2006.

[86] Z. Hao, A. Erbil, F. Ayazi. An analytical model for support loss in micromachined beam resonators with in-plane flexural vibrations. *Sensors and Actuators A*, 109:156–164, 2003.

[87] J. Yang, T. Ono, M. Esashi. Energy Dissipation in Submicrometer Thick Single-Crystal Silicon Cantilevers. *Journal of Microelectromechanical Systems*, 11, no.6:775–783, 2002.

[88] D. S. Bindel, E. Quevy, T. Koyama, S. Govindjee, J. W. Demmel, R.T. Howe. Anchor loss simulation in resonators. *Technical Digest of the IEEE International Conference on Micro Electro Mechanical Systems*, (e):133–136, 2005.

[89] D. M. Photiadis and J. A. Judge. Attachment losses of high Q oscillators. *Applied Physics Letters*, 85, no. 3:482–484, 2004.

[90] M.C. Cross, R. Lifshitz. Elastic wave transmission at an abrupt junction in a thin plate with application to heat transport and vibrations in mesoscopic systems. *Phys. Rev. B*, 64:1–22, 2001.

[91] J. A. Judge, D. M. Photiadis, Joseph F. Vignola, Brian H. Houston and Jacek Jarzynski. Attachment loss of micromechanical and nanomechanical resonators in the limits of thick and thin support structures. *Journal of Applied Physics*, 101:1–11, 2007.

[92] R. Tabrizian, M. Rais-Zadeh, and F. Ayazi. Effect of Phonon Interactions on Limiting the f.Q Product of Micromechanical Resonators. *IEEE Transducers*, pages 2132–2134, 2009.

[93] H. A. Sodano and J.-S. Bae. Eddy Current Damping in Structures. *The Shock and Vibration Digest*, 36, no. 6:469–478, 2004.

[94] X. M. H. Huang, X. L. Feng, C. A. Zorman, M. Mehregany and M. L. Roukes. VHF, UHF and microwave frequency nanomechanical resonators. *New Journal of Physics*, 7, 247:1–15, 2005.

[95] E. E. Kriezis, Th. D. Tsiboukis, S. M. Panas, and J. A. Tegopoulos. Eddy Currents: Theory and Applications. *Proc. of the IEEE*, 80, no. 10:1559–1589, 1992.

[96] G. G. Stokes. On the Effect of the Internal Friction of Fluids on the Motion of Pendulums. *Transactions of the Cambridge Philosophical Society*, IX, 1850.

[97] H. Hosaka, K. Itao, S. Kuroda. Damping characteristics of beam-shaped micro-oscillators. *Sens. Actuators*, A49:87–95, 1995.

[98] J. E. Sader, T. P. BURG and S. R. Manalis. Energy dissipation in microfluidic beam resonators. *J. Fluid Mech.*, pages 1–36, 2010.

[99] T. Veijola. Compact models for squeezed-film dampers with inertial and rarefied gas effects. *Journal of Micromechanics and Microengineering*, 14:1109–1118, 2004.

[100] T.I. Gombosi. *Gaskinetic theory*. Cambridge Univ. Press, 1994.

[101] G. A. Bird. *Molecular Gas Dynamics and the Simulation of Gas Flows*. Oxford, U.K., 1994.

[102] M. Gad-el-Hak. The Fluid Mechanics of Microdevices—The Freeman Scholar Lecture. *Journal of Fluids Engineering*, 121:5–33, 1999.

[103] T. Veijola, H. Kuisma, J. Lahdenperä, T. Ryhänen. Equivalent-circuit model of the sqeezed gas film in a silicon accelerometer. *Sensors and Actuators A*, 48:239–248, 1995.

[104] R. C. W. Leung, T. Thurber, and W. Ye. On the modified Reynolds equation model for the prediction of squeeze-film gas damping in a low vacuum. *Microfluid Nanofluid*, 11:753–762, 2011.

[105] A. A. Alexeenko, S. F. Gimelshein, E. P. Muntz, A. D. Ketsdever. Kinetic modeling of temperature driven flows in short microchannels. *Kinetic modeling of temperature driven flows in short microchannels*, 45, Issue 11:1045–1051, 2006.

[106] M. Suijlen, J.J. Koning, M.A.J. van Gils, H.C.W. Beijerinck. Squeeze film damping in the free molecular flow regime with full thermal accommodation. *Sensors and Actuators A: Phys*, page doi:10.1016/j.sna.2009.03.025, 2009.

[107] H. W. Drawin. Theoretische Ableitung der Eichkurven für kontinuierlich anzeigende Reibungs- und Wirbelvakuummeter. *Vakuum-Technik*, 11:45–49, 1962.

[108] R. G. Christian. The theory of oscillating-vane vacuum gauges. *Vacuum*, 16:175–178, 1966.

[109] M. J. Martin, B. H. Houston, J. W. Baldwin, M. K. Zalalutdinov. Damping Models for Microcantilevers, Bridges, and Torsional Resonators in the Free-Molecular-Flow Regime. *Journal of Microelectromechanical Systems*, 17:503–511, 2008.

[110] M. Bao, H. Yang. Squeeze film air damping in MEMS. *Sensors and Actuators A*, 136:3–27, 2007.

[111] C. Gui, R. Legtenberg, M. Elwenspoek, J.H. Fluitman. Q-factor dependence of one-port encapsulated polysilicon resonator on reactive sealing pressure. *J. Micromech. Microeng.*, 5:183–185, 1995.

[112] B. Xiong G. Wu, D. Xu and Y. Wang. A high-performance bulk mode single crystal silicon microresonator based on a cavity-SOI wafer. *Journal of Microme*, 22:1–8, 2012.

[113] S. Prabhakar, S. Vengallatore. Thermoelastic damping in bilayered micromechanical beam resonators. *Journal of Micromechanics and Microengineering*, 17:532–538, 2007.

[114] J. Lübbe, L. Tröger, S. Torbrügge, R. Bechstein, C. Richter, A. Kühnle and M. Reichling. Achieving high effective Q-factors in ultra-high vacuum dynamic force microscopy. *Measurement Science and Technology*, 21:1–9, 2010.

[115] L. Khine and M. Palaniapan. High-Q bulk-mode SOI square resonators with straight-beam anchors. *Journal of Microm*, 19, no.1, 2009.

[116] J. E.-Y. Lee and A. A. Seshia. 5.4-MHz single crystal silicon wine glass mode disk. *Sensors and Actuators A*, 156, no.1:28–35, 2009.

[117] G. Wu, D. Xu, B. Xiong and Y. Wang. A high-performance bulk mode single crystal silicon microresonator based on a cavity-SOI wafer. *Journal of Micromechanics and Microengineering*, 22:1–8, 2012.

[118] T. H. Metcalf, X. Liu. An Ultra-High Q Silicon Cantilever Resonator for Thin Film Internal Friction and Young's Modulus Measurements. *Solid State Phenomena*, 184:325–330, 2012.

[119] Y. Ahn, H. Guckel and J. D. Zook. Capacitive microbeam resonator design. *Journal of Micromechanics and Microengineering*, 11:70–80, 2000.

[120] IEEE Standard on Piezoelectricity, Std 176-1987, 1987, p. 51.

[121] E. Benes. Improved quartz crystal microbalance technique. *Journal of Applied Physics*, 56:608–626, 1984.

[122] M. Stifter, M. Sachse, T. Sauter, W. Hortschitz and F. Keplinger. Pressure dependence of the quality factor of a micromachined cantilever in rarefied gases. *Journal of Physics: Conference Series*, 362, no. 1:1–9, 2012.

[123] F. Mohd-Yasin, D. J. Nagel and C. E. Korman. Noise in MEMS. *Measurement Science and Technology*, 21:1–22, 2010.

[124] J. J. Talghader. Thermal and mechanical phenomena in micromechanical optics. *Journal of Physics D: Applied Physics*, 37:109–122, 2004.

[125] F. L. Walls, and J. R. Vig. Fundamental Limits on the Frequency Stabilities of Crystal Oscillators. *IEEE T*, 42, no. 4:576–589, 1995.

[126] J. R. Vig, C. Audoin, L. S. Cutler, M. M. Driscoll, E. P. EerNisse, R. L. Filler, R. M. Garvey, W. J. Riley, R. C. Smythe, R. D. Weglein. The Effects of Acceleration on Precision Frequency Sources. *Research and Development Technical Report SLCET-TR-91-3 (Rev. 1)*, pages 1–64, 1992.

[127] D. DiLella, L.J. Whitman, R. J. Colton, T. W. Kenny, W. J. Kaiser, E.C. Vote, J. A. Podosek, L. M. Miller. A micromachined magnetic-field sensor based on an electron tunneling displacement transducer. *S*, 86:8–20, 2000.

[128] A. N. Cleland and M. L. Roukes. Noise processes in nanomechanical resonators. *Journal of*, 92, no. 5:2758–2769, 2002.

[129] T. B. Gabrielson. Mechanical-Thermal Noise in Micromachined Acoustic and Vibration sensors. *IEEE Trans. on Electron Devices*, 40, no. 5:903–909, 1993.

[130] L. S. Cutler, and C. L. Searle. Some Aspects of the Theory and Measurement of Frequency Fluctuations in Frequency Standards. *Proc. of the IEEE*, 54, no. 2:136–154, 1966.

[131] Y. K. Yong, J. R. Vig. Resonator Surface Contamination-A Cause of Frequency Fluctuations? *IEEE T*, 36, no. 4:452–458, 1989.

[132] J. R. Vig, and Y. Kim. Noise in Microelectromechanical System Resonators. *IEEE T*, 46, no. 6:1558–1565, 1999.

[133] M. A. Hopcroft, Member, W. D. Nix, and T. W. Kenny. What is the Young's Modulus of Silicon? *Journal of Microelectromechanical Systems*, 19, no. 2:229–238, 2010.

[134] E. Iervolino, M. Riccio, F. Santagata, J. Wei, A.W. van Herwaarden, A. Irace, G. Breglio, P.M. Sarro. Resonance frequency of locally heated cantilever beams. *Sensors and Actuators A: Physical*, page to appear, 2012.

[135] http://www.speakesensors.co.uk, June 2012.

[136] R. B. Givens, D. K. Wickenden, D. A. Oursler, R. Osiander, J. L. Champion, and T. J. Kistenmacher. Heterodyne detection of alternating magnetic fields with a resonating xylophone bar magnetometer. *Applied Physics Letters*, 74, no. 10:1472–1474, 1999.

[137] M. Stifter, T. Sauter, W. Hortschitz, F. Keplinger and H. Steiner. MEMS Heterodyne AMF Detection with Capacitive Sensing. *Proceedings of the IEEE Sensors*, page to appear, 2012.

[138] MEMS Magnetic AC Field Detection. MEMS Magnetic AC Field Detection. *4M2012 Conference Proceedings*, 2012.

[139] M. Stifter, H. Steiner, F. Keplinger, W. Hortschitz, T. Sauter. Magnetic Field Stabilization for MEMS Applications by an Automatic Triaxial Compensation Unit. *Vienna Magnetics Group Reports*, pages 37–38, 2012.

[140] H. Okada, T. Itoha, T. Suga. Wafer level sealing characterization method using Si micro cantilevers. *Sensors and Actuators A: Physical*, 147:359–364, 2008.

Curriculum Vitae

Persönliche Daten

MMag. Michael Stifter

Hammerbachgasse 16, 2620 Neunkirchen

Geboren am 11.12.1975 in Oberpullendorf

Verheiratet mit Heidemarie Stifter

Kinder: Franziska Karoline und Raphael Johannes

Ausbildung und Berufspraxis

1982 – 1986	Volksschule, Lutzmannsburg
1986 – 1994	Realgymnasium, Oberpullendorf
1994 – 2001	Lehramt Mathematik und Physik, Universität Wien
1995 – 2000	Diplom Physik, Universität Wien
2000 – 2001	Militärdienst, ABC-Abwehrschule Wien
2001 –	Mittelschullehrer, Höhere Technische Bundes- Lehr- und Versuchsanstalt Wiener Neustadt
2007 –	Wissenschaftler, Institut für Integrierte Sensorsysteme (ÖAW), Wiener Neustadt
2008 – 2012	Doktoratsstudium der technischen Wissenschaften, TU Wien

Weitere Aktivitäten

2007 – 2012	Teilnahme an Robotikbewerben als Betreuer, wie z.B. den Roboterweltmeisterschaften in Singapur 2010 oder Hawaii 2012

Neunkirchen, 25. Oktober 2012